

Fundamental Studies of Subsonic and Transonic Flow Separation

Part III. Third Phase Summary Report

J. M. Wu, et al.

Gas Dynamics Division
The University of Tennessee Space Institute
Tullahoma, Tennessee 37388

October 1979

Final Report — November 1975 — September 1978

**TECHNICAL REPORTS
FILE COPY**

Approved for public release; distribution unlimited.

Property of U. S. Air Force
AEDC LIBRARY
F40600-77-C-0003

**ARNOLD ENGINEERING DEVELOPMENT CENTER
ARNOLD AIR FORCE STATION, TENNESSEE
AIR FORCE SYSTEMS COMMAND
UNITED STATES AIR FORCE**

NOTICES

When U. S. Government drawings, specifications, or other data are used for any purpose other than a definitely related Government procurement operation, the Government thereby incurs no responsibility nor any obligation whatsoever, and the fact that the Government may have formulated, furnished, or in any way supplied the said drawings, specifications, or other data, is not to be regarded by implication or otherwise, or in any manner licensing the holder or any other person or corporation, or conveying any rights or permission to manufacture, use, or sell any patented invention that may in any way be related thereto.

Qualified users may obtain copies of this report from the Defense Documentation Center.

References to named commercial products in this report are not to be considered in any sense as an indorsement of the product by the United States Air Force or the Government.

This final report was submitted by The University of Tennessee Space Institute, Tullahoma, Tennessee 37388 under contract F40600-76-C-0006, with the Arnold Engineering Development Center/DOT, Arnold Air Force Station, Tennessee 37389. Captain Steve Lamkin, Directorate of Technology was the AEDC Project Manager.

This report has been reviewed by the Information Office (OI) and is releasable to the National Technical Information Service (NTIS). At NTIS, it will be available to the general public, including foreign nations.

APPROVAL STATEMENT

This report has been reviewed and approved.



ELTON R. THOMPSON
Project Manager
Directorate of Technology

Approved for publication:

FOR THE COMMANDER



MARION L. LASTER
Director of Technology
Deputy for Operations

UNCLASSIFIED

| REPORT DOCUMENTATION PAGE | | READ INSTRUCTIONS BEFORE COMPLETING FORM | | | | | | | | | | | | | | | |
|---|--------------------------|---|-----------------|--------------------------|-------------------------|----------------|----------------------|-----------|---------------|------------------|-----------------------------|----------------------|-----------|--|----------------|-----------|--|
| 1. REPORT NUMBER AEDC-TR-79-48 | 2. GOVT ACCESSION NO. | 3. RECIPIENT'S CATALOG NUMBER 5 | | | | | | | | | | | | | | | |
| 4. TITLE (and Subtitle) FUNDAMENTAL STUDIES OF SUBSONIC AND TRANSONIC FLOW SEPARATION, PART III. THIRD PHASE SUMMARY REPORT | | 5. TYPE OF REPORT & PERIOD COVERED Final Report - November 1975-September 1978 | | | | | | | | | | | | | | | |
| | | 6. PERFORMING ORG. REPORT NUMBER | | | | | | | | | | | | | | | |
| 7. AUTHOR(s) J. M. Wu, A. Vakili-Dastjerd, F. G. Collins, K. C. Reddy, T. H. Moulden, M. K. Bhat, and R. M. Dowgwillo | | 8. CONTRACT OR GRANT NUMBER(s) F40600-76-C-0006 | | | | | | | | | | | | | | | |
| 9. PERFORMING ORGANIZATION NAME AND ADDRESS The University of Tennessee Space Institute Tullahoma, Tennessee 37388 | | 10. PROGRAM ELEMENT, PROJECT, TASK AREA & WORK UNIT NUMBERS Program Element 65807F | | | | | | | | | | | | | | | |
| 11. CONTROLLING OFFICE NAME AND ADDRESS Arnold Engineering Development Center/DOS Air Force Systems Command Arnold Air Force Station, Tennessee 37389 | | 12. REPORT DATE October 1979 | | | | | | | | | | | | | | | |
| | | 13. NUMBER OF PAGES 157 | | | | | | | | | | | | | | | |
| 14. MONITORING AGENCY NAME & ADDRESS (if different from Controlling Office) | | 15. SECURITY CLASS. (of this report) UNCLASSIFIED | | | | | | | | | | | | | | | |
| | | 15a. DECLASSIFICATION/DOWNGRADING SCHEDULE N/A | | | | | | | | | | | | | | | |
| 16. DISTRIBUTION STATEMENT (of this Report) Approved for public release; distribution unlimited. | | | | | | | | | | | | | | | | | |
| 17. DISTRIBUTION STATEMENT (of the abstract entered in Block 20, if different from Report) | | | | | | | | | | | | | | | | | |
| 18. SUPPLEMENTARY NOTES Available in DDC | | | | | | | | | | | | | | | | | |
| 19. KEY WORDS (Continue on reverse side if necessary and identify by block number) <table style="width: 100%; border: none;"> <tr> <td style="width: 33%;">flow separation</td> <td style="width: 33%;">turbulent boundary layer</td> <td style="width: 33%;">numerical Navier-Stokes</td> </tr> <tr> <td>transonic flow</td> <td>incipient separation</td> <td>solutions</td> </tr> <tr> <td>subsonic flow</td> <td>shallow cavities</td> <td>transonic wind tunnel tests</td> </tr> <tr> <td>upper transonic flow</td> <td>wake flow</td> <td></td> </tr> <tr> <td>turbulent flow</td> <td>base flow</td> <td></td> </tr> </table> | | | flow separation | turbulent boundary layer | numerical Navier-Stokes | transonic flow | incipient separation | solutions | subsonic flow | shallow cavities | transonic wind tunnel tests | upper transonic flow | wake flow | | turbulent flow | base flow | |
| flow separation | turbulent boundary layer | numerical Navier-Stokes | | | | | | | | | | | | | | | |
| transonic flow | incipient separation | solutions | | | | | | | | | | | | | | | |
| subsonic flow | shallow cavities | transonic wind tunnel tests | | | | | | | | | | | | | | | |
| upper transonic flow | wake flow | | | | | | | | | | | | | | | | |
| turbulent flow | base flow | | | | | | | | | | | | | | | | |
| 20. ABSTRACT (Continue on reverse side if necessary and identify by block number) <p>The work reported herein represents the third phase of a fundamental study of transonic flow separation with extensive experimental measurements and some numerical Navier-Stokes solutions for high Reynolds number two-dimensional flow. The flow conditions have been extended to include low supersonic free-stream cases. The tests were performed over a Mach number range of 0.6 and 1.32 and Reynolds number range of 4×10^6 to 200×10^6. Simple geometrical surface and flow discontinuities of different sizes (such as ramps, rearward and forward-facing steps, cylinders, etc.) were selected to cause upstream disturbances</p> | | | | | | | | | | | | | | | | | |

UNCLASSIFIED

UNCLASSIFIED

20. ABSTRACT (Continued)

and/or generate downstream adverse pressure gradient regions strong enough to produce local flow separation. The incipient separation angle in flow over ramp compression corner was measured. An average incipient separation angle of 22.5 degrees was confirmed, with no Reynolds number effect in the above range of free-stream flow parameters.

Based on extensive wall static pressure measurements for different geometries and flow conditions, the Mach number and the Reynolds number effects on such characteristics as the separation, the reattachment and the maximum pressures were studied in detail, and correlations between these parameters for different classifications of flows were obtained. It was also observed that by a proper scaling there exists a similarity in surface pressure distributions of transonic flow over airfoil in the attached region between the shock wave and the trailing-edge separation and the attached flow on a rectangular shallow cavity.

The study of development of boundary layer in regions of strong adverse pressure gradients revealed that the transverse pressure gradient is of considerable importance. Consequently, in obtaining a numerical solution for boundary layers in strong pressure gradient regions, the transverse pressure gradient should be considered. It was confirmed by a further study that pressure recovers faster than the velocity along the flow direction downstream of a disturbance. The velocity recovery starts from the wall and spreads outward. Meanwhile, the outer edge of shear layer adjusts to the local external flow quickly. This results in the disturbance effect being maximum in the lower portion of the wake flow. The distance effect on the relaxation process with respect to the disturbance sizes on characteristic pressures downstream of a disturbance was studied and a correlation was obtained including the Mach number effect.

Interaction of normal shock and the turbulent boundary layer was also investigated. There was no separation bubble detected in the region of shock boundary layer interaction at free-stream Mach numbers up to 1.32. High-speed Schlieren motion pictures showed that the normal shock wave was oscillating at a frequency of nearly 200 Hz. The disturbance produced by the normal shock was found to generate less disturbance in the flow field, compared to surface discontinuities type of disturbances.

It has been demonstrated that separated transonic flows, such as flows past rearward and forward-facing steps of a long (or shallow) cavity can be computed using full Navier-Stokes equations. However, the accuracy is rather limited in the separated region behind the rearward-facing step because of the inadequacy of algebraic turbulence model and a lack of sufficient numerical resolutions.

PREFACE

The work reported herein was conducted at The University of Tennessee Space Institute, Tullahoma, Tennessee, and was supported by the Arnold Engineering Development Center under Contract Number F40600-76-C-0006 for the period November 1975 - September 1978. The Air Force project manager during this contract period was Capt. Steve Lamkin, Directorate of Technology.

The reproducibles used in the reproduction of this report were supplied by the authors: J. M. Wu, A. Vakili-Dastjerd, F. G. Collins, K. C. Reddy, T. H. Moulden, M. K. Bhat, and R. M. Dowgwillo.

CONTENTS

| | | <u>Page</u> |
|-------------|---|-------------|
| Chapter 1.0 | INTRODUCTION | 11 |
| 2.0 | DESCRIPTION OF EXPERIMENTAL SETUP AND DATA REDUCTION TECHNIQUE | 14 |
| 2.1 | Wind Tunnel | 14 |
| 2.2 | Model | 17 |
| 2.3 | Shock Holder (Generator) | 18 |
| 2.4 | Instrumentation | 18 |
| 2.5 | Data Acquisition System | 22 |
| 2.6 | UTSI Belt Skin Friction Gage | 24 |
| 2.7 | Data Reduction | 24 |
| 2.8 | Cone Probe | 29 |
| 2.8.1 | Method of Calculating P_{∞} and P_t | 29 |
| 3.0 | FLOW OVER RAMP COMPRESSION CORNERS WITHOUT AND WITH UPSTREAM DISTURBANCE GENERATORS | 35 |
| 4.0 | FLOW OVER FORWARD-FACING STEP | 72 |
| 5.0 | TURBULENT FLOW OVER CAVITIES | 80 |
| 5.1 | Base Pressure | 80 |
| 5.2 | Reattachment Pressure | 84 |
| 5.3 | Plateau Pressure | 84 |
| 5.4 | Separation Pressure | 91 |
| 5.5 | Maximum Pressure | 95 |
| 5.6 | Comparison of Cavity Flow and Transonic Flow Over Airfoil | 101 |
| 6.0 | TURBULENT BOUNDARY LAYER | 112 |
| 6.1 | Law of the Wall and Law of the Wake | 114 |
| 6.2 | Normal Shock-Boundary Layer Interaction | 121 |
| 6.2.1 | Experimental Setup and Results | 127 |
| 7.0 | NAVIER-STOKES SOLUTIONS FOR LONG CAVITIES | 137 |
| 7.1 | A Finite Difference Algorithm for Navier-Stokes Equations | 137 |
| 7.2 | MacCormack's Implicit-Explicit Algorithm | 138 |
| 7.3 | Cavity Flow Computations | 140 |
| 8.0 | SUMMARY AND CONCLUSIONS | 147 |
| 9.0 | LIST OF REFERENCES | 150 |

FIGURES

| | | <u>Page</u> |
|-----------|---|-------------|
| FIGURE 1. | Schematic Diagram of Different Processes of Turbulent Boundary-Layer Separation on an Airfoil (from Ref. 8) | 13 |
| 2. | Sectional View of The University of Tennessee Space Institute Transonic Wind Tunnel | 15 |
| 3. | Experimental Setups. | 19 |
| 4. | Shock Holder and Its Orientation in the Tunnel. | 21 |
| 5. | Pitot and Cone Probes Mounted on Traverse Mechanism. | 23 |
| 6. | UTSI Belt-Skin-Friction Gage | 25 |
| 7. | Cone Probe | 30 |
| 8. | C_p on the Cone Probe at $x/L = .728$ as a Function of Mach Number. | 31 |
| 9. | P_t/P_c vs. Free Stream Mach Number for the Cone of Figure 7. | 33 |
| 10. | Static Pressure in y-Direction in the Immediate Downstream of a Normal Shock Measured by Cone Probe | 34 |
| 11. | Typical Oil Flow Over Ramp Compression Corner. | 36 |
| 12. | Characteristic Parameters of Interest of Flow Over Ramp Compression Corners | 37 |
| 13a. | Influence of Ramp Compression Angle in the Flow Upstream. | 39 |
| 13b. | Influence of Mach Number on a 45° Ramp Compression Corner | 40 |
| 14a. | Variation of Peak Pressure on the Ramps with Mach Number. | 41 |
| 14b. | Plots of Ramp Surface Pressures and Peak Pressure Trend as a Function of Ramp Angle | 42 |
| 15. | Effect of Upstream Small Cylindrical Disturbance on the Surface Pressure Distribution Over the Ramps of Different Angles. | 43 |
| 16. | Effect of Upstream Small Cylindrical Disturbance on the Surface Pressure Distribution Over the Ramps of Different Angles. | 44 |

| | <u>Page</u> |
|--|-------------|
| FIGURE 17. | |
| Effect of Large Cylindrical Upstream Disturbance on the Surface Pressure Distribution Over Ramps of Different Angles. . . . | 45 |
| 18. Effect of Mach Number on Disturbed Flow Over a 45° Ramp. . . . | 46 |
| 19. Distribution of Coefficient of Shearing Stress Across Boundary Layer on a Flat Plate Under Adverse Pressure Gradient Causing Separation (Reference 16) . . | 48 |
| 20. Effect of Relaxation Distance Downstream of a Large Cylindrical Disturbance on the Surface Pressure Distribution Over a Ramp of 30° Angle | 50 |
| 21. Effect of Relaxation Distance Downstream of a Large Cylindrical Disturbance on the Surface Pressure Distribution Over a Ramp of 25° Angle | 51 |
| 22. Comparison of Disturbance Size Effect on the Flow Over a 30° Ramp. | 53 |
| 23. Effect of Backward Facing Step Disturbance on the Surface Pressure Distribution of Flow Over Ramps of Different Angles. . . . | 54 |
| 24. Comparison of Different Disturbances Effect on the Surface Pressure Distribution Over Ramp of 30° Angle | 55 |
| 25. Effect of Relaxation Distance Downstream of a Backward Facing Step on the Surface Pressure Distribution Over a 25° Ramp. | 56 |
| 26. Incipient Separation Angles for Two-Dimensional Ramp Compression Corner. | 58 |
| 27. Separation Length as a Function of the Ramp Angle. | 59 |
| 28. Variations of Peak Pressure Against Free Stream Mach Number | 60 |
| 29. Variation Peak Pressure Over a Ramp Compression Corner with Upstream Disturbance Against Free Stream Mach Number | 62 |

| | <u>Page</u> |
|------------|---|
| FIGURE 30. | |
| | Variation of Peak Pressure Over the Ramp Compression Corner with Upstream Disturbance Against Free Stream Mach Number 64 |
| 31a. | Variation of Peak Pressure on the Ramp Compression Corner with a Backward-Facing Step Down- stream Disturbance Against Free Stream Mach Number 64 |
| 31b. | Comparison of Effect of Various Upstream Disturbance Generators Upon Flow Over Ramp-Compression- Corner. 65 |
| 32. | Peak Pressure Variations on the Ramp Compression Corner a Short Distance Downstream of a Backward-Facing Step Against Free Stream Mach Number 66 |
| 33. | Variation of Peak Pressure Against Nondimensionalized Relaxation Distance. 67 |
| 34. | Variation of Disturbance Strength Against Free Stream Mach Number 69 |
| 35. | Separation Length Plotted Against the Ramp Angle in Presence of Upstream Disturbances of Different Size. 71 |
| 36. | Comparison of Pressure Distributions for Sub-, Trans- and Supersonic Flow Ahead of a Forward-Facing Step. 73 |
| 37. | Static Pressure Distribution in Subsonic Flow Over Forward-Facing Step. 74 |
| 38. | Static Pressure Distribution in Subsonic Flow Over Forward-Facing Step with 0.5-Inch Cylindrical Disturbances. 75 |
| 39. | Static Pressure Distribution in Supersonic Flow Over a Forward- Facing Step with 0.5-Inch Cylindrical Upstream Disturbance. . . . 76 |
| 40. | Schlieren Photograph and Static Pressure Distribution in Subsonic Flow Over Forward-Facing Step with 0.5-Inch Cylindrical Disturbance 78 |

| | | <u>Page</u> |
|------------|---|-------------|
| FIGURE 41. | Schlieren Photograph and Static Pressure Distribution in Supersonic Flow Over Forward-Facing Step with 0.5-Inch Cylindrical Disturbance | 79 |
| 42. | Nondimensional Critical Cavity Length. | 81 |
| 43. | Nomenclature and Schematic Diagram of the Pressure Distribution and the Flow Over a Shallow-Cavity Model. | 82 |
| 44. | A Typical Oil Flow Pattern Upstream and on the Forward-Facing Step. | 83 |
| 45. | Variation of Base Pressure Against Free Stream Mach Number for Shallow Cavity. | 85 |
| 46. | Variation of Base Pressure Normalized with P_t Against Cavity Geometry | 86 |
| 47. | Variation of Base Pressure Normalized with P_∞ Against Cavity Geometry | 87 |
| 48. | Variation of Reattachment Distance with Mach Number. | 88 |
| 49. | Variation of Reattachment Pressure with Free Stream Mach Number for a Shallow Cavity. | 89 |
| 50. | Variation of P_r/P_∞ Against Cavity Geometry. | 90 |
| 51. | Variation of P_r/P_t Against Cavity Geometry. | 90 |
| 52. | Effect of Depth to Length Ratio on the Plateau to Free Stream Pressure Ratio. | 92 |
| 53. | Variation of Plateau Pressure in Flow Over Cavities with Free Stream Mach Number. | 93 |
| 54. | Variation of Plateau Pressure in Flow Over a Shallow Cavity Against Free Stream Mach Number | 94 |
| 55. | Variation of Separation Pressure in Flow Over Shallow Cavity Against Mach Number | 96 |
| 56. | Reynolds Number Effect on the Separation Pressure in Flow Over a Shallow Cavity with the Mach Number Influence. | 97 |

| | <u>Page</u> |
|--|-------------|
| FIGURE 57. Variation Peak Pressure in Flow Over Shallow Cavity Against Mach Number | 98 |
| 58. Comparison of Plateau and Peak Pressure Against Free Stream Mach Number | 99 |
| 59. Variation of P_m/P_p in Flow Over Cavity Against Free Stream Mach Number | 100 |
| 60. Variation of Peak Pressure in Flow Over Cavity Against Geometry of the Cavity. | 102 |
| 61. Variation of Maximum Pressure in Flow Over Cavity Against Free Stream Mach Number. | 103 |
| 62. Numerical Result of $M_\infty = 0.8$ Flow Over a 15% Parabolic Airfoil. | 107 |
| 63. Surface Pressure Distribution Over a 40-Inch Cavity | 108 |
| 64. \tilde{C}_p Plot Obtained from Figure 63 Which Shows Similar Trend With the Region of Interest of Figure 62 | 109 |
| 65. \tilde{C}_p Plot for a 40-Inch Cavity in Free Stream $M_\infty = .718$ | 110 |
| 66. \tilde{C}_p Plot for a 23.5-Inch Cavity in Free Stream $M_\infty = 1.12$ | 111 |
| 67. Comparison of Transverse Pressure Gradient for the Shown Flow Conditions. | 113 |
| 68. Comparison of Velocity Profiles for the Above Flow Conditions | 115 |
| 69. Comparison of Upstream Disturbance Effects on the Velocity Profile 3 Inches in Front of the 25 Degree Ramp. | 116 |
| 70. The Effect of Upstream Disturbance on the Velocity Profile 3 Inches in Front of the 30 Degree Ramp. | 117 |
| 71. Comparison of Upstream Disturbance Effects on the Velocity Profile 3 Inches in Front of the 45 Degree Ramp. | 118 |
| 72. Comparison of Velocity Profiles for the Flow Field Shown. | 122 |

| | <u>Page</u> |
|--|-------------|
| FIGURE 73. Comparison of the Law of the Wall and Law of the Wake for Profiles Shown on Figure 71 | 123 |
| 74. Appearance of Normal Shock Over NACA 0012 Airfoils in Transonic Flow. | 124 |
| 75. Flow Pattern and Pressure Distribution When the Shock is Not Strong Enough to Cause Much Separation. | 125 |
| 76. Flow Pattern and Pressure Distribution With a Strong Shock | 126 |
| 77. Shock Wave Oscillations. | 129 |
| 78. Static Pressure Along the Flat Plate With the Impinging Normal Shock | 130 |
| 79. Velocity Profile Downstream of the Normal Shock. | 132 |
| 80. Plot of the Velocity Profile Downstream of the Shock in the Law of the Wall Law of the Wake Coordinate. | 134 |
| 81. Transverse Pressure Immediately Downstream of the Shock | 136 |
| 82. Grid Used for 40-Inch Long Cavity. . . . | 141 |
| 83. Sketch of the Computational Region for Flow Past a Long Cavity | 144 |
| 84. Pressure Distribution for Flow Past a Cavity (Cavity Length - 40", Cavity Height - 1.25"). | 145 |
| 85. Velocity Vectors Near the Forward Facing Step | 146 |
| 86. Mapping of the Rectangular Mesh in the x-y Plane into the uv Plane | 147 |

APPENDIX

| | <u>Page</u> |
|--|-------------|
| Paragraph I.1 GRID GENERATION FOR FLOW OVER A LONG CAVITY | 155 |

1.0 INTRODUCTION

Since June, 1972, the Gas Dynamics Division of The University of Tennessee Space Institute has been engaged in the study of various turbulent flow separation phenomena that occur at transonic Mach numbers. The previous results are reported in Refs. 1 and 2. The research reported herein is a continuation of that endeavor and is entitled: "Part III — Third Phase Summary Report."

The influence of separation on the aerodynamic characteristics of various fluid dynamic devices has been the subject of numerous investigations. Despite this effort a full understanding of turbulent flow separation phenomena does not exist nor is it possible to correctly predict changes in the local or global flow field properties caused by the separation. The problem is compounded in transonic flows where strong viscous/inviscid interactions exist which are frequently complicated by the formation or interaction with local shock waves and separated flow regions.

Experimental and numerical efforts provide two parallel approaches toward obtaining answers to the many unresolved problems in aerodynamics today. Experimental observations are generally designed to provide clear physical insights into particular problems for which no accurate analytical or numerical solutions exist. The phenomenon of turbulent boundary layer separation, such as occurs on airfoils, wings, compressor blades and inlets, is probably the one flow feature in these devices which has the most pronounced effect on surface loading, pressure recovery, and performance.

Flow separation in two-dimensional flows, to which the present study is restricted, in general occurs as the result of adverse pressure gradients or changes in the geometry of the body. Examples are the flow over forward-facing and rearward-facing steps, respectively. The presence of one of these two factors is essential for two-dimensional flow separation. These separated regions are basically governed by two processes: 'separation' and 'reattachment.' The separation phenomenon in a bounded flow is related to the behavior of the boundary layer flow under the imposed free stream and boundary conditions. The difficulties in theoretically handling separation arise in the application of the 'separation criterion' and often result in mathematical 'singularities' when the boundary layer approximation is employed. Most of the investigations on the essential characteristics of flows with separated

regions have been performed either in subsonic or supersonic flows (Refs. 3, 4, 5, 6 and 7). On the other hand, very few thorough investigations have been performed in the important transonic flow range. Transonic flow is the most sensitive of the flow ranges, especially when it is associated with a strong pressure gradient. Natural phenomena contributing to the transonic flow sensitivity are transition, shock waves, local separation, and discontinuities in the boundary of the flow.

Theoretically the transonic flow sensitivity is associated with the fact that the inviscid flow field equations change their character from one region to the next. This change in character also contributes to most of the difficulties encountered in the numerical solution of inviscid transonic flow. Under certain conditions a disturbance to a local flow field may induce or suppress a downstream flow separation (Ref. 2) which will in turn modify the local and hence the overall flow field over an airfoil or wing. Pearcey, et al. (Ref. 8) have studied transonic shock induced separation and its influence on the flow at the airfoil trailing edge. This has been discussed in our Part II report (Ref. 2). The well-known Type A and Type B flow separation patterns are reproduced and shown in Fig. 1. The influence of the upstream disturbance on the downstream flow condition can be clearly seen. The present work is addressed to the investigation of such transonic flow interactions on some simple geometries. Both experimental and numerical investigations are performed. The experimental studies, performed in the UTSI transonic wind tunnel, examined the influence of upstream disturbance generators upon the flow over a downstream geometry that produced an adverse pressure gradient. Numerical solutions were obtained, using the full Navier-Stokes equations, for the flow over simple geometries that produced separated flow regions and compared to the experimental measurements. The reasons for discrepancies are identified and discussed.

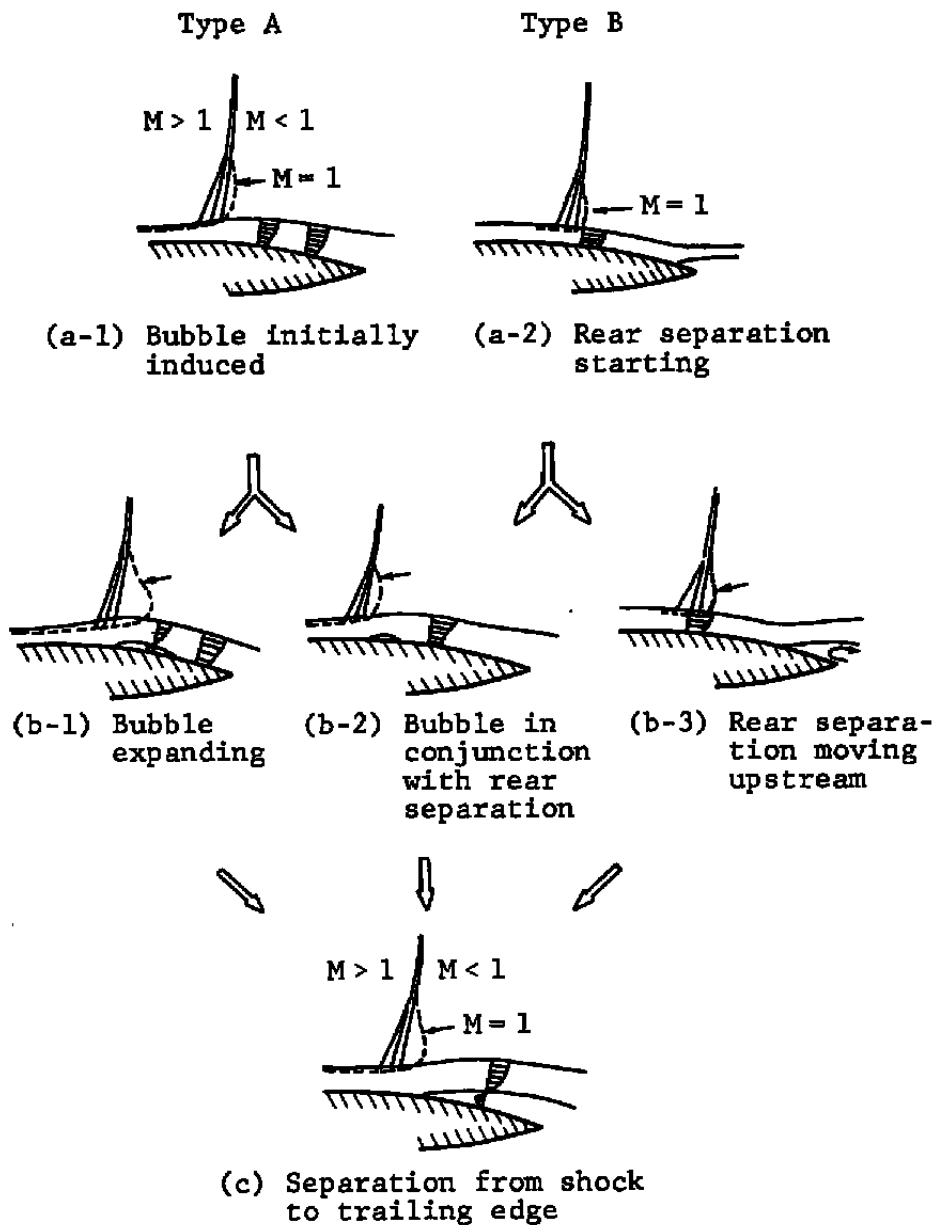


Figure 1. Schematic Diagram of Different Processes of Turbulent Boundary-Layer Separation on an Airfoil (from Ref. 8).

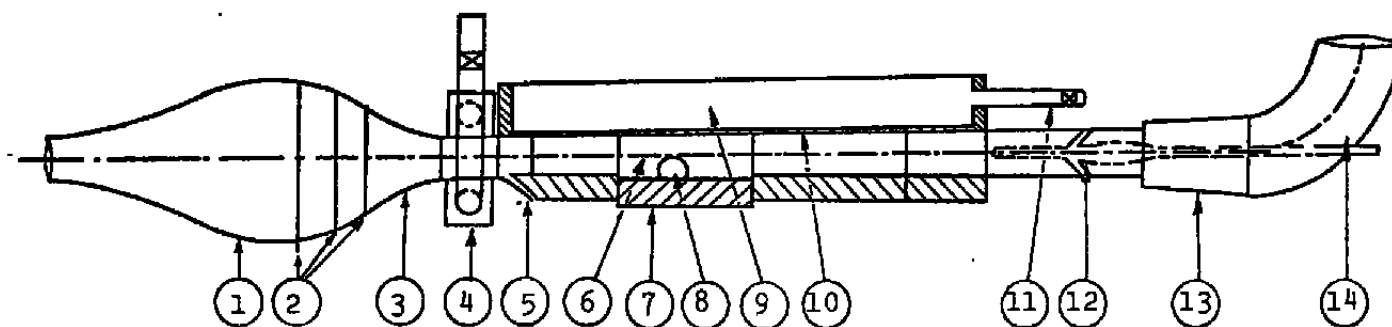
2.0 DESCRIPTION OF EXPERIMENTAL SETUP AND DATA REDUCTION TECHNIQUE

2.1 WIND TUNNEL

This experimental investigation was performed in The University of Tennessee Space Institute (UTSI) transonic wind tunnel. The tunnel is of the blow-down type and has been especially designed for high Reynolds number flow studies (Ref. 9). The nominal cross section of the test section is 12 inches in width, 11 inches in height and has a useful testing length of 144 inches. Details of the UTSI wind tunnel facility can be found in Refs. 9 and 10; therefore, only remarks relevant to the present experiments will be given here. Due to the long length of the test section there is a divergence of about 0.8 degrees along the length of the tunnel to compensate for the thickening of the boundary layer.

Figure 2 gives a cross-sectional view of the tunnel. Before entering the test section the flow passes over a perforated floor-plate section which removes the boundary layer which has developed up to this point, providing a well defined reference point for defining the origin of boundary layers under study. Supersonic Mach numbers ($1.0 < M_{\infty} < 1.4$) are achieved, when desired, by using a perforated-wall type supersonic nozzle (Ref. 10). Control of mass flow through the perforations permits the selection of any low supersonic Mach number, a capability not possible with a non-flexible (solid) wall countoured nozzle. The test section is topped along its entire length with a plenum chamber, which is sealed for subsonic Mach numbers and is vented to the atmosphere via a butterfly valve for supersonic Mach numbers. The perforation distribution in the ceiling plate is designed to minimize flow interferences. Originally a ceiling open ratio of 33 percent was used, but later this was reduced to nearly 15 percent to provide maximum flow uniformity. The test section ends in a variable area section to control mass flow, followed by a diffuser and finally the exhaust stack. Table 1 lists the range of parameters in the UTSI transonic wind tunnel.

Small changes in the test Mach number and Reynolds number occur during individual runs due to the decrease in the stagnation temperature caused by the throttling process of the control valve. Since the stagnation temperature cannot be controlled, average values of the related parameters were used for the data analysis. The tunnel wall temperature also decreases during each run, but the wall-to-free stream temperature ratio, T_w/T_t , was assumed to be



- | | | | |
|---|----------------------|----|--------------------------------|
| 1 | Settling Chamber | 8 | Schlieren Window |
| 2 | Smoothing Screens | 9 | Plenum Chamber |
| 3 | Contraction Cone | 10 | Perforated Ceiling |
| 4 | Supersonic Nozzle | 11 | Plenum Ventilation Pipe |
| 5 | B. L. Suction Device | 12 | Translating Centerbody (Choke) |
| 6 | Test Section | 13 | Diffuser |
| 7 | Typical Floor Plate | 14 | Exhaust Stack |

Figure 2. Sectional View of The University of Tennessee Space Institute Transonic Wind Tunnel.

TABLE 1
OPERATIONAL CONDITIONS OF THE UTSI TRANSONIC TUNNEL

| Parameters | Operational Conditions |
|---|--|
| Mach number range | $0.50 \leq M_{\infty} \leq 1.40$ |
| Unit Reynolds number range | $5 \times 10^6 \leq Re/ft \leq 3 \times 10^7$ |
| Reynolds number range based on length from leading edge | $4 \times 10^6 \leq Re_L \leq 2 \times 10^8$ |
| Maximum temperature drop (°C) for 10 sec. | 10 |
| Subsonic flow uniformity in test section | $\Delta M/M \leq \pm 0.2\%$ in transverse direction $\Delta M/M \leq \pm 3.5\%$ longitudinal direction ($27.5 \leq x \leq 74$ ") |
| Maximum flow rate (lb/sec) | 190 |
| Normal running time (sec) | $10 \leq t \leq 60$ ($1.4 \geq M_{\infty} \geq 0.6$) |
| Minimum running stagnation pressure (psia) | $19 \leq P_0 \leq 42$ ($0.6 \leq M_{\infty} \leq 1.4$) |
| Surface finish roughness (μ in.) | 63 |
| Approximate turbulence fluctuation level (percent freestream velocity) | ± 5 |

constant and about equal to one. That is, adiabatic wall conditions were assumed. Actually, there was a slight amount of heat transfer from the tunnel floor to the boundary layer. The wall temperature was experimentally measured and was found to decrease at an average rate of 2° F/sec. during the steady-state condition. The unit Reynolds number was varied from run to run by changing the stagnation pressure. The subsonic Mach number was controlled by the downstream choke location, which changes the downstream tunnel area. For supersonic Mach numbers the choke was set for maximum area and the Mach number was set by the amount of mass removed from the perforated nozzle.

The quality of the flow in the test section of the tunnel was examined by making measurements of the flow properties (Ref. 11). Table 2 indicates rough averages of the computed uncertainties of the properties in the free stream. q_{∞} is the dynamic pressure. In isolated cases computed uncertainties of the mean of the properties can exceed 0.5 percent while instantaneous variations can reach ± 3 percent.

TABLE 2. TYPICAL COMPUTED UNCERTAINTIES
IN FREE STREAM CONDITIONS

| Free Stream Variable | Typical Computed Uncertainty, % | |
|-----------------------------|------------------------------------|--------------------|
| | of the Mean | Single Measurement |
| P_{∞} (psia) | $\pm .15$ | ± 1.04 |
| P_t (psia) | $\pm .25$ | ± 1.70 |
| M_{∞} | $\pm .25$ | ± 1.70 |
| q_{∞} (psia) | $\pm .20$ | ± 1.40 |
| Re_{∞} (ft $^{-1}$) | $\pm .40$ | ± 2.8 |

2.2 MODEL

The notable feature of the UTSI tunnel is the use of the test section floor as the model. Since the effective length of test section is 144 inches, Reynolds numbers (based on length) very close to flight Reynolds numbers can be achieved. For the purpose of this study two families of bodies were manufactured to be used in conjunction with the floor plate to make the models. The first were upstream disturbance generators consisting of: a shock generator, circular cylinders of diameters 0.5 and 1.25 inches,

backward-facing steps of heights 0.5, 1.0, and 1.25 inches and a normal impinging shock. The second were adverse pressure gradient generators consisting of: forward-facing steps of heights 0.5, 1.0, and 1.25 inches, and ramps of different angles of 25, 30, and 45 degrees. Figure 3 shows the experimental setup. For each of these arrangements several runs with different free stream conditions were made. A Mach number and Reynolds number matrix were examined for each model to investigate the effects of Mach number and Reynolds number on the parameters of interest.

2.3 SHOCK HOLDER (GENERATOR)

For the study of a normal shock-boundary-layer interaction the generation of a normal shock was necessary. There are many ways of generating a normal-impinging shock on a flat plate in supersonic flow, most of which require the installation of an object in the tunnel free stream or on the tunnel ceiling. However, interactions between the external object and the free stream can generate unwanted disturbances which occasionally dominate the entire flow field. It is generally difficult to obtain a normal shock and produce no extra interference in the flow. The geometry and location above the wall of the present model (Fig. 4) were determined to minimize the flow interference while producing a normal shock at the tunnel wall. Recompression at the end of the holder, however, remained a problem.

2.4 INSTRUMENTATION

Many static pressure tubes were built into the surface of each model along its centerline. A pre-arranged selection of 47 static pressures was measured three times during each run, plus some five other static pressures which were monitored 16 times a second. The pressure orifices were normally spaced one inch apart, except in regions of special interest. For example, in the separation and reattachment regions and in the foot of the shock more detailed measurements were necessary. In these regions, depending on the orifice availability, some of the orifices were spaced as close as 0.2 inches of each other. The static pressure orifices had an internal diameter of .04 inch, nearly 20 times smaller than the undisturbed boundary layer thickness. Static pressures were measured by a pressure transducer which was connected to a 48-port Scanivalve. The valve mechanism was operated electronically and connected each port in sequence to the transducer. The Scanivalve was operated with a sampling rate of 16 ports

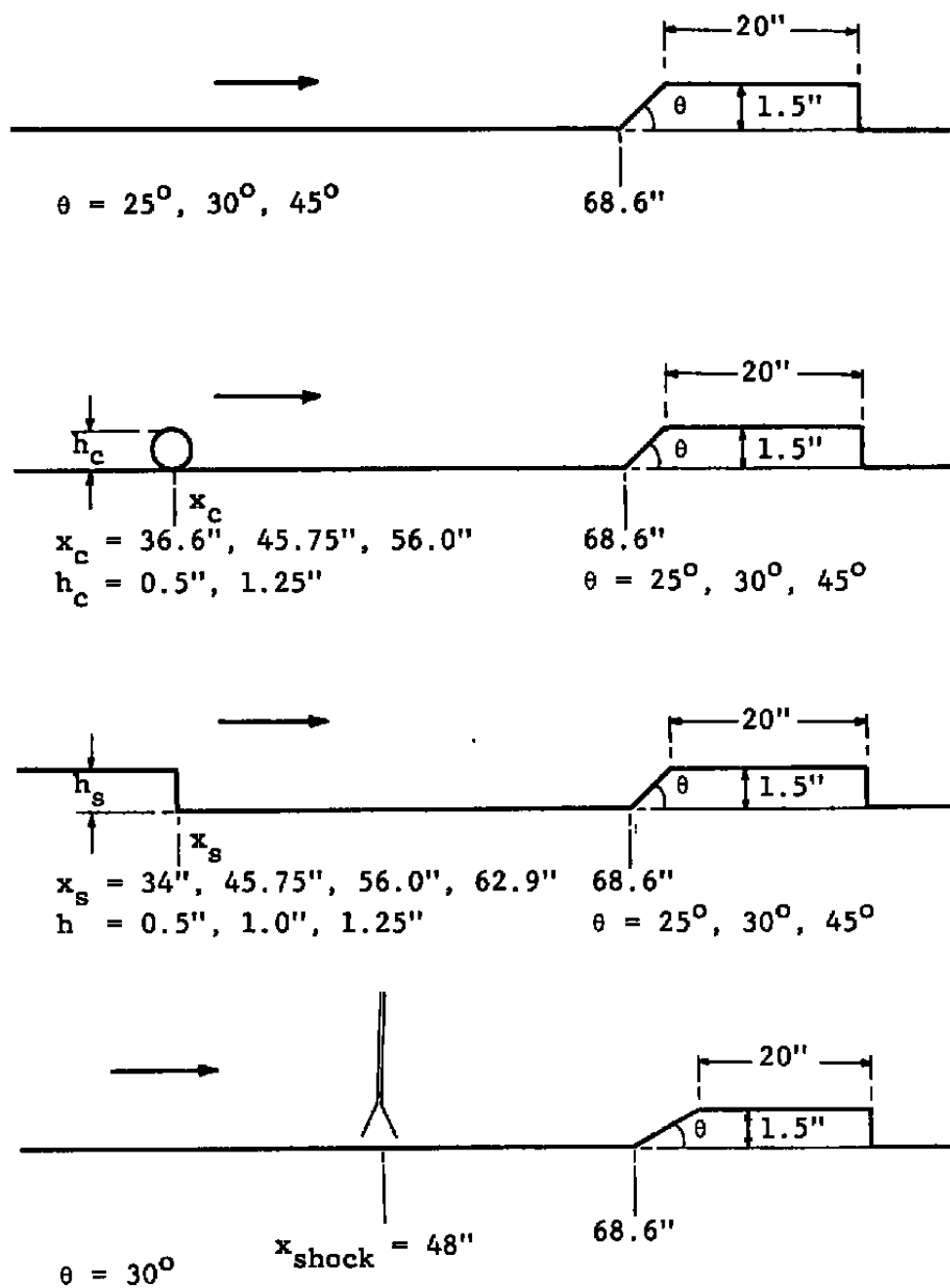


Figure 3. Experimental Setups.

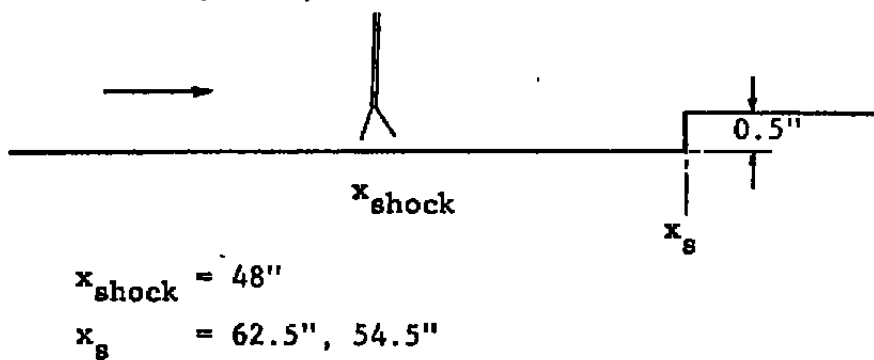
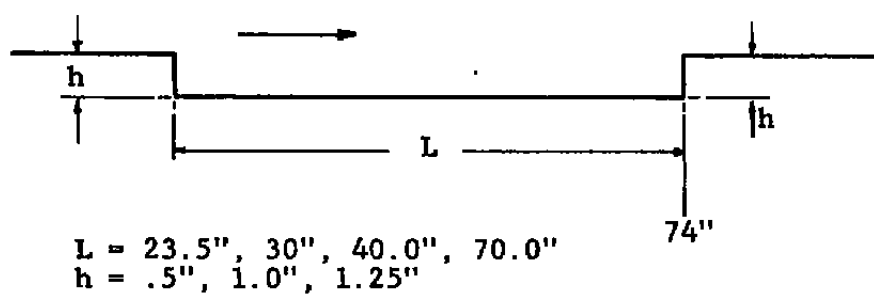
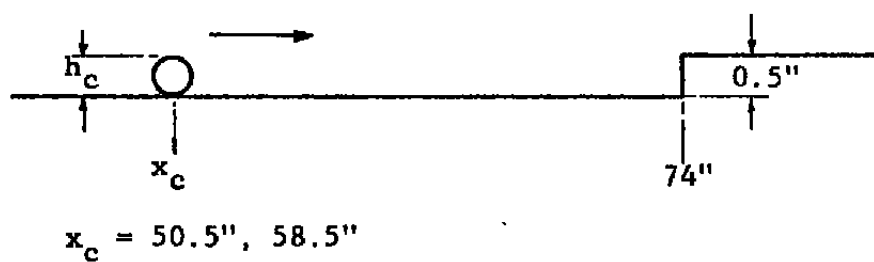


Figure 3. (Continued)

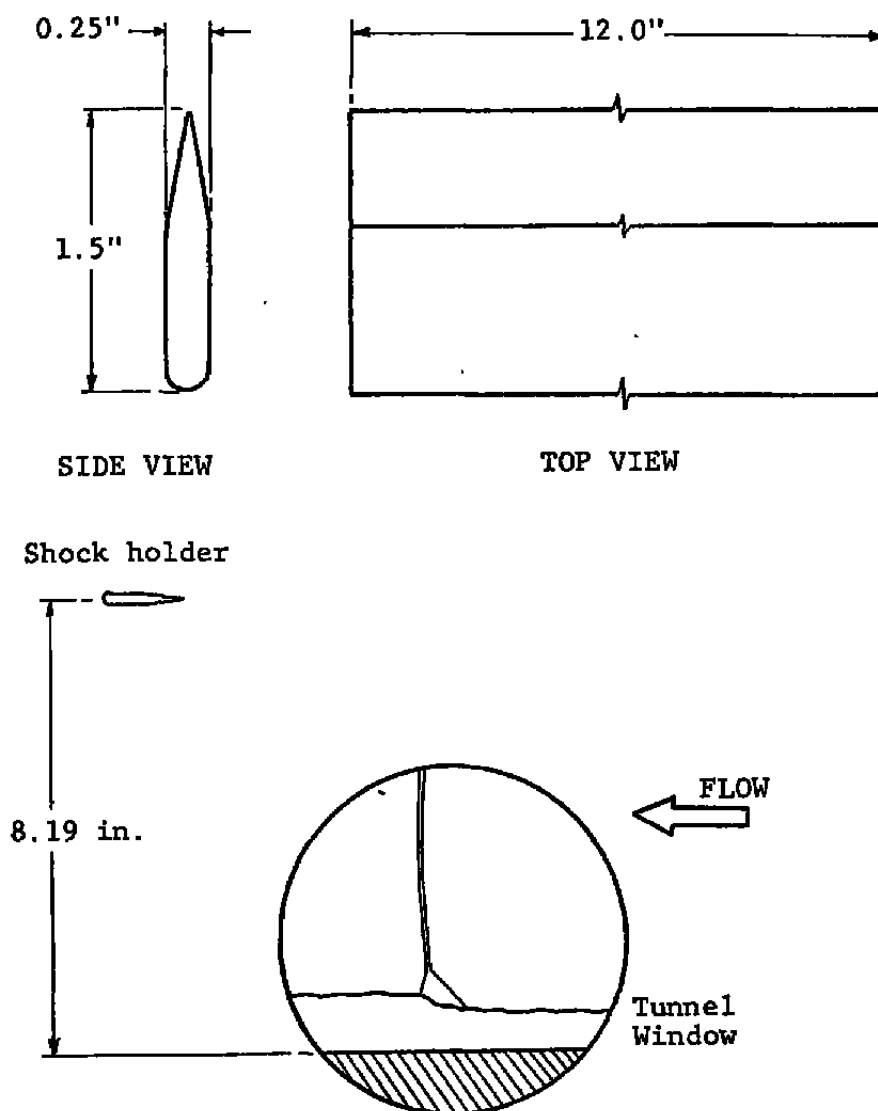


Figure 4. Shock Holder and Its Orientation in the Tunnel.

per second, requiring three seconds to read the surface pressure distribution on a model. Three scans were normally measured during each test and the average of the measurements during each scan were obtained. The measurements obtained during the scan with the steadyest pressure were used for the data analysis. The wall static pressure at a fixed location could drop by as much as 0.5 psi during a scan duration.

The velocity boundary layer was measured using the traversing probe shown in Fig. 5. This probe simultaneously measured the total and static pressures using pitot and cone probes, respectively. The cone probe was made from a 10 degree half-angle conical tip containing four circular holes 0.009 inches in diameter, spaced 90 degrees from each other at a distance of 0.134 inches from the tip of the cone. It was mounted 1.5 inches apart from the pitot probe to minimize interference, as shown on Fig. 5. The traversing pitot probe had an opening of 0.016 inches in diameter. This assembly could be traversed a maximum of 3.5 inches and its instantaneous position was measured by a Burns linear potentiometer which was calibrated before each test. Two fixed pitot probes were used to measure the stagnation pressure in the tunnel, one inside the stilling chamber and the other located at $x = 29$ inches in the test section. Skin friction was measured during a limited number of runs by a new skin friction gage developed at UTSI (Ref. 10). The flat plate skin friction measurements gave consistently higher C_f values than the calculations. Partly, this increase may be thought to indicate a free stream turbulence level of about 5 to 10 percent (Ref. 11). There may have also existed a systematic error in the instrument to be identified later, using known flow conditions. Visualization techniques such as schlieren/shadow-graph photography and oil flow were normally used to provide qualitative information about the flow patterns.

2.5 DATA ACQUISITION SYSTEM

The important component of the data acquisition system was a customized microcomputer based on the Z-80A system.

Transducer output signals were introduced into a 16-channel A/D (12 bit) converter (with multiplexing at 35 kHz maximum rate and a sample and hold). The digital signals were stored in a Z-80, 48K, 8 bit microprocessor and a 92K floppy disk. The microprocessor also controlled various aspects of the experiment. To increase the number of data points one input channel was connected to a 48-channel Scanivalve (16 Hz data rate) and one to a 25-channel thermocouple scanner.

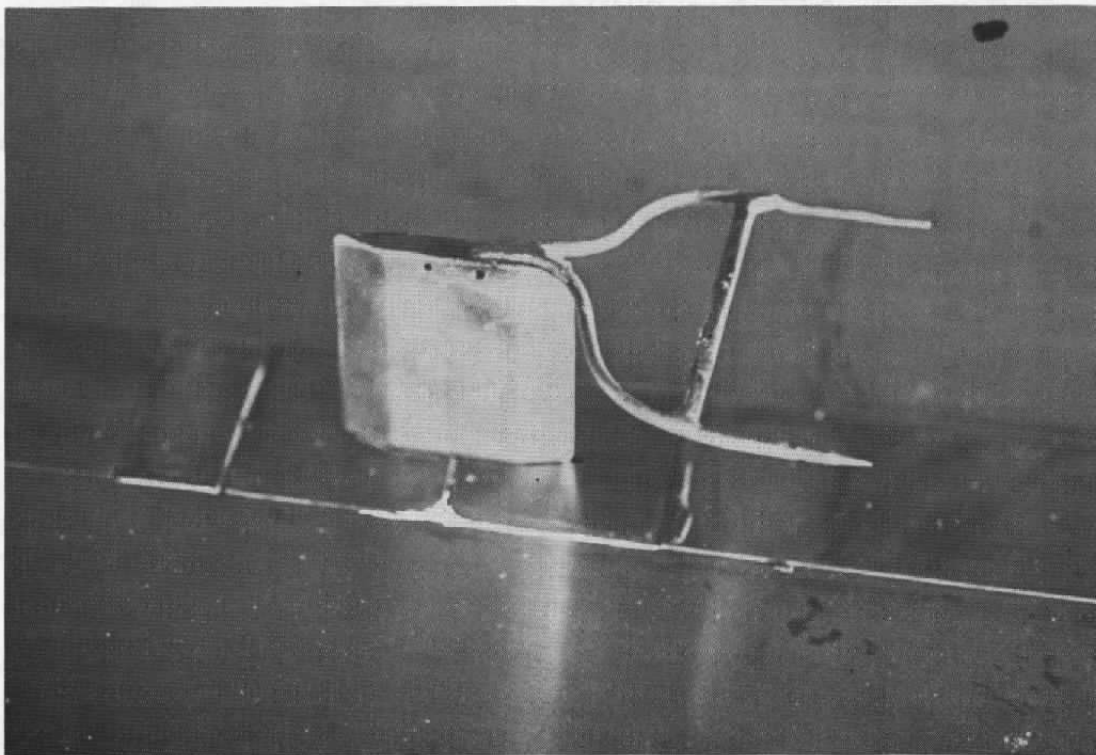


Figure 5. Pitot and Cone Probes Mounted on Traverse Mechanism.

The data was transmitted, using a Teletypewriter, over 'phone lines to the UTSI computer (DEC 11T55), where it was stored on disk memory. The data would then be analyzed and plotted by command from the wind tunnel.

2.6 UTSI BELT SKIN FRICTION GAGE²

A new instrument was invented and manufactured at UTSI to measure the skin friction forces directly and mechanically. This device consists of a flexible belt (tape) which is wrapped continuously and tightly over two cylinders separated by a small distance. A portion of the belt replaces the surface over which the fluid flows such that the force exerted by the fluid on the surface is transmitted to the belt, causing it to rotate the cylinders. These cylinders are mounted on frictionless flexures which are mounted rigidly in a solid frame (see Fig. 6). Strain gages are installed on both sides of the vertical flexure web to measure the amount of torque applied to the cylinders. The stiffness of the flexure web was selected to limit the amount of angular deflection per one gram-force exerted on the belt to not more than one degree. For situations with higher shear stress forces than are measured in the UTSI tunnel, special flexures with thicker webs would be required.

Because of the symmetrical design of the instrument, it can be used in either a vertical or horizontal orientation. To calibrate, the instrument is held vertically and various dead weights are hung to one end of a very thin nylon thread that is attached to the sensing surface while the output of the gage is recorded. The instrument is calibrated by increasing and decreasing the amount of dead weight to make sure of the perfect linearity of the instrument.

Further details about the data acquisition can be found in Charboneau (1976) (Ref. 12).

2.7 DATA REDUCTION

The equations that were used to calculate the flow variables using the measurements are given in this section.

The local Mach number was calculated from the isentropic flow relation:

²Patent pending.

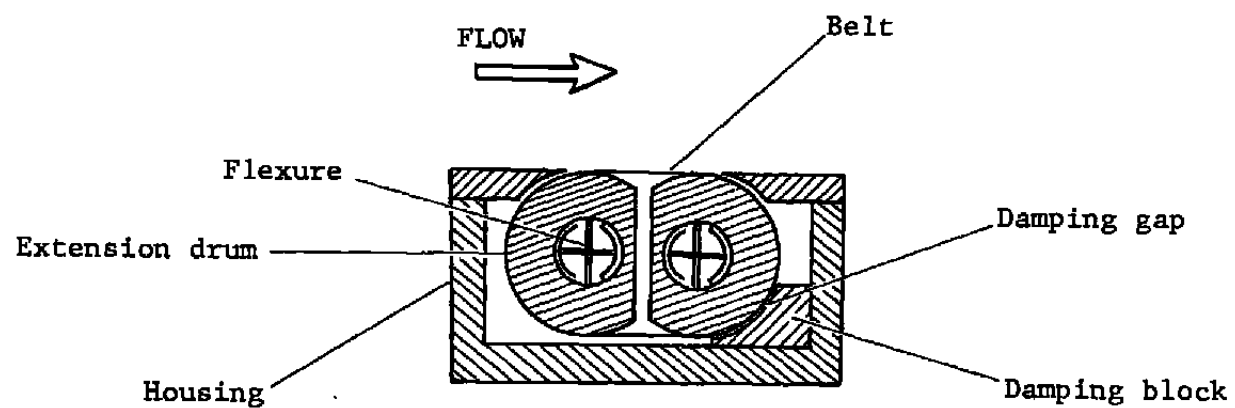


Figure 6. UTSI Belt-Skin-Friction Gage.

$$M = \left\{ \left[\left(\frac{P_t}{P_s} \right)^{\frac{\gamma-1}{\gamma}} - 1 \right] \frac{2}{\gamma+1} \right\}^{1/2}$$

with total pressure P_t , static pressure P_s and $\gamma = 1.4$.
If conditions were supersonic, the Rayleigh pitot equation

$$\frac{P_t}{P_s} = \left[\left(\frac{\gamma+1}{2} \right) M^2 \right]^{\frac{\gamma}{\gamma-1}} \left[\frac{\gamma+1}{2\gamma M^2 - (\gamma-1)} \right]^{\frac{1}{\gamma-1}} \quad (1)$$

was solved for the Mach number by Newton-Raphson iteration. The presence of subsonic, sonic or supersonic flow conditions was determined by

$$\frac{P_t}{P_s} \text{ less than, equal to or greater than } \left(\frac{\gamma+1}{2} \right)^{\frac{\gamma}{\gamma-1}}$$

respectively. Pressure coefficients with respect to the free stream conditions were calculated using the definition

$$C_p = \frac{P - P_\infty}{q_\infty} = \frac{P - P_\infty}{\frac{1}{2} \gamma P_\infty M_\infty^2}$$

The total pitot pressure was corrected for normal shock effects at supersonic Mach numbers by solving the following equation for P_{t2} :

$$\frac{P_{t2}}{P_{t1}} = \left[\frac{(\gamma+1)M^2}{(\gamma-1)M^2 + 2} \right]^{\frac{\gamma}{\gamma-1}} \left[\frac{\gamma+1}{2\gamma M^2 - (\gamma-1)} \right]^{\frac{1}{\gamma-1}} \quad (2)$$

The Reynolds number per foot was found using

$$Re/ft = \frac{1.7784 \times 10^9 P_{t_\infty} M_\infty}{(T_{t_\infty} + 460)^{1.315} (1 + .2 M_\infty^2)^{2.185}} = f(M_\infty, P_{t_\infty}, T_{t_\infty})$$

with the total pressure in psia and total temperature in °F. This equation was obtained by fitting a curve to measured viscosity data for air. A total temperature of 40°F, which was approximately the average temperature observed, was used if there was no total temperature data available. The velocity ratio is calculated by:

$$\frac{U}{U_e} = \frac{M}{M_e} \left(\frac{T}{T_e} \right)^{1/2} \quad (3)$$

where e indicates conditions at the edge of the boundary layer.

For an adiabatic wall, the temperature and velocity ratios are related by (Whitfield and High, 1974)

$$\begin{aligned} \frac{T}{T_e} = & 1 + \frac{(\gamma-1)}{2} M_e^2 \left[1 - \left(\frac{u}{u_e} \right)^2 \right] + (1 - P_{r_m}) \\ & \left\{ \frac{\beta(\gamma-1)}{(\alpha+1)(\alpha+2)} M_e^2 \left[1 - \left(\frac{u}{u_e} \right)^{\alpha+2} \right] + \frac{\gamma-1}{2} M_\infty^2 \left[1 - \left(\frac{u}{u_e} \right)^2 \right] \right. \\ & \left. + f(1) - f\left(\frac{u}{u_e} \right) \right\} \end{aligned} \quad (4)$$

where

$$\begin{aligned} f\left(\frac{u}{u_e} \right) = & \frac{\Delta}{(\gamma-1)M_e^2} \left[(\zeta-\Delta) \ln |\zeta-\Delta| - (\zeta+\Delta) \ln |\zeta+\Delta| \right] \\ \zeta = & -(\gamma-1)M_e^2 \frac{u}{u_e} \\ \Delta = & \left[2(\gamma-1)M_e^2 \frac{T_{t,e}}{T_e} \right]^{1/2} \end{aligned} \quad (5)$$

and where sub e indicates the edge of shear layer condition.

The mixed or "turbulent Prandtl number is defined by

$$Pr_m = \frac{C_p(\mu + \mu_t)}{(\kappa + \kappa_t)}$$

and the parameters α and β are taken to be

$$\alpha \equiv (5/2)m|_{m=10} = 25$$

$$\beta \equiv 10m|_{m=10} = 100$$

where m is the coefficient for this relation

$$\frac{u}{u_e} = \left(\frac{y}{\delta}\right)^{1/m}$$

The velocity ratio was then found by solving Equations (3) and (4) simultaneously by iteration. A different but equally involved relationship between the temperature and velocity exists for the constant temperature wall. Since the boundary layer data were routinely evaluated assuming an adiabatic wall, the constant temperature wall expression is not given here.

Boundary layer thickness, δ , is defined as

$$\delta = y|_{\frac{u}{u_e} = .99}$$

The boundary layer displacement thickness, δ^* , is defined as

$$\delta^* = \int_0^{\delta} \left(1 - \frac{\rho_u}{\rho_e} \frac{u}{u_e}\right) dy$$

and the momentum thickness as

$$\theta = \int_0^{\delta} \left(\frac{\rho_u}{\rho_e} \frac{u}{u_e}\right) \left(1 - \frac{u}{u_e}\right) dy$$

Both are evaluated by numerical integration using the trapezoidal rule. The shape factor H is then defined as $H = \delta^*/\theta$.

2.8 CONE PROBE

The measurement of static pressure was carried out using a cone probe. A typical cone probe is shown in Fig. 7. The semi-vertex angle of this cone was $\delta = 9.38^\circ$ and the location of the pressure orifices was at $x/L = 0.72826$. The surface pressure (P_c) at the above location on the above cone was recorded while simultaneously the total pressure was measured using a pitot probe.

2.8.1 METHOD OF CALCULATING P_∞ AND P_t

From the above measurements the static and total pressure were calculated as follows:

The pressure coefficient $C_p = (P_c - P_\infty)/q_\infty$ for the above cone with the corresponding pressure tap location was calculated for subsonic and transonic Mach numbers (up to the Mach number for which the shock attached) using the program of Wu, et al. (Ref. 13). For the supersonic Mach numbers for which the shock was attached the C_p was calculated using the charts in Ref. 14. Thus C_p as a function of M_∞ for the above cone and pressure tapping location was tabulated and is plotted in Fig. 8. Next the ratio P_t/P_c of the measured total and static pressure was calculated.

For subsonic Mach numbers ($M_\infty < 1$) M_∞ was calculated from

$$\frac{P_t}{P_c} = \frac{\left(1 + \frac{\gamma-1}{2} M_\infty^2\right)^{\frac{\gamma}{\gamma-1}}}{1 + \frac{\gamma}{2} C_p M_\infty^2} \quad (6)$$

For supersonic Mach numbers, the measured total pressure was corrected for the normal shock in front of the pitot tube. M_∞ in this case was calculated from

$$\frac{P_t}{P_c} = \frac{\left(\frac{\gamma+1}{2} M_\infty^2\right)^{\frac{\gamma}{\gamma-1}}}{\left(1 + \frac{\gamma}{2} C_p M_\infty^2\right) \left(\frac{2}{\gamma+1} M_\infty^2 - \frac{\gamma-1}{\gamma+1}\right)^{\frac{1}{\gamma-1}}} \quad (7)$$

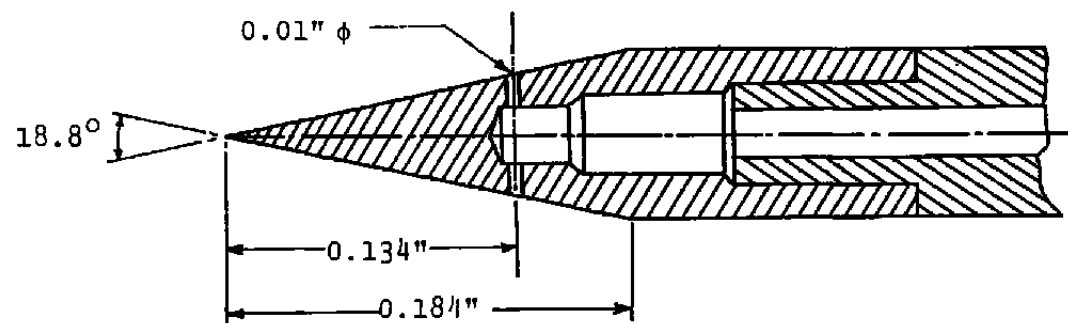


Figure 7. Cone Probe.

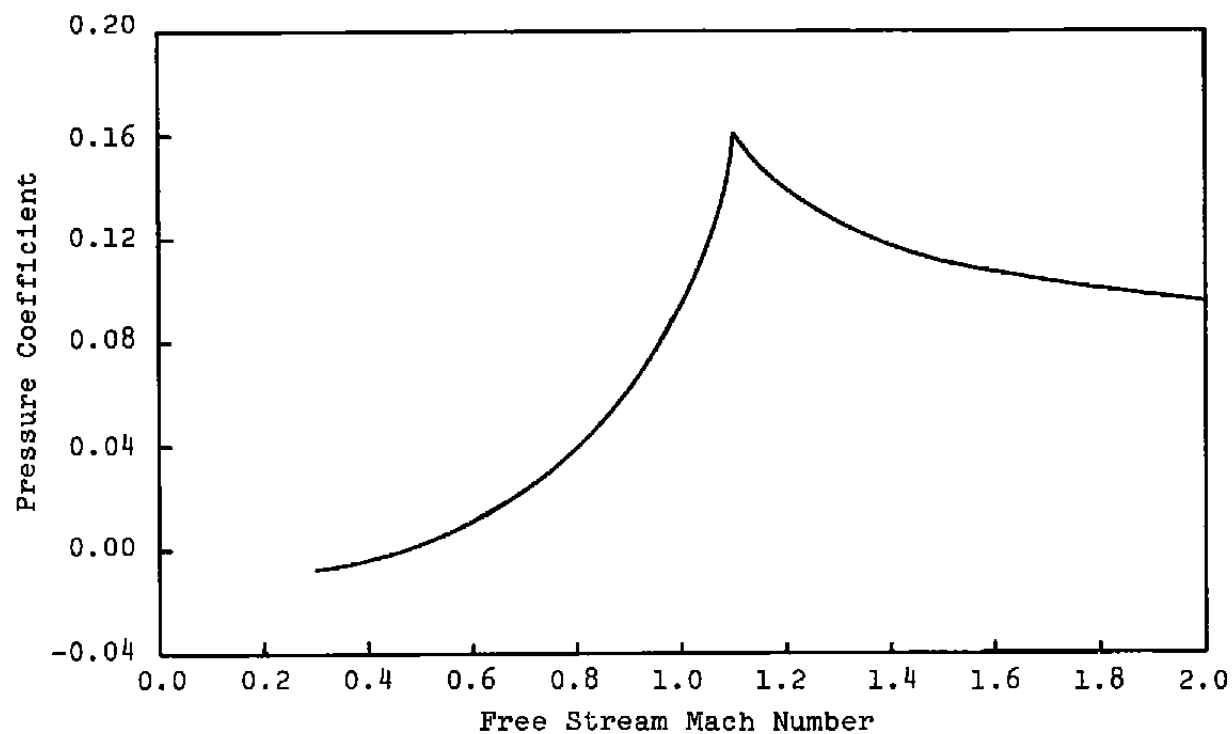


Figure 8. C_p on the Cone Probe at $x/L = .728$
as a function of Mach Number.

Alternatively a table of M_∞ vs. P_t/P_c was formed from the relations (6) and (7). For

$$\frac{P_t}{P_c} = \frac{\left(\frac{\gamma+1}{2}\right)^{\frac{\gamma}{\gamma-1}}}{\left[1 + \frac{\gamma}{2} C_p\right]} = 1.7744818$$

the relation (6) was used. For a given ratio of P_t/P_c , M_∞ would be calculated from the above table by interpolation. A plot of M_∞ vs. P_t/P_c is shown in Fig. 9.

Having calculated M_∞ , P_∞ was calculated using the isentropic relation

$$\frac{P_t}{P_\infty} = \left(1 + \frac{\gamma-1}{2} M_\infty^2\right)^{\frac{1}{\gamma-1}}$$

For subsonic Mach numbers P_t is the measured total pressure and for supersonic Mach numbers, P_t was calculated from the measured total pressure P_o using the relation

$$\frac{P_t}{P_o} = \left(\frac{2\gamma}{\gamma+1} M_\infty^2 - \frac{\gamma-1}{\gamma+1}\right)^{\frac{1}{\gamma-1}} \left(\frac{1 + \frac{\gamma-1}{2} M_\infty^2}{\frac{\gamma+1}{2} M_\infty^2}\right)^{\frac{\gamma}{\gamma-1}}$$

A sample calculation from the measurement of a cone probe traverse through the boundary layer on a flat plate downstream of a normal-impinging shock is shown in Fig. 10.

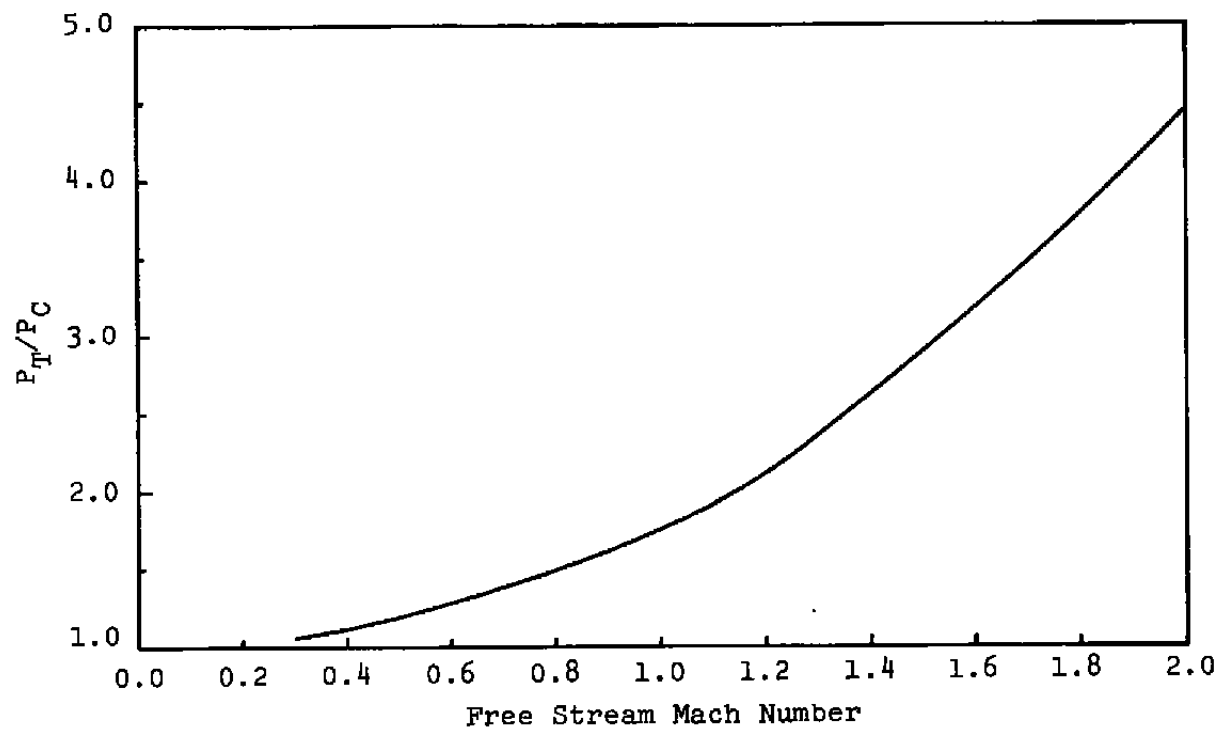


Figure 9. P_t/P_c vs. Free Stream Mach Number
for the Cone of Figure 7.

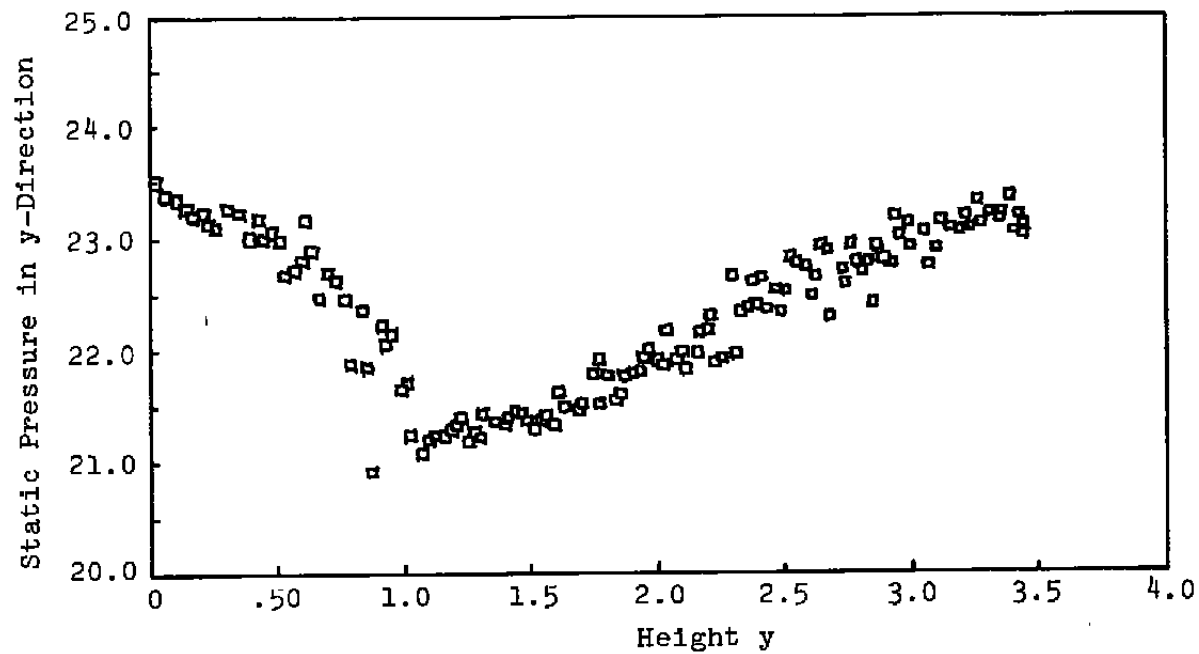


Figure 10. Static Pressure in y-Direction in the Immediate Downstream of a Normal Shock Measured by Cone Probe.

3.0 FLOW OVER RAMP COMPRESSION CORNERS WITHOUT AND WITH UPSTREAM DISTURBANCE GENERATORS

In recent years the two-dimensional supersonic and subsonic flow over ramp-compression-corners has been studied by many other investigators. This simple geometry permits detailed studies of the turbulent boundary layer in the region of adverse pressure gradient. In addition, normally there are fewer difficulties associated with three-dimensionality and flow unsteadiness with this configuration compared to alternative methods of producing an adverse pressure gradient such as with an incident shock wave.

In this series of experiments the flow over forward-facing ramps of many different angles was tested. A fairing plate 20 inches long was used downstream of the ramps. It was assumed that there was no upstream influence from the end of the extension plate to the flow field over the ramp. The purpose of the ramps was to generate different pressure gradients in the approaching flow. In most of the experiments, surface oil flow visualization techniques were used to indicate separation and reattachment locations in front of and on the ramps, respectively. The oil flow also indicated corner effects which directly exhibited the extent of two-dimensionality of the flow. In almost every case, the flow over the ramps was admissibly two-dimensional. The flow in the region close to where the ramps and other models met the tunnel wall was three-dimensional and the existence of three-dimensionality was clear due to the presence of a vortex pattern in the oil flow on the floor plate and sidewalls. However, the centerline region was two-dimensional in most of the tests. Three-dimensionality effects were not studied in this work (a typical oil flow picture is shown in Fig. 11).

Velocity profiles were measured at several distances upstream of the ramps to make it possible to study the effect of the ramp on the boundary layer. However, it was later found that additional velocity profiles had been necessary. Especially, the velocity profile ahead of the interaction should have been measured every time. For each ramp of a fixed angle, upstream disturbance generators of various size and geometry, such as cylinders of 0.5-inch and 1.25-inch diameters and a backward-facing step of 1.25 inch height were placed at different locations upstream of the ramp. Figure 12 shows the characteristic parameters of interest for the flow over ramp-compression-corners with and without upstream disturbances.

In previous work by this group (Ref. 15), a mean value of the incipient separation angle equal to 22.5 degrees



Figure 11. Typical Oil Flow Over Ramp Compression Corner.

was observed for flow in a Mach and Reynolds number range similar to that of this study.

To obtain reference flow patterns for this series of experiments, the flow over ramp-compression-corners of 25, 30, and 45 degrees was studied again, without upstream disturbances. Typical results are shown in Fig. 13. The static pressure distribution for flow at $M_\infty \sim 0.81$ over the three ramps of different angles is shown in Fig. 13a and the flow over the 45 degree ramp at three Mach numbers is shown in Fig. 13b. Since the Reynolds number variation is small among the tests shown in these figures its effect is assumed to be secondary to the primary effect of ramp angle and Mach number.

The properties of the static pressure distribution on ramp-compression-corners, as found from these results and in the previous work of this group (Ref. 15), can be summarized as follows. The influence of the ramp on the wall static pressure is felt many boundary layer thicknesses upstream of the ramp location. The wall static pressure rise reaches a peak value on the ramp and then decreases gradually until the top corner of the ramp. At the top of the ramp a sudden pressure expansion is observed and thereafter the flow compresses to the free stream undisturbed pressure. The peak pressure increases with an increase in ramp angle and Mach number (Fig. 14a). The peak pressure location moves up the ramp as the ramp angle increases (Fig. 14b). The peak pressure occurring on the ramp is due to the kinetic energy of the separated shear layer at the reattachment point on the ramp. The increase in peak pressure with the increase of ramp angle and Mach number are indications for the above statement. Therefore, a fuller velocity profile will result in a higher peak pressure on the ramp. From here it can be concluded that as the Reynolds number increases the peak pressure should also increase.

As previously indicated, in the present work the influence of various upstream disturbance generators on the flow over ramps was studied. By placing a 0.5-inch diameter cylinder at station $x = 36.6$ inches, 32 inches upstream of the beginning of the ramp, the peak pressure for all ramp angles decreased drastically compared to the pressure without the disturbances (Fig. 15). Similar results were observed when this cylindrical disturbance generator or a larger cylinder of 1.25-inch diameter were placed at nearly 23 inches upstream of the beginning of the ramps (Figs. 16 and 17). The effect of Mach number on the disturbed flow is shown in Fig. 18. This is because the upstream disturbance generator disturbs the velocity profile

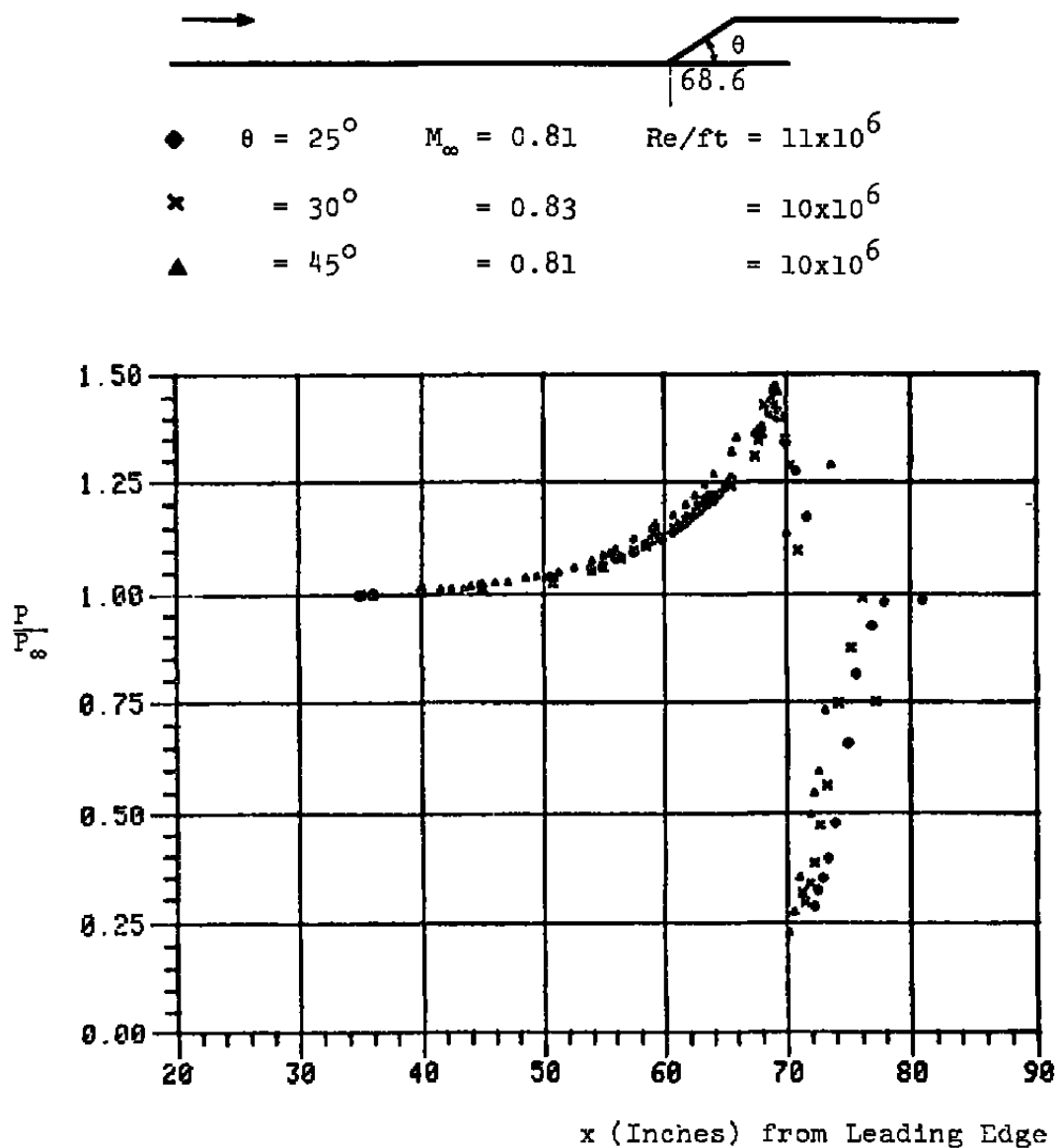


Figure 13a. Influence of Ramp Compression Angle in the Flow Upstream.

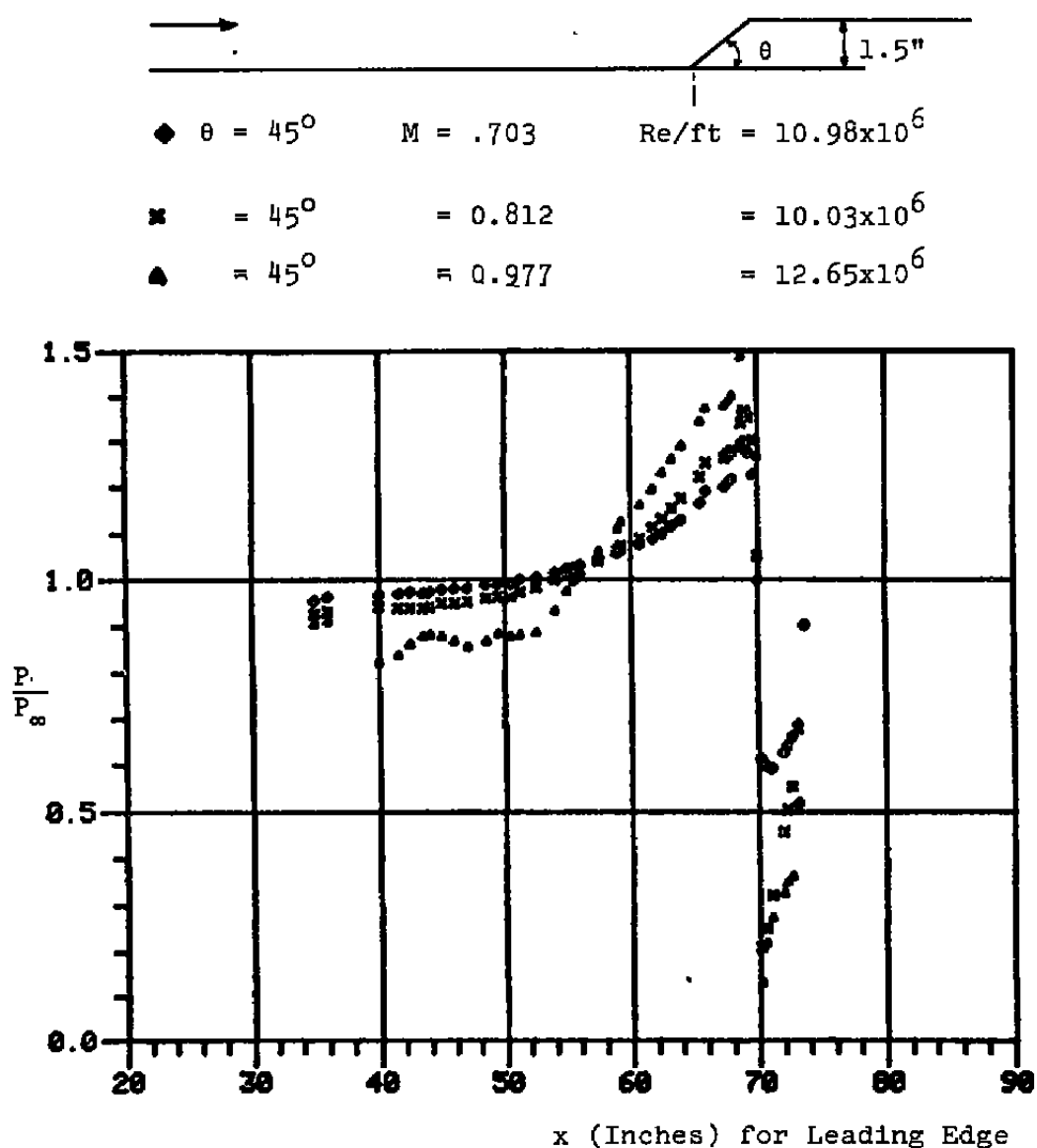


Figure 13b. Influence of Mach Number on a 45° Ramp Compression Corner.

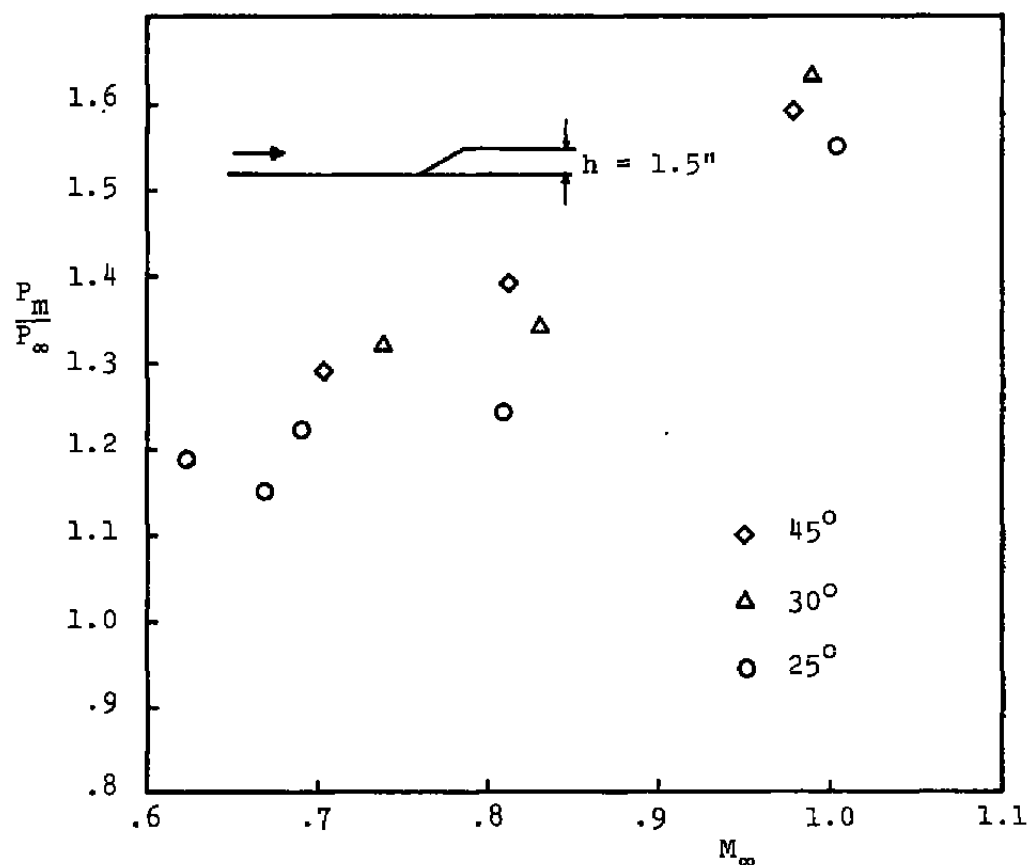


Figure 14a. Variation of Peak Pressure on the Ramps with Mach Number.

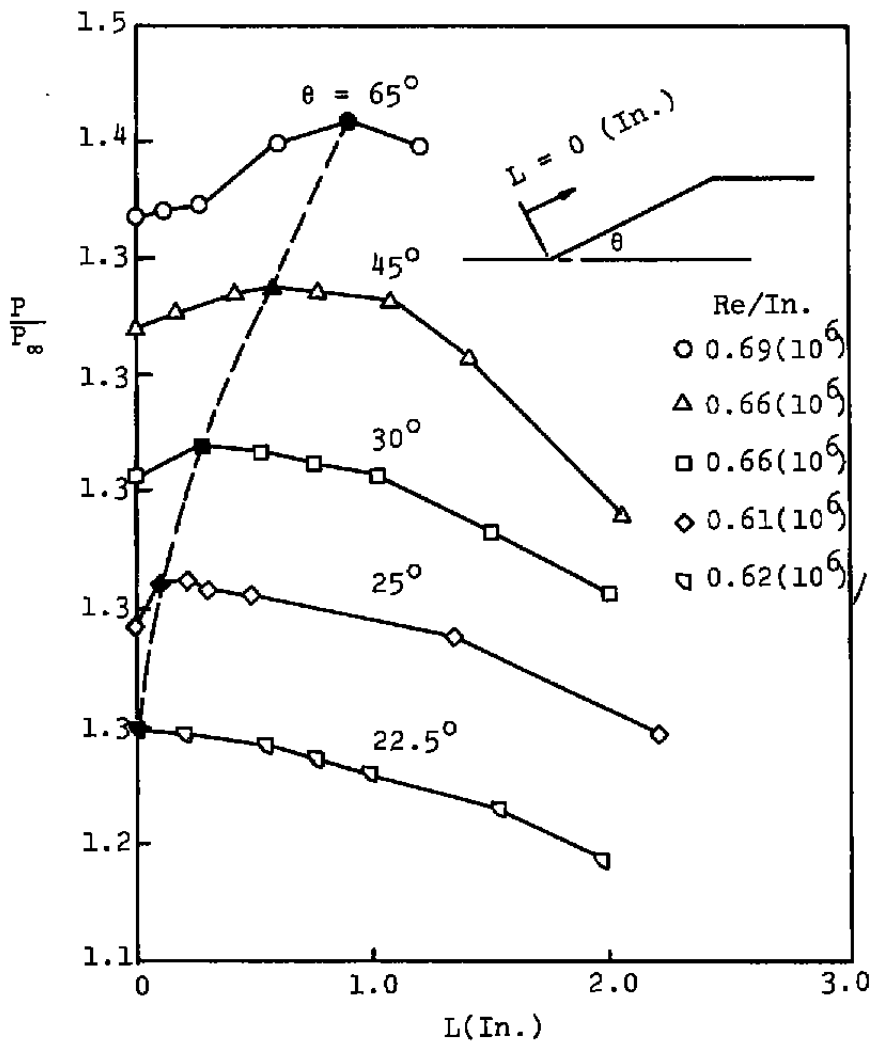


Figure 14b. Plots of Ramp Surface Pressures and Peak Pressure Trend as a Function of Ramp Angle.

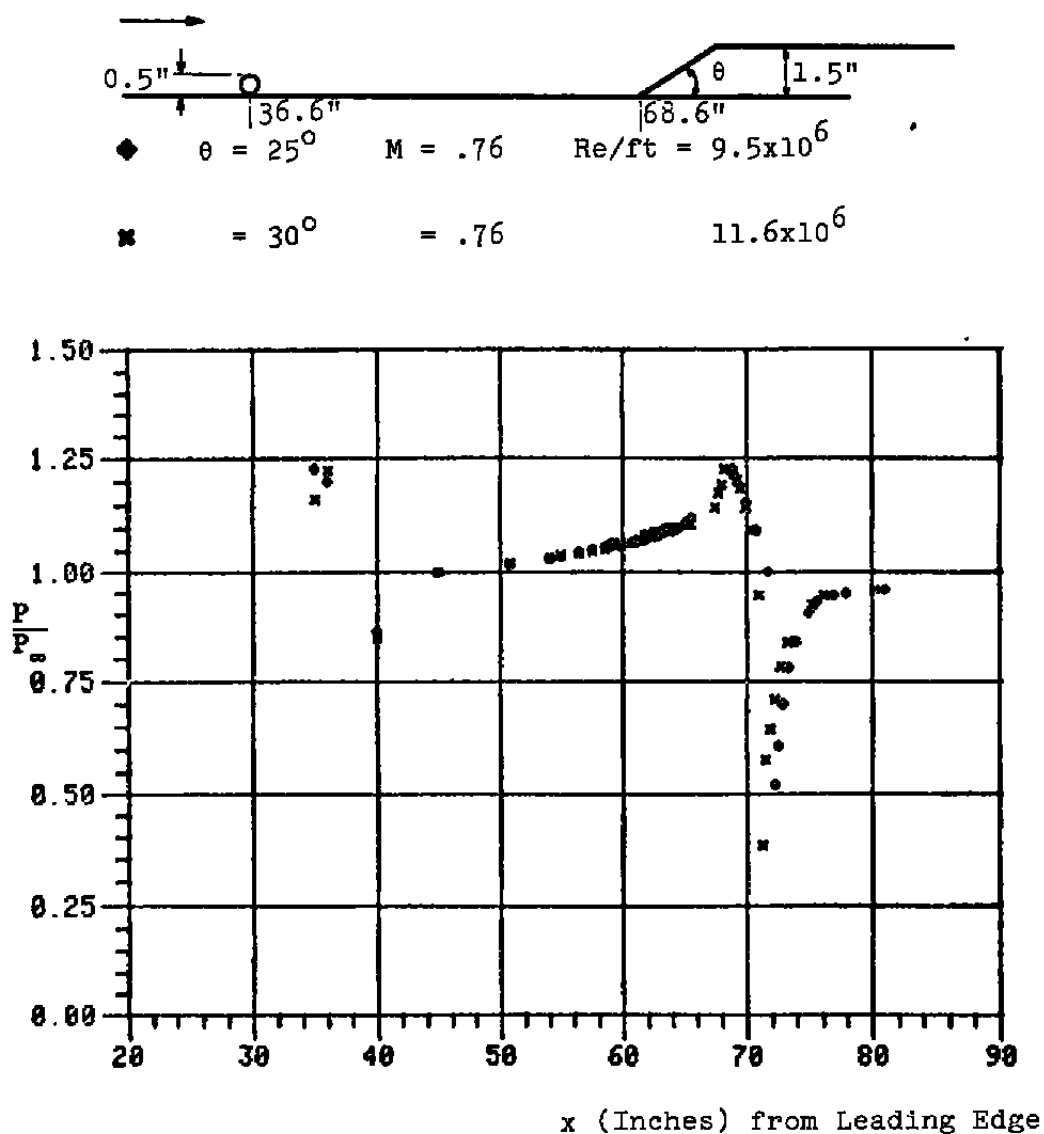


Figure 15. Effect of Upstream Small Cylindrical Disturbance on the Surface Pressure Distribution Over the Ramps of Different Angles.

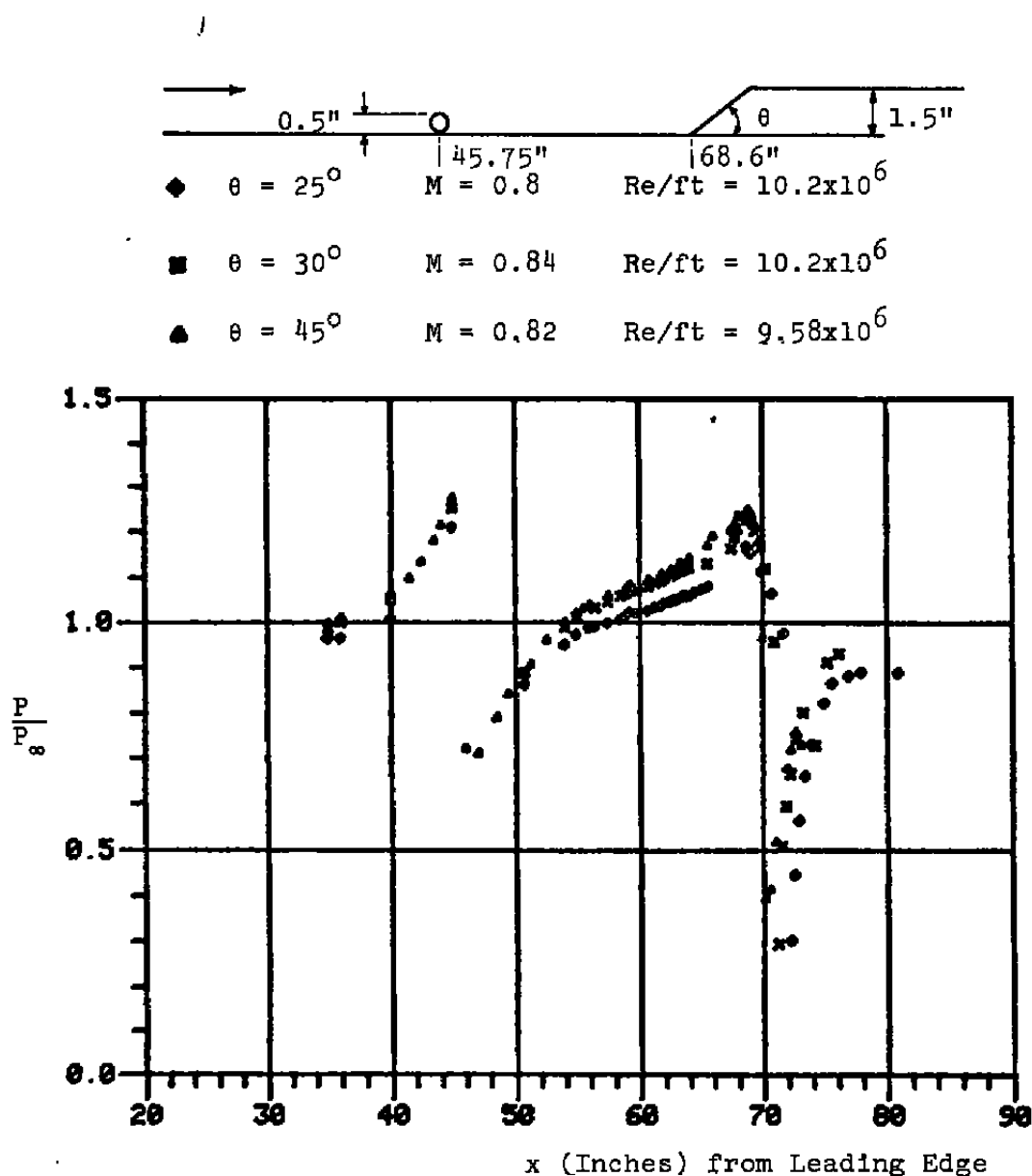


Figure 16. Effect of Upstream Small Cylindrical Disturbance on the Surface Pressure Distribution Over the Ramps of Different Angles.

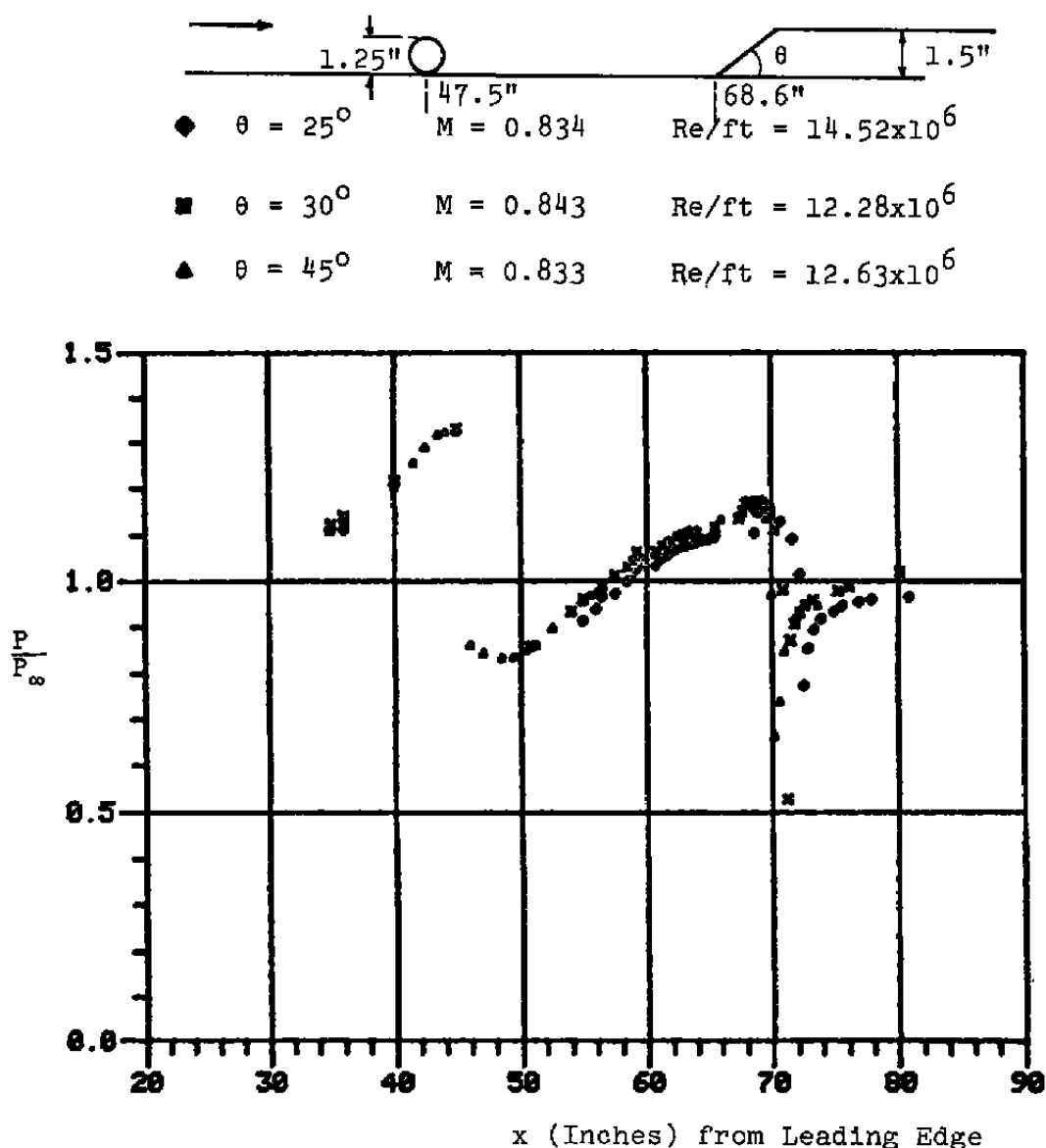


Figure 17. Effect of Large Cylindrical Upstream Disturbance on the Surface Pressure Distribution Over Ramps of Different Angles.

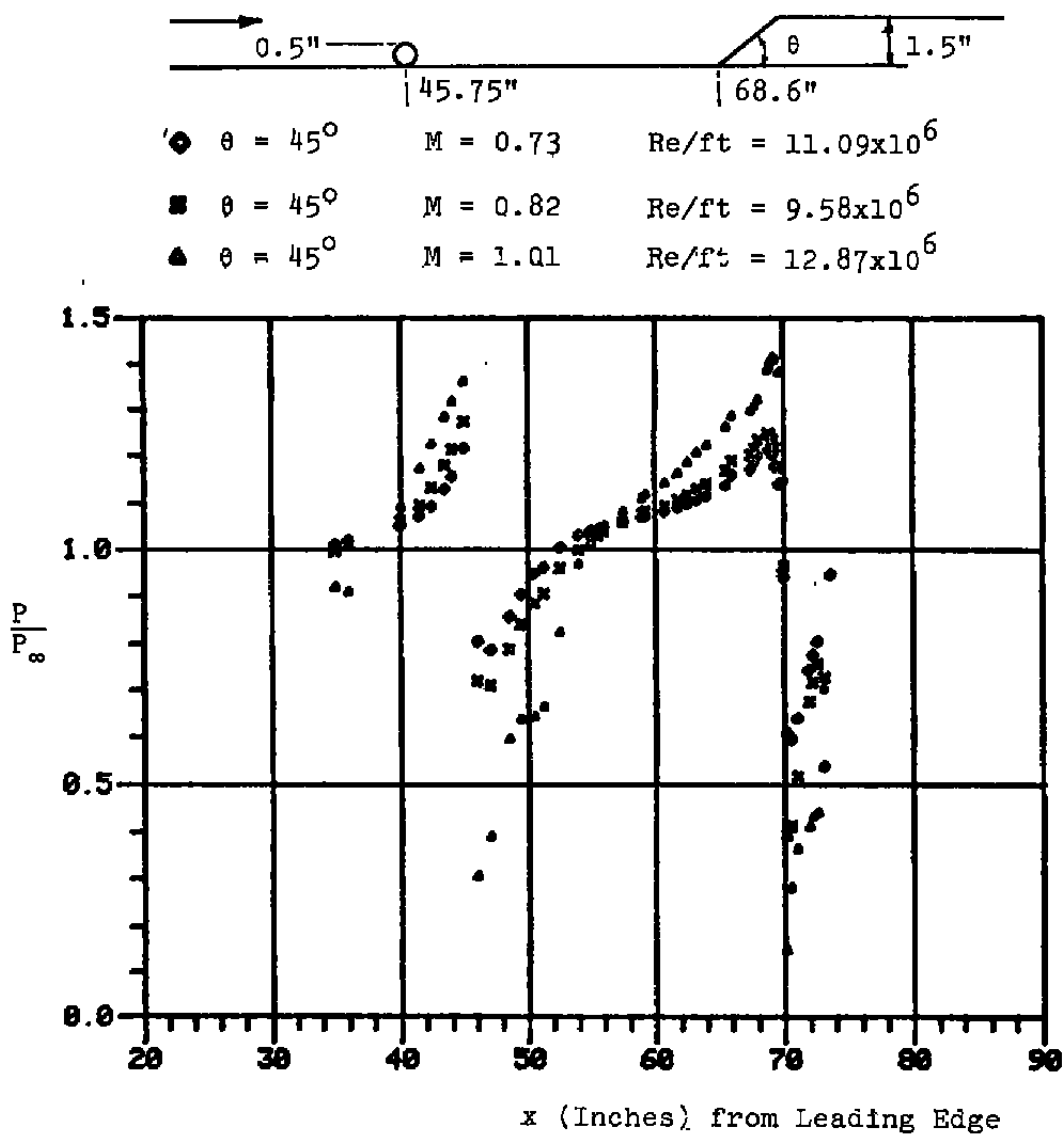


Figure 18. Effect of Mach Number on Disturbed Flow Over a 45° Ramp.

and produces a redistribution of energy in the shear layer downstream of the disturbance. That is, due to the presence of the cylindrical disturbance, the new shear layer has considerably less kinetic energy but higher turbulent shearing stresses. The high turbulent shearing stress resists (prevents) separation to a great extent. Therefore, as will be seen, the incipient separation angle for the disturbed flow increases.

Schubauer and Klebanoff (Ref. 16) gave a detailed physical explanation concerning the effects of turbulent shearing stresses and their relative importance with respect to viscous stresses on boundary layer characteristics. It is well known that viscous shearing stresses are so small that laminar flow can advance but a little distance beyond a pressure minimum. In contrast with this, turbulent shearing stresses can prevent separation entirely or delay it if the rate of increase of pressure is not too large. This emphasizes an important fact, namely, that when separation has not occurred, or has been delayed to distances well beyond the pressure minimum, as in the present experiment, viscous stresses play an insignificant role in the prevention or delay of separation. Turbulent shearing stresses also determine the magnitude of shearing stresses in the laminar sublayer by forcing a high rate of shear. This, in fact, gives boundary layer profiles the appearance of near slip flow at the surface. Thus, turbulent stresses dominate all parts of the boundary layer. Viscous effects in the laminar sublayer and elsewhere still play an important role in determining the existing state of the turbulence. However, in dealing with the effects of turbulence, and not with the origin of turbulence, effects of viscosity can be neglected.

It is easy to see qualitatively on physical grounds how the shearing stress must be distributed across the boundary layer. The shearing stress is always in such a direction that fluid layers farther out pull on layers further in. When the pressure is either constant or falling, all pull is ultimately exerted on the surface. Therefore, the shearing stress must be at least as high at the surface as it is elsewhere, and it would be expected to be a maximum there, as it must fall to zero outside the boundary layer. When the pressure is rising, part of the pull must be exerted on the fluid near the region of higher pressure. In other words, the fluid in such layers must be pulled upon harder than it pulls upon the layer nearer the surface. This means that the shearing stress must have a maximum away from the surface in regions of adverse pressure gradients. Figure 19 shows some representative shear stress distributions observed. It is seen that the maximum shear stress develops

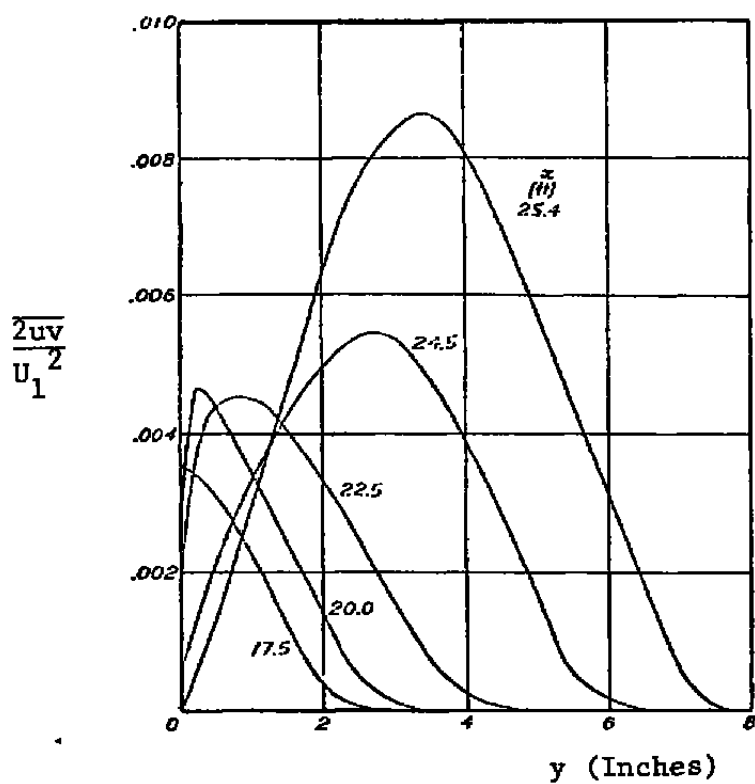


Figure 19. Distribution of Coefficient of Shearing Stress Across Boundary Layer on a Flat Plate Under Adverse Pressure Gradient Causing Separation (Reference 16).

first near the surface and moves progressively outward. The region between the surface and the position of maximum stress is receiving energy from the region beyond the maximum, the rate per unit volume at each point being $u \partial \tau / \partial y$. Thus, the fall in the shearing stress toward the surface, producing a positive slope, is evidence that the shearing stress is acting to prevent separation. It is clear then that a stress falling to zero at the surface, as for example, the curve at $X = 25.4$ feet (Fig. 19), is not the only cause of separation. It is rather an indication that the velocity gradient is vanishing at the surface. This means that the velocity in the vicinity of the surface is vanishing and that a condition is developing in which no energy can be received. When this condition is fulfilled the fluid can move no further and separation has occurred. Chu and Young found similar results (Ref. 17) as in Ref. 16. In the experiments by Chu and Young it was observed that the shear stress does not go to zero at the outer edge of the boundary layer and the low frequency unsteadiness of the separated flow region was given as the reason for the above phenomena.

Turbulent shearing stresses relax with length or time downstream of the disturbance region. This relaxation, also called the rehabilitation process of flow after a disturbance, is extremely complicated and is still an unresolved problem in fluid dynamics today. Detailed turbulence measurements in such regions are required to gain more insight about this process.

Figure 20 presents the wall static pressure distribution plot for flow over a 30 degree compression corner with a 1.25-inch diameter cylinder located at 32 and 23 inches upstream. Although the flow Mach number and Reynolds number are almost the same, the static pressure distributions downstream of the disturbance are significantly different, which shows the difference in the relaxation length on the flow downstream of the same disturbance. In Fig. 20, for the longer relaxation distance, the peak pressure on the ramp is much higher which indicates that the partial recovery of velocity profile after the disturbance depends strongly on the relaxation distance. The subsequent flow recompression over the top of the ramp is slower in this case. Similar conclusions can be drawn from Fig. 21, where wall static pressure for flow over a 1.25-inch diameter cylindrical disturbance at three locations upstream of a 25-degree compression ramp is plotted.

To study the effect of the disturbance size on the flow, two cylinders of diameters 0.5 inch and 1.25 inch were placed at the same upstream location in similar flow

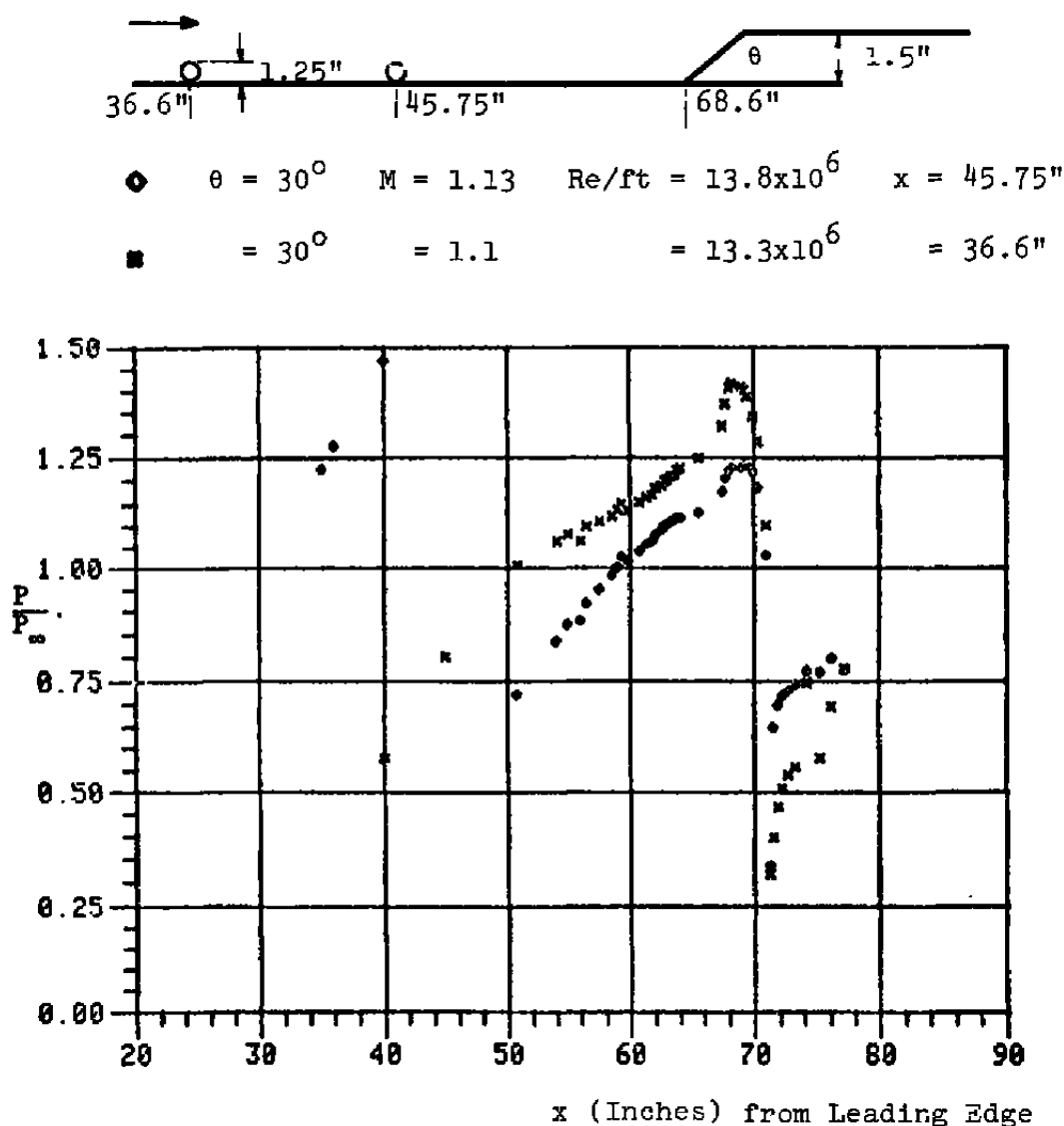


Figure 20. Effect of Relaxation Distance Downstream of a Large Cylindrical Disturbance on the Surface Pressure Distribution Over a Ramp of 30° Angle.

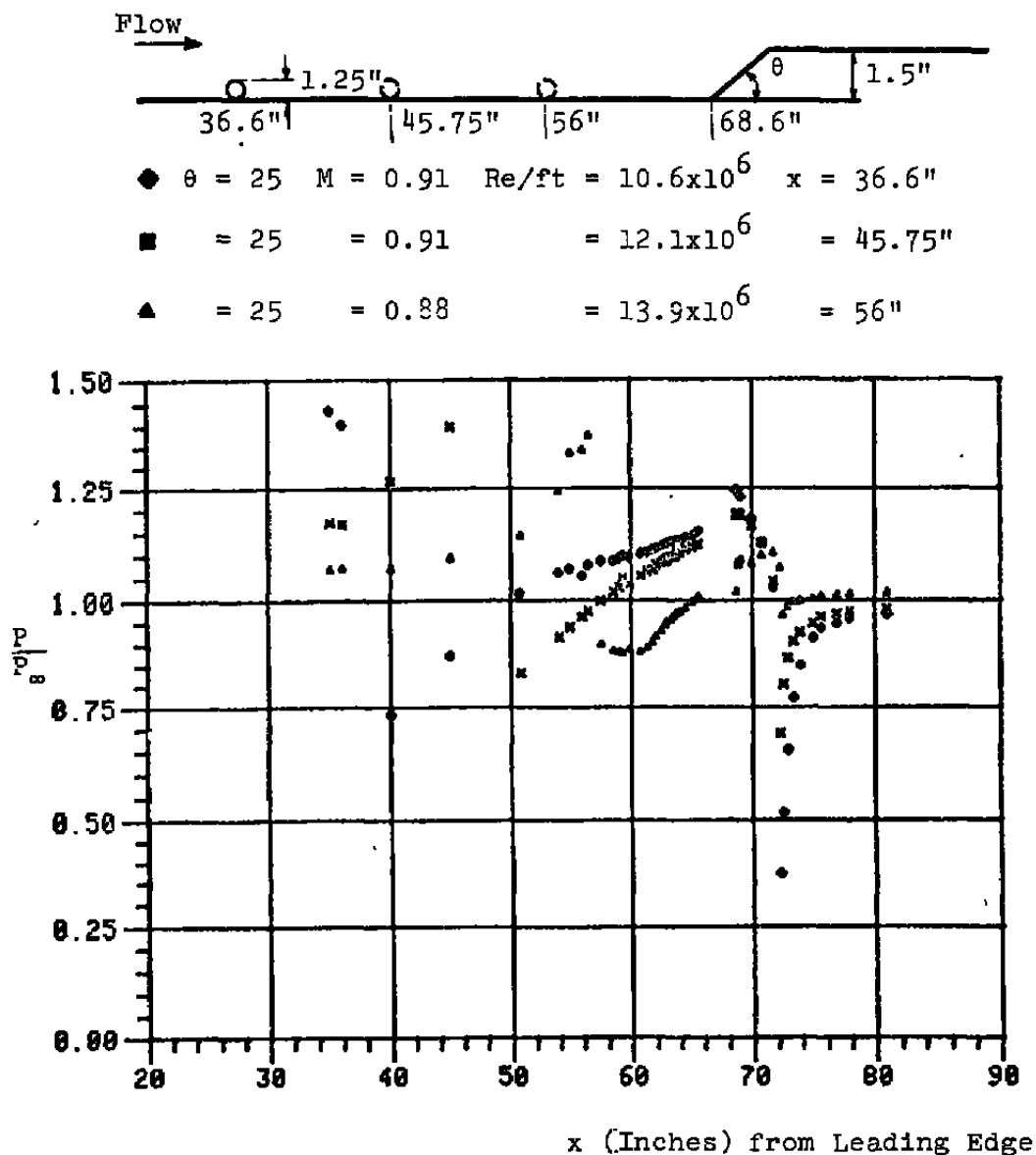


Figure 21. Effect of Relaxation Distance Downstream of a Large Cylindrical Disturbance on the Surface Pressure Distribution Over a Ramp of 25° Angle.

conditions. The larger cylinder obviously produced a larger disturbance to the flow field (Fig. 22). In this case, the rehabilitation distance is the same. However, since the larger cylinder caused a stronger distortion to the flow and hence to the velocity profile, a lower peak pressure was reached on the ramp. But the more disturbed flow field reached the free stream static pressure in a shorter distance from the top of the ramp.

Another type of upstream disturbance generator that was studied consisted of rearward-facing steps of various height to undisturbed boundary-layer thickness ratios. The backward-facing steps also introduce a significant disturbance into the flow field. Typical surface static pressure distributions for nearly constant Mach number and Reynolds number flow over ramps of different angles with a 1.25-inch backward-facing step at 34.6 inches upstream of the ramp compression corner are given in Fig. 23. The extent of the disturbance generated by a rearward-facing step is comparatively smaller than the disturbance produced by the cylindrical disturbance of equal height under similar flow conditions. In particular, the peak pressure on the ramp is reduced more by the cylinder than by the rearward-facing step. Figure 24 shows this observation. It should also be mentioned that the step was 2.6 inches further upstream of the ramp than the cylinder, and therefore in this case the flow had a longer distance to relax from the rearward-facing upstream disturbance. The effect of length on the relaxation process for a rearward-facing step disturbance is shown in Fig. 25. Similar to the cylindrical disturbance, the distance plays an important role in the relaxation process.

In flow over ramp compression corners, the critical angle at which a known flow will start to separate is called the incipient separation angle. For laminar flows, the incipient separation angle is smaller than for turbulent flow of similar free stream conditions. This is because viscous shearing stresses in the laminar flow close to the wall are small. In contrast, turbulent shearing stresses are large and can prevent separation entirely or delay it if the rate of increase of pressure is not too large. The Reynolds number effect on incipient separation angle has been studied by many investigators; most of them found strong Reynolds number influence on incipient separation angle. Most of these studies have been performed at subsonic or supersonic Mach numbers. However, in the present study no Reynolds number influence was found in the range of $10^5 < Re_{\delta_0} < 10^6$, where the Reynolds number is based on the undisturbed boundary layer thickness at the ramp location. This agrees with the recent supersonic results

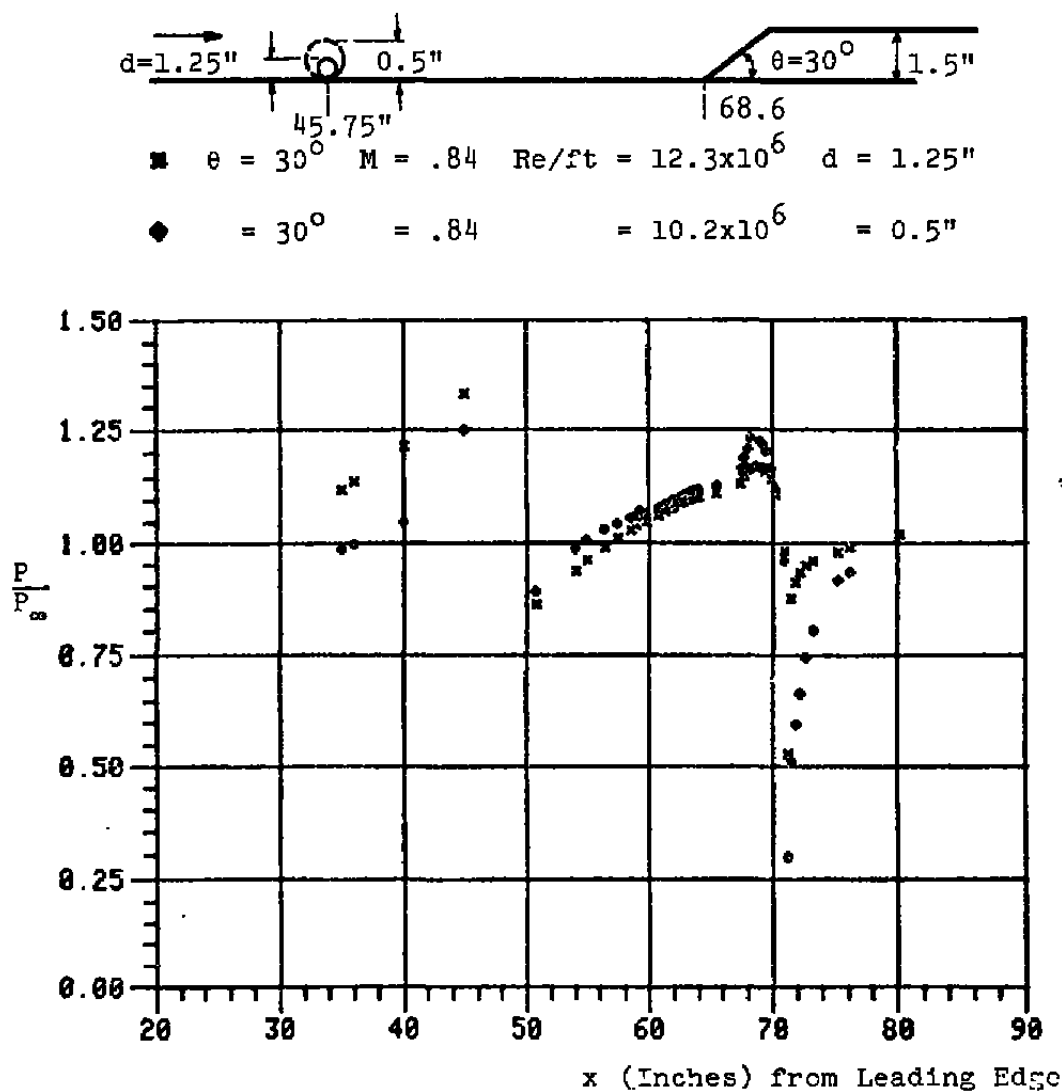


Figure 22. Comparison of Disturbance Size Effect on the Flow Over a 30° Ramp.

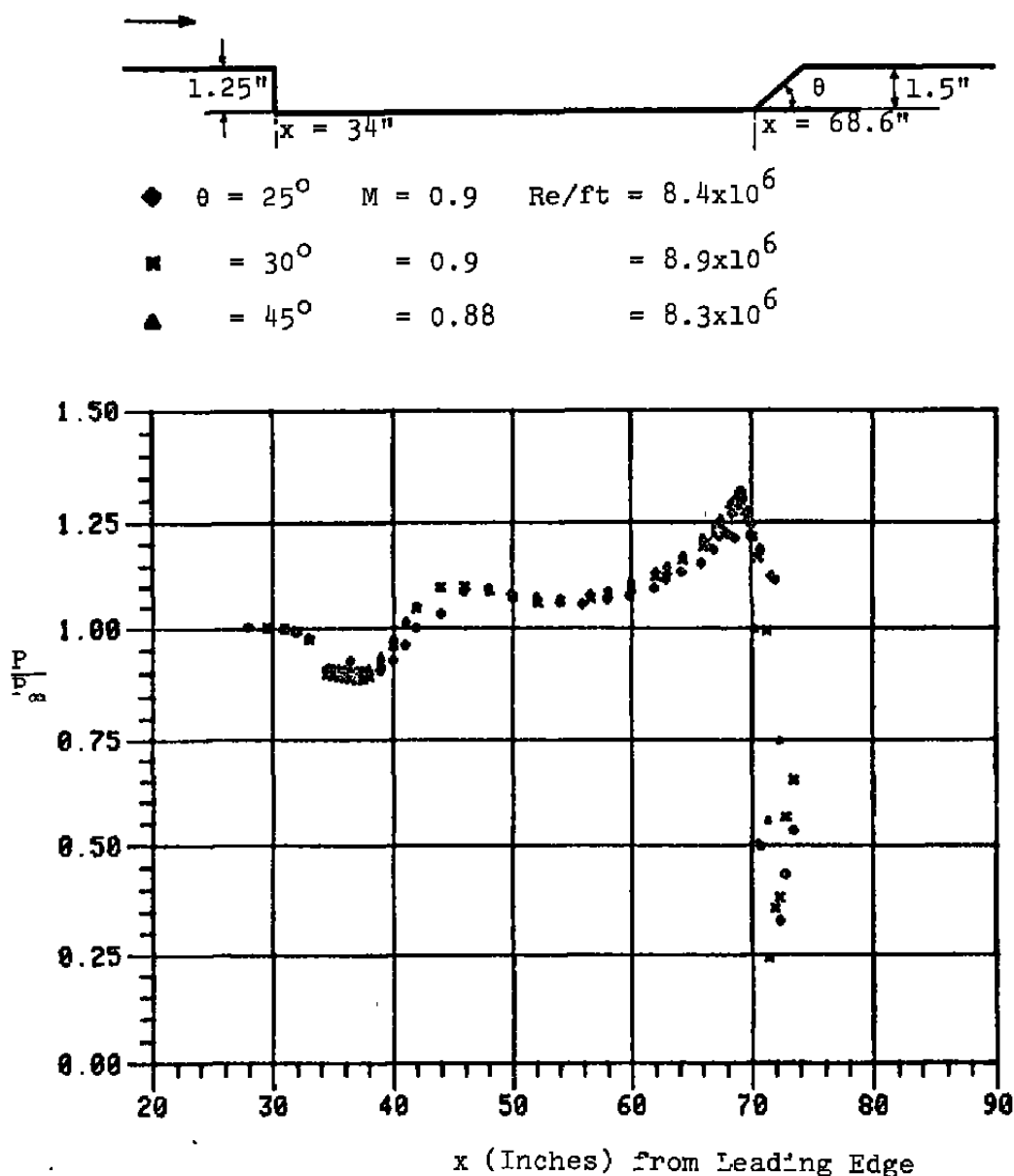


Figure 23. Effect of Backward Facing Step Disturbance on the Surface Pressure Distribution of Flow Over Ramps of Different Angles.

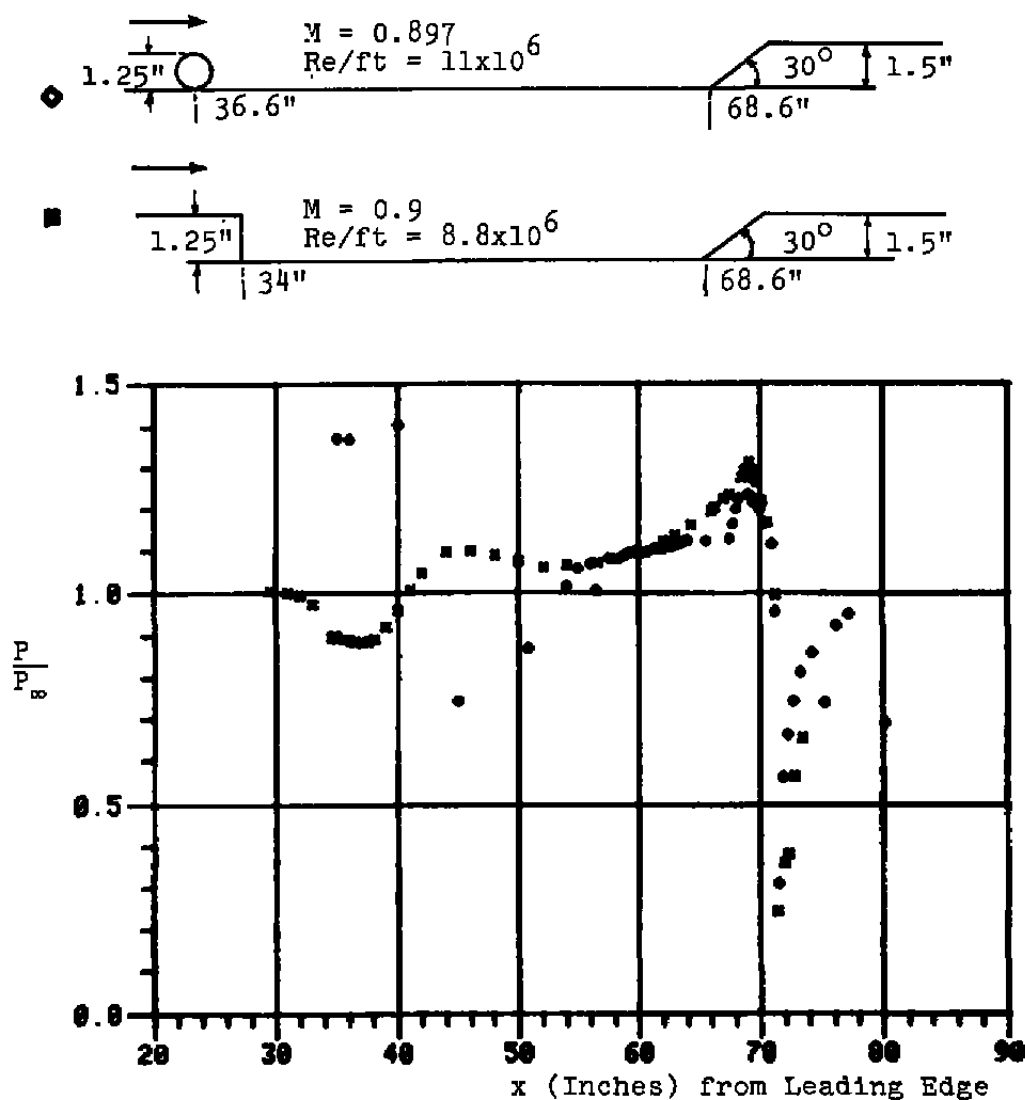
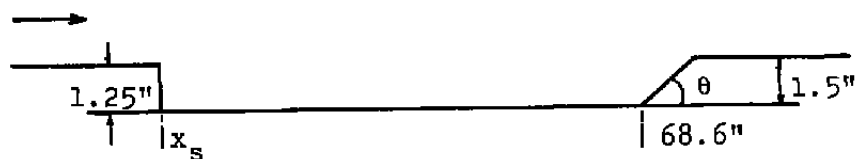


Figure 24. Comparison of Different Disturbances Effect on the Surface Pressure Distribution Over Ramp of 30° Angle.



- ◆ $\theta = 25^\circ$ $M = 0.90$ $Re/ft = 8.1 \times 10^6$ $x_s = 34"$
 x $\theta = 25^\circ$ $M = 0.89$ $Re/ft = 7.9 \times 10^6$ $x_s = 45.75"$

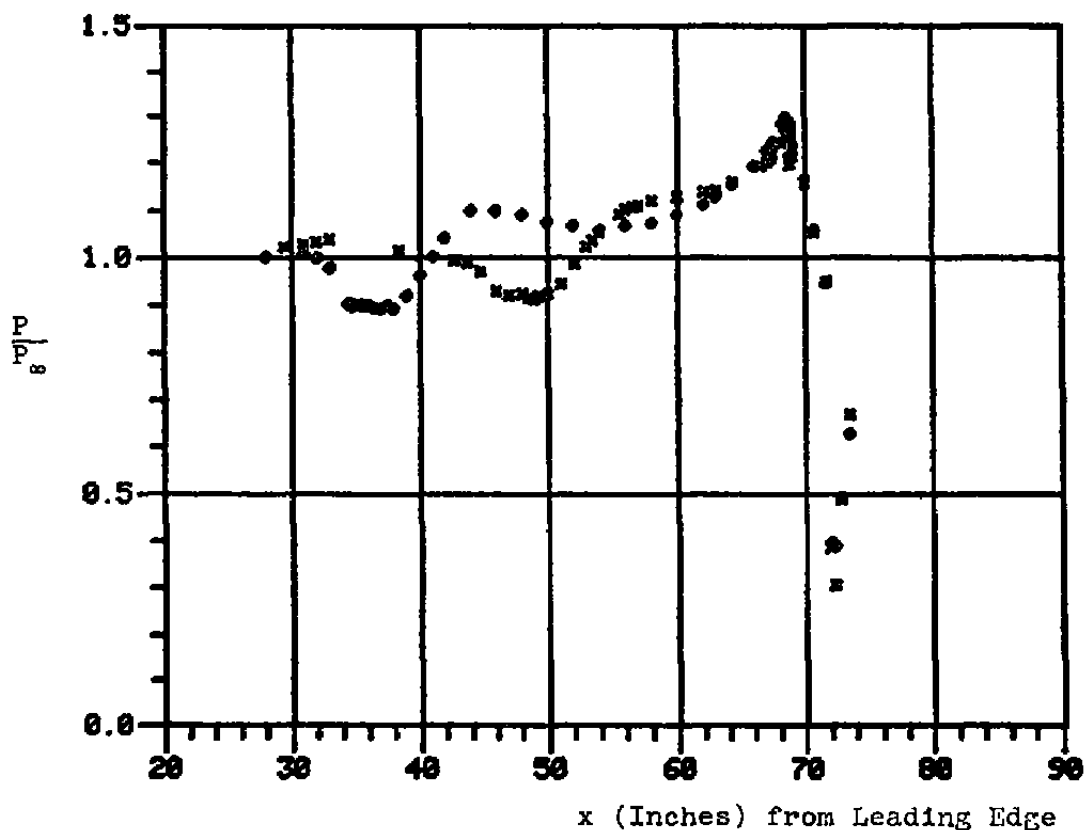


Figure 25. Effect of Relaxation Distance Downstream of a Backward Facing Step on the Surface Pressure Distribution Over a 25° Ramp.

of Settles (Ref. 18) and Inger (Ref. 19), Fig. 26. In some of the previous investigations where a Reynolds number effect was observed, the turbulent boundary layer was artificially produced at low Reynolds numbers. Experiments in the present investigation showed an increase in the incipient separation angle when an upstream disturbance was present, Fig. 27. The turbulent boundary layer was always naturally obtained in the present experiments.

As far as the flow on the ramp is concerned, the peak pressure reached on the ramp reveals valuable information about the flow energy and history upstream of the step. Due to difficulty in accurately determining the separation pressure and the fact that the separation and maximum pressure are very nearly equal in this range of free stream Mach numbers, the peak pressure has been considered for possible correlations with free stream parameters. The total pressure has been selected for the normalization parameter, since it represents the total energy of the flow. The P_m/P_t variation for different ramp angles with change of free stream Mach number over a large range of Reynolds numbers is plotted in Fig. 28. There seems to exist a linear trend from this plot, neglecting the scatter of data around $M_\infty \sim 1.0$. This scatter in the data is suspected to be due to interference of the traversing pitot probe which was ahead of the ramp and other sources which could not be isolated. The forward-facing step data points corresponding to $\theta = 90^\circ$ show a similar trend, as seen in this figure. From Fig. 28 the equation for this line is

$$\frac{P_m}{P_t} = -0.3 M_\infty + 1.08 \quad (8)$$

If the approaching flow is brought to rest on the ramp isentropically then the pressure will be equal to P_t . However, the present result indicates that dissipation occurs during the deceleration process and the amount of dissipation increases with Mach number.

The Reynolds number dependency of the peak pressure can be found by combining Equation (8) with the Reynolds number equation from Chapter 2.0. By eliminating P_t from the two equations we obtain:

$$Re/ft = \frac{1.7784 \times 10^9}{(T_o + 460^\circ)^{1.315} (1 + 0.2 M_\infty^2)^{2.185} (1.08 - 0.3 M_\infty)} P_m \quad (9)$$

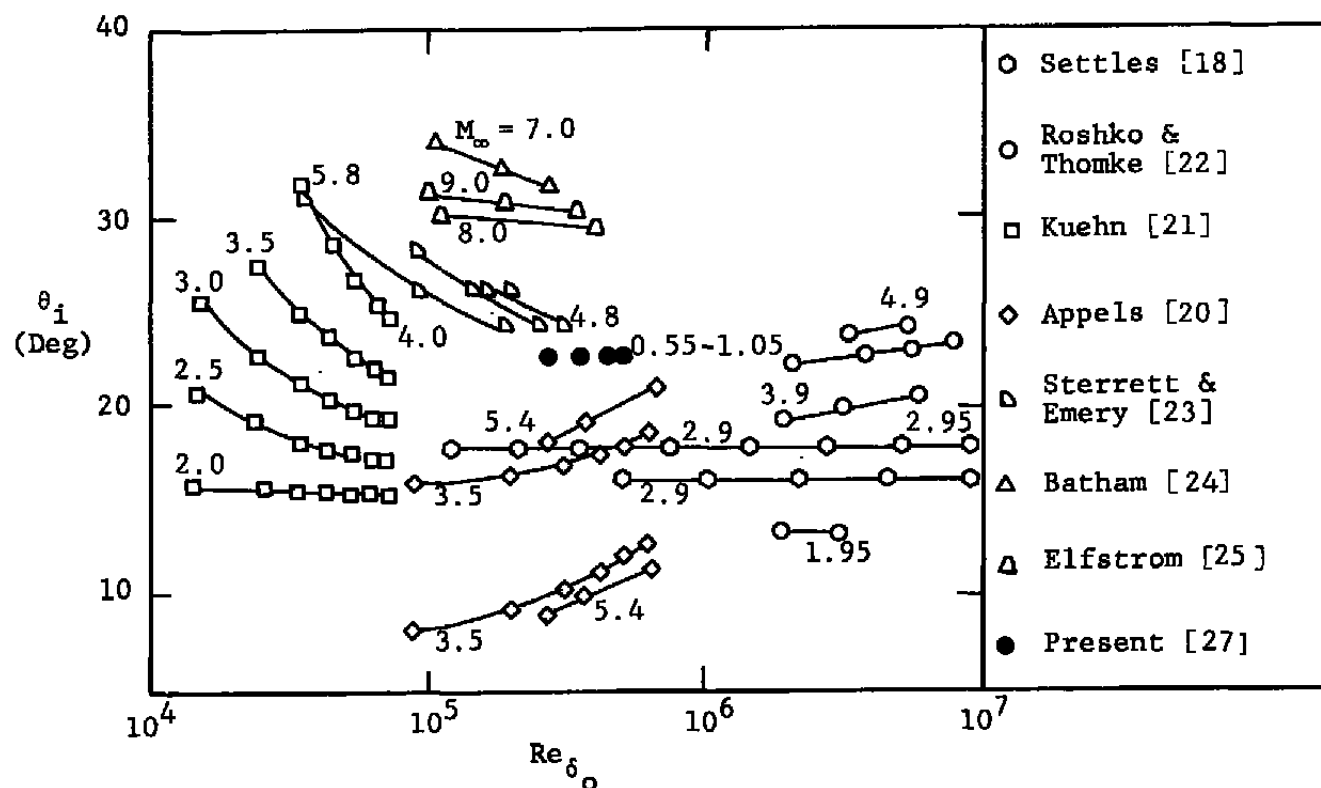


Figure 26. Incipient Separation Angles for Two-Dimensional Ramp Compression Corner. Adapted from Reference [20].

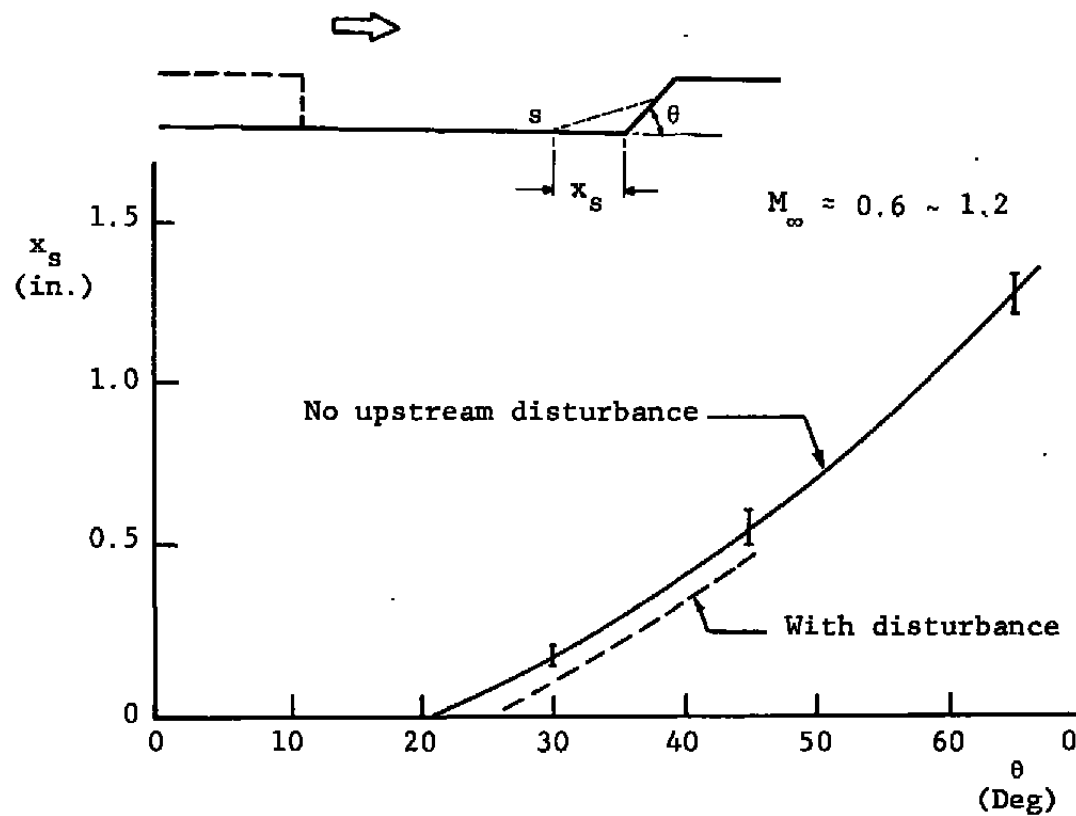


Figure 27. Separation Length as a Function of the Ramp Angle.

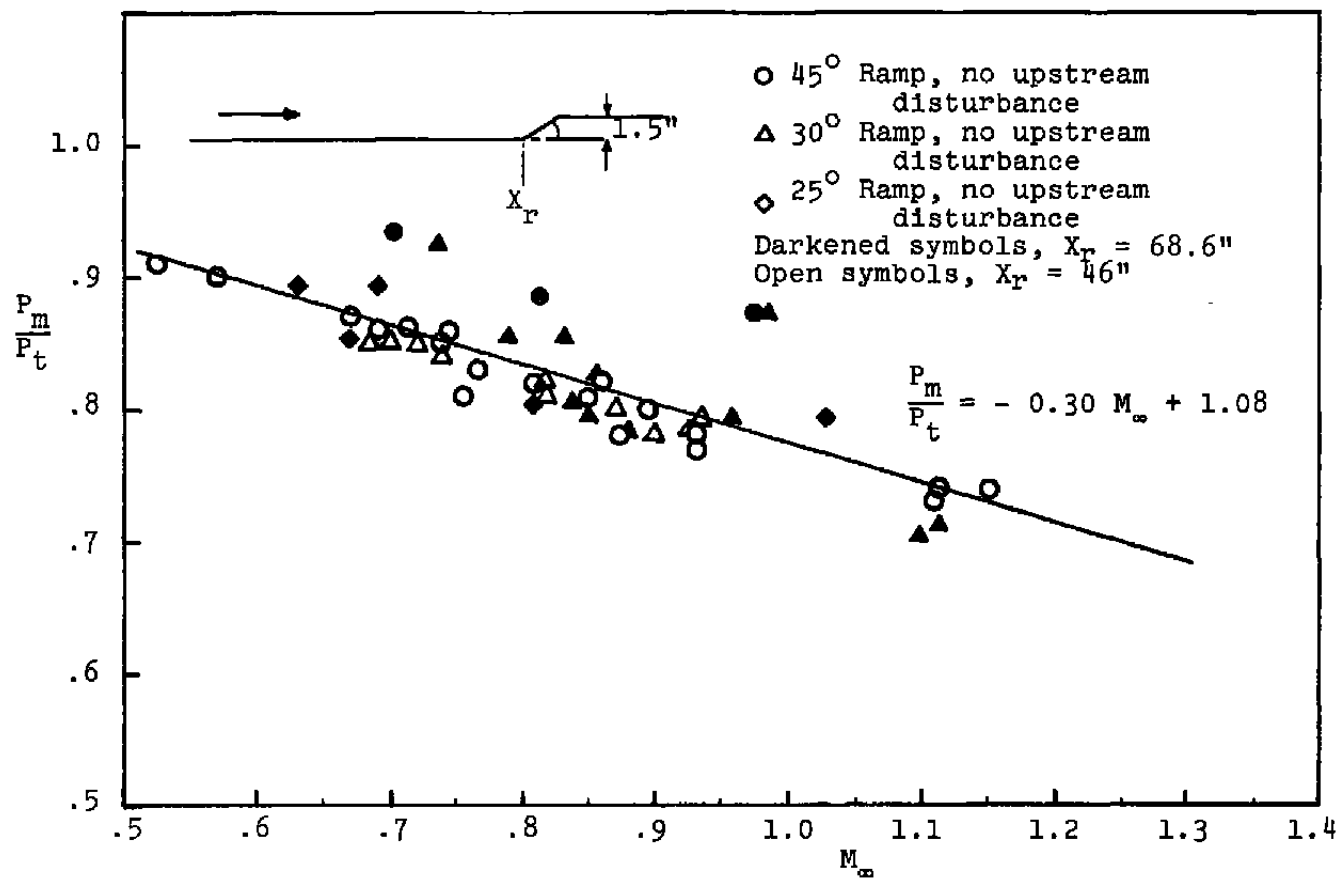


Figure 28. Variations of Peak Pressure Against Free Stream Mach Number.

This equation cannot be put into a simple explicit relationship between unit Reynolds number, Mach number, and peak pressure. However, it can be used to predict an unknown peak pressure for known free-stream conditions.

In Fig. 29 the same parameters are plotted for the ramp-compression-corner with a 0.5-inch diameter cylinder placed at different distances upstream of the ramp. The same plot for a 1.25-inch diameter cylinder is shown in Fig. 30. Surprisingly, all of these plots show a linear trend over the range of Mach numbers, Reynolds numbers, and relative upstream location of the disturbance generators.

It is of interest to compare the effect of disturbances of different nature, say a rearward-facing step, with that of the cylinders. Figure 31 shows the plot of P_m/P_t versus Mach number for flow over 1.25-inch rearward-facing steps 34.6 and 22.85 inches upstream of ramps of different angles. The trend is linear again, and it is clear that the presence of the step has not produced as strong an effect when compared to the cylinder. The slope of the curve P_m/P_t versus M_∞ can be used as a measure of the strength of the upstream disturbance upon the flow over the ramp. Over the range of upstream distances examined, namely about 30 to 45 boundary layer thicknesses, the slope was characteristic of the specific disturbance generator and can be used to characterize that generator. The different generators are compared in Fig. 31b. From this figure it can be seen that the rearward-facing step produces the least influence upon the flow approaching the ramp while the effect of a cylinder increases with the diameter of the cylinder.

The above comparison is only valid if the disturbance is not close enough to the ramp to have a direct interaction with the flow over the ramp. This effect is shown in Fig. 32 for a rearward-facing step placed close to the ramp. With the rearward-facing step 6.35 inches upstream of the ramp the separated flow reattaches on the ramp and the flow between the two is no longer characteristic solely of the effect of the upstream disturbance upon the flow approaching the ramp.

Figure 33 shows the plot of P_m/P_t against the nondimensionalized relaxing length scale L/h_d . From this plot again the peculiar characteristics of a rearward-facing step upstream disturbance can be seen. The data for the rearward-facing step are located at $L/h_d = 27.68$ and are clearly off the trend of the cylindrical type disturbances. It will fit in this categorization if a larger equivalent L/h_d (which means smaller h_d) is considered for the rearward-facing step data.

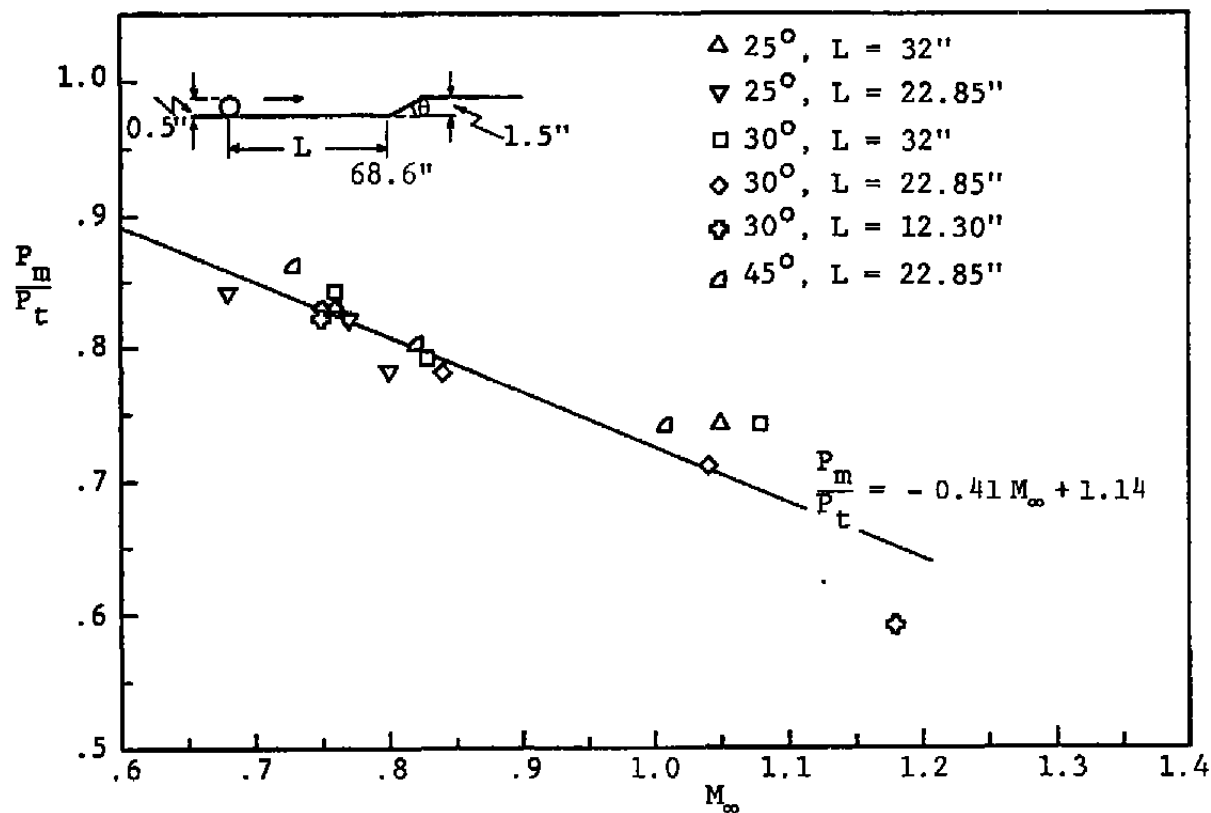


Figure 29. Variation Peak Pressure Over the Ramp Compression Corner with Upstream Disturbance Against Free Stream Mach Number.

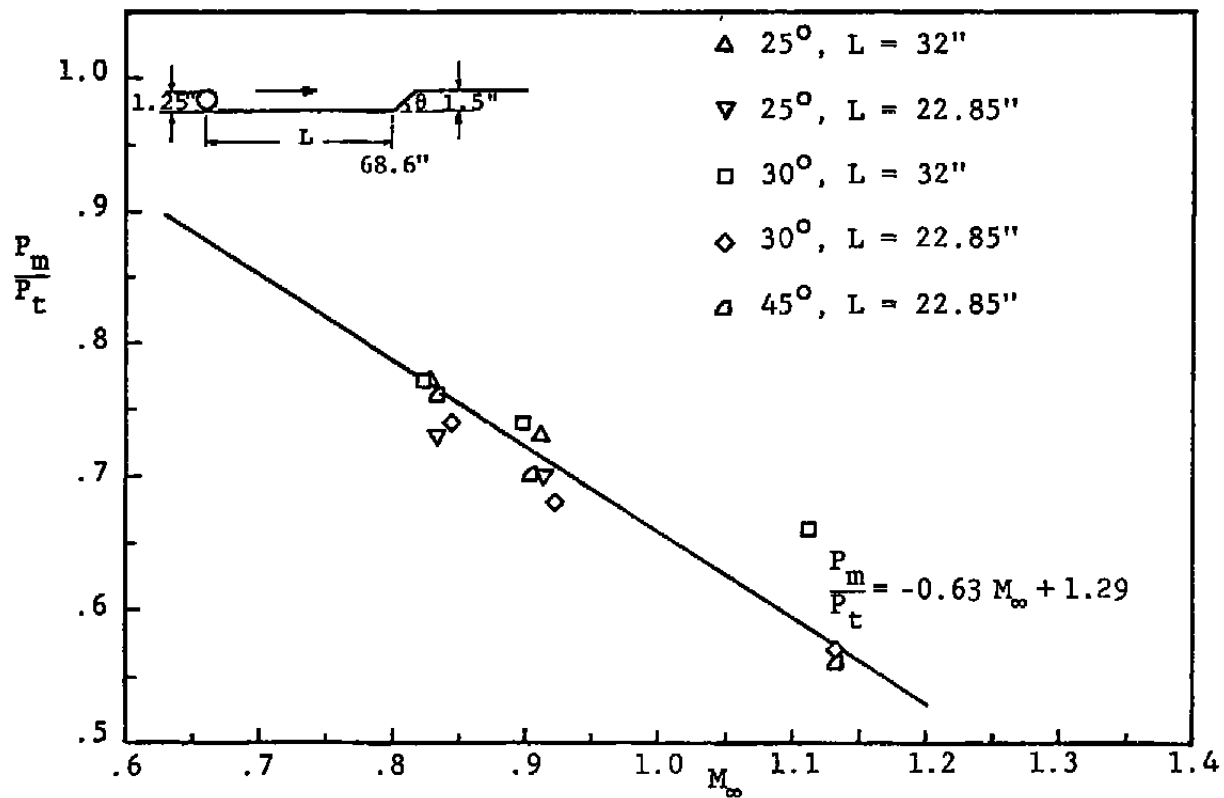


Figure 30. Variation of Peak Pressure Over the Ramp Compression Corner with Upstream Disturbance Against Free Stream Mach Number.

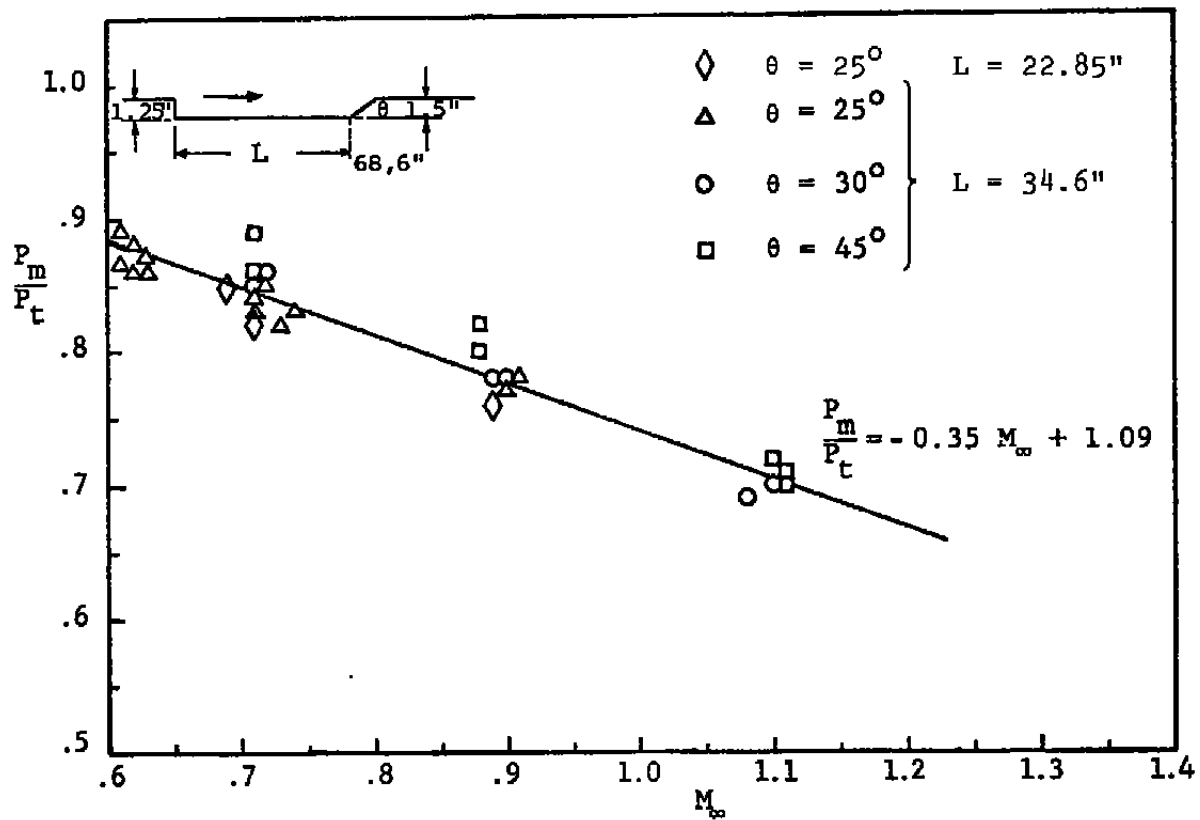


Figure 31a. Variation of Peak Pressure on the Ramp Compression Corner with a Backward-Facing Step Downstream Disturbance Against Free Stream Mach Number.

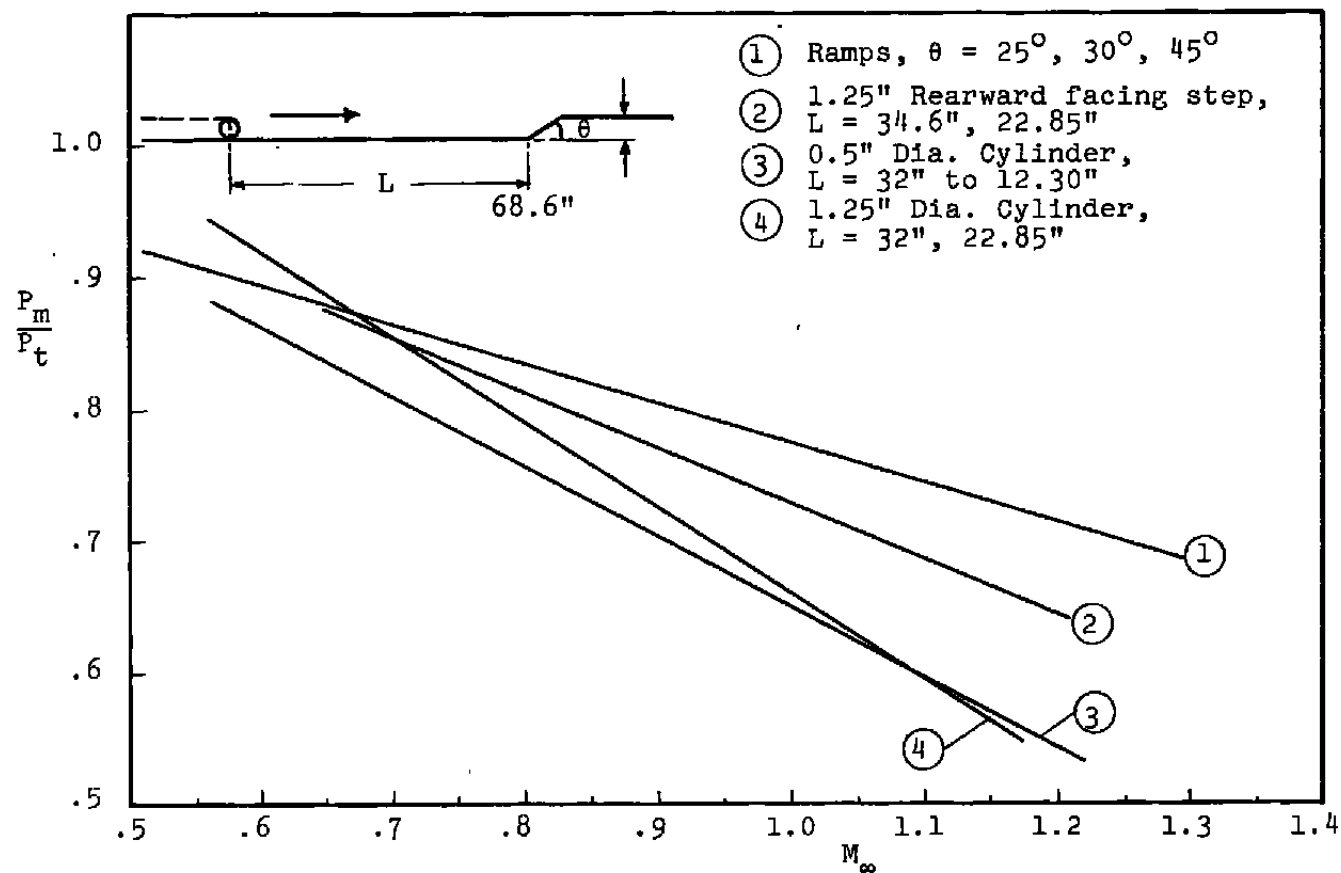


Figure 31b. Comparison of Effect of Various Upstream Disturbance Generators Upon Flow Over Ramp-Compression-Corner.

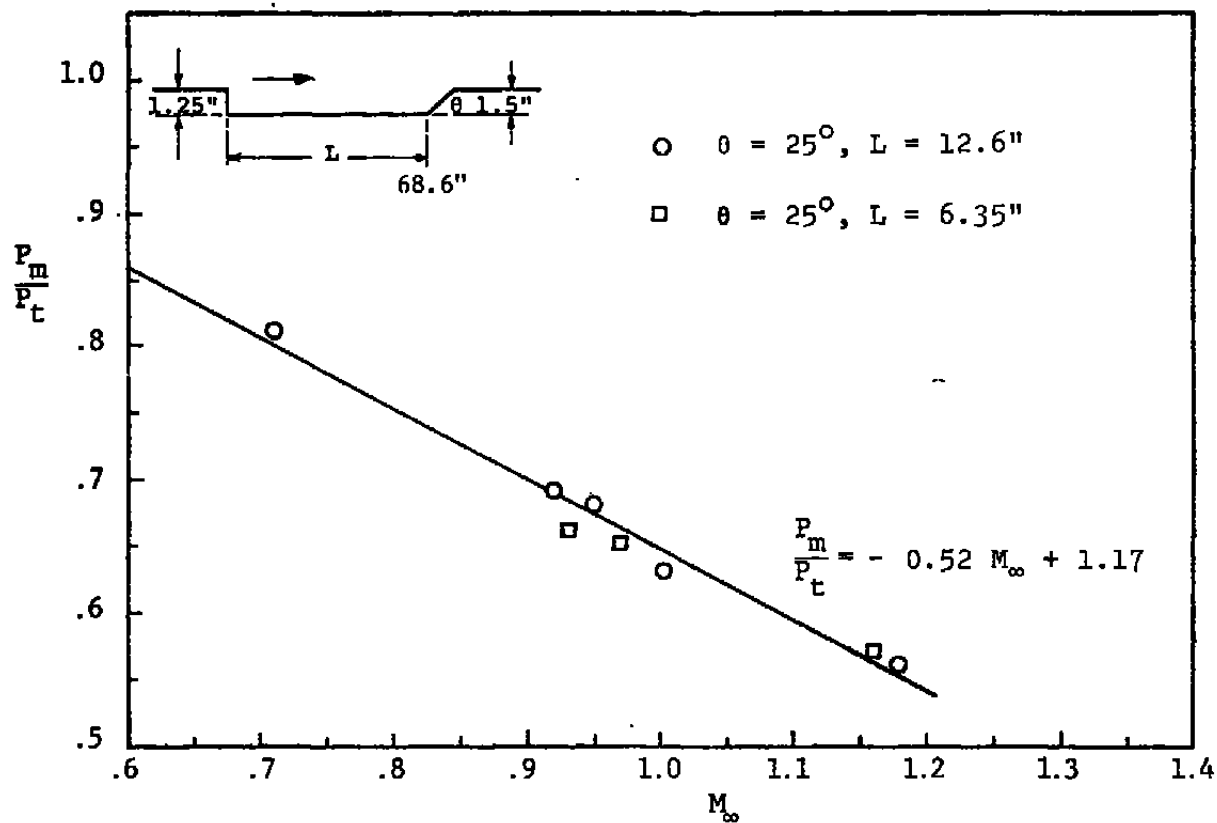


Figure 32. Peak Pressure Variations on the Ramp Compression Corner a Short Distance Downstream of a Backward-Facing Step Against Free Stream Mach Number.

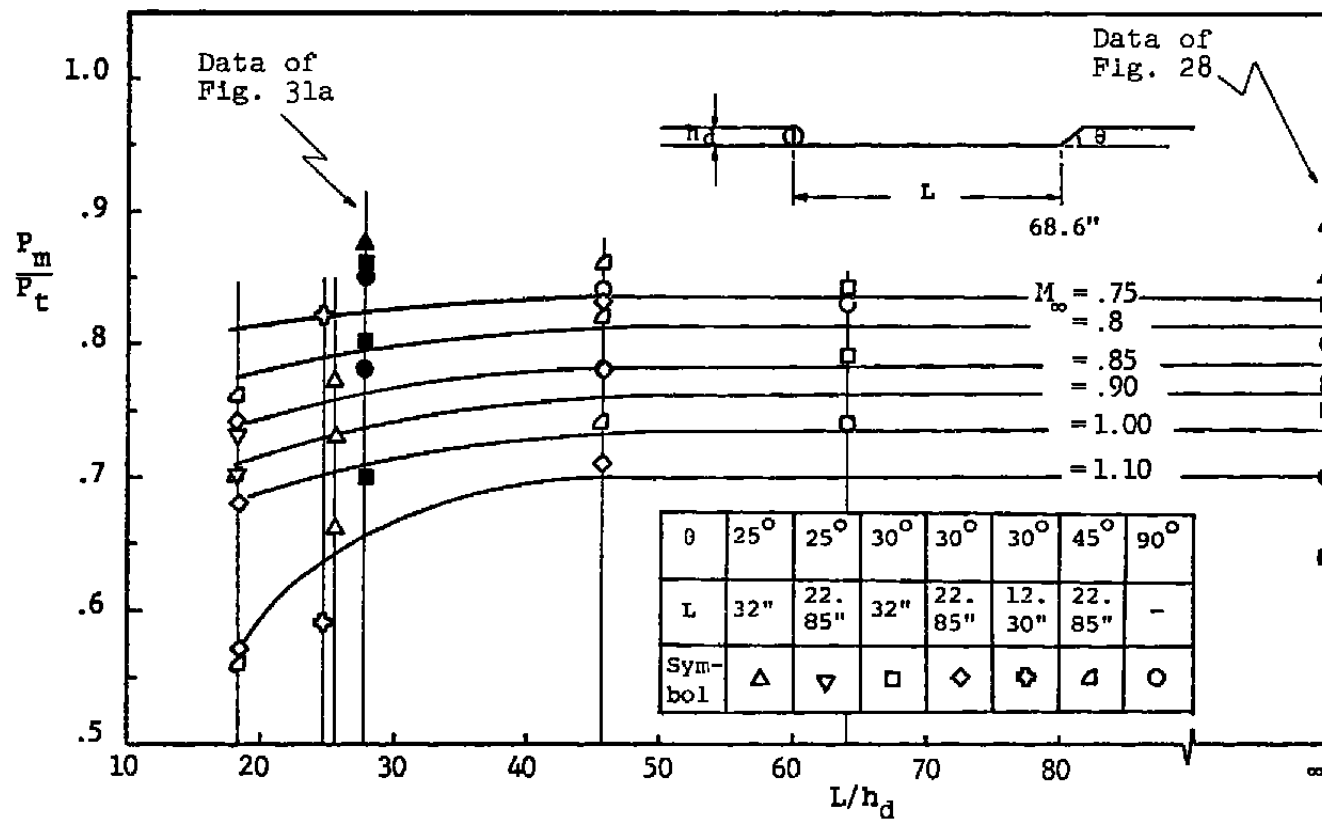


Figure 33. Variation of Peak Pressure Against Nondimensionalized Relaxation Distance.

The presence of upstream disturbances causes a strong mixing process which feeds energy from the free stream into the shear layer. The energy exchanged between the mean flow and the shear layer is governed by the dynamics of the large turbulent eddies. Large eddies contribute most to the turbulence production. The viscous dissipation of turbulent energy, on the other hand, occurs mainly at micro scales, comparable to the Kolmogorov micro scale (Ref. 28). This implies that the internal dynamics of the turbulence must transfer energy from large scale eddies to small scale eddies. Therefore the energy distribution after a disturbance will be completely different. As a result of the disturbance energy is being added to the large scales of the turbulent motion and time (or downstream distance) is required to redistribute the energy with the smaller scales and hence allow the turbulence to return to "equilibrium." Therefore, before equilibrium is reached downstream of the disturbance, the mixing processes associated with the larger eddy motion energizes the turbulent boundary layer and gives the boundary layer the ability to stay attached further in a region of an adverse pressure gradient, where normally the flow would have separated.

The strength of a disturbance and its effect on the relaxation process downstream depends on parameters like M_∞ , Re , δ , δ^* , θ , and the disturbance strength. We may define the strength of a disturbance as the ratio of pressure difference across the disturbance to the upstream undisturbed pressure, $(P_{max} - P_{min})/P_\infty$. This parameter is plotted against the free stream Mach number for cylindrical disturbances of different sizes located upstream of the ramps in Fig. 34. As the free stream Mach number increases the disturbance strength increases almost linearly. The scatter of the points in this figure is possibly due to the fact that no effort was made to keep the boundary layer parameters constant for the various measurements, nor were boundary layer parameters included in the definition of the disturbance strength parameter. An additional parameter that should be included in a complete definition of the disturbance strength is the relative size of the disturbance compared to the undisturbed boundary layer thickness, h_d/δ_0 . Also, the disturbance location is important, L/h_d .

The downstream effect of a disturbance depends on the disturbance strength and the distance between the disturbance and the point of interest. Along this distance the disturbed flow relaxes and the flow has a tendency to return to an equilibrium state. The history of the flow along a relaxing distance has been studied previously. However no theory is capable of describing the relaxation process. Chen (Ref. 26) observed that there is a critical length for

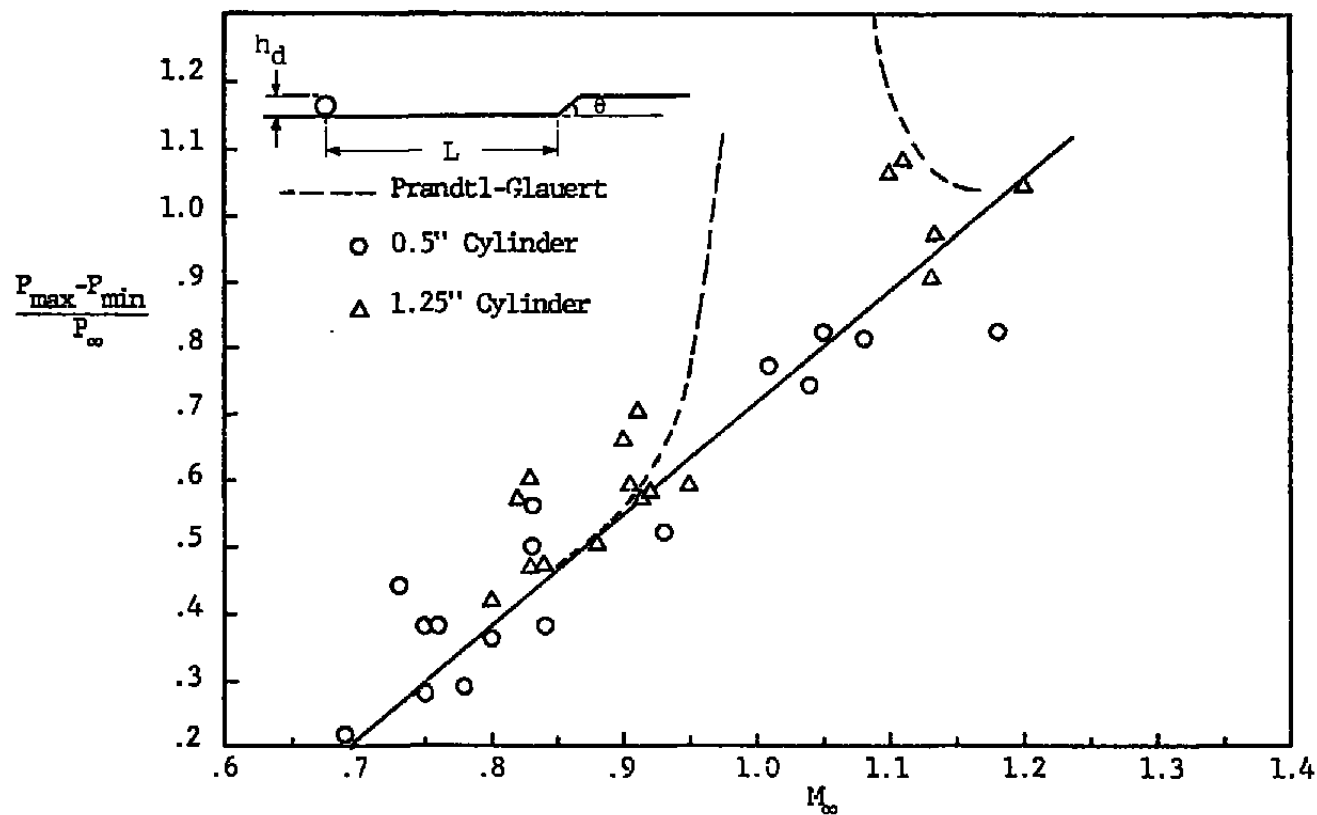


Figure 34. Variation of Disturbance Strength Against Free Stream Mach Number. P_{max} and P_{min} are Pressures Over the Cylinder.

a shallow cavity for which the shear layer has maximum energy redistributed into it from the free stream flow. In Fig. 35 the effect of disturbances of different strength, at a fixed distance upstream from the ramp, on the separation length in front of ramps with different angles is shown. As the disturbance size increases with nearly constant boundary layer parameters, the extent of the separation reduces (Fig. 35). As discussed for Fig. 34, the size of the upstream disturbances relative to the boundary layer thickness has an important effect, and probably a factor like (h_d/δ_o) should have been included in the definition of the disturbance strength. However δ_o was not measured for each run; therefore, the influence of this factor, (h_d/δ_o) , on $P_{max} - P_{min}/P_\infty$ could not be determined. Also, from Fig. 34 it is clear that the disturbance generated by the 0.5-inch cylinder is weaker than the one of the 1.25-inch diameter cylinder.

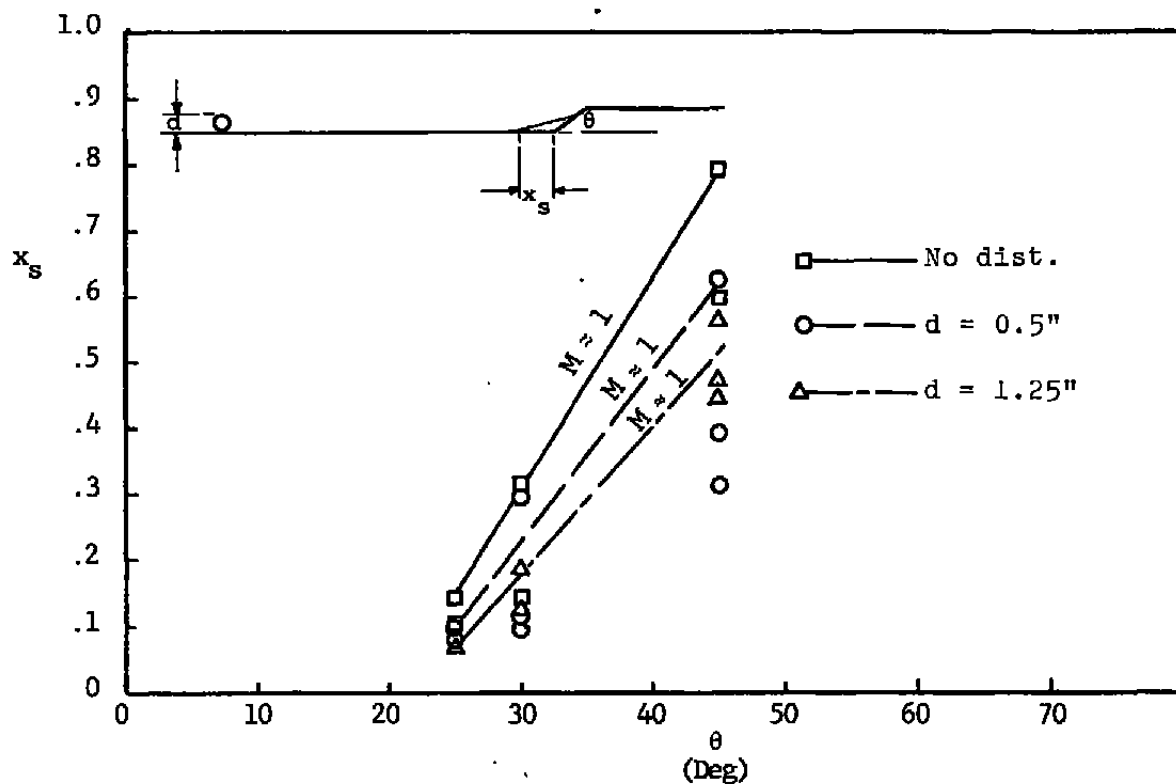


Figure 35. Separation Length Plotted Against the Ramp Angle in Presence of Upstream Disturbances of Different Size. Data taken at various Mach numbers with curves indicating trends for $M_\infty \approx 1$.

4.0 FLOW OVER FORWARD-FACING STEP

For the subsonic flow over a forward-facing step the surface static pressure rises steadily beginning several step heights ahead of the step, due to the loss of kinetic energy of the flow as it approaches the step. In the lower transonic and subsonic flow the pressure distribution on the model shows a maximum (peak) pressure point about one step height upstream of the step. In supersonic flow the pressure maximum occurs after a plateau pressure region downstream of separation (Fig. 36). Supersonic flow also produces higher maximum pressures and shorter upstream influence distances. The adverse pressure gradient generated due to the existence of the step is the sole reason for the flow to separate in front of the step. This is true practically for all step sizes except when the step height is negligible with respect to the undisturbed boundary layer thickness.

Figure 37 shows a typical surface pressure distribution over a forward-facing step with no upstream disturbance for subsonic flow. The characteristic pressure rise ahead of the step and the sharp drop in pressure due to the expansion of the flow on top of the step are clearly visible. The pressure distribution resulting from the introduction of a 0.5-inch diameter cylinder as an upstream disturbance is given in Fig. 38. The free stream Mach number and Reynolds number for the flows of Figs. 37 and 38 are essentially identical. Comparison of these two plots shows the following for the disturbed flow:

- (i) Earlier pressure rise ahead of the step
- (ii) Lower maximum pressure ahead of the step
- (iii) Faster pressure recovery downstream of the step

Figure 39 shows the pressure distribution for the flow with $M_\infty = 1.4$ over the geometry of Fig. 38. Comparing Figs. 38 and 39 shows the following for the supersonic flow:

- (i) Slower pressure rise ahead of the cylinder
- (ii) Higher maximum pressure on the cylinder
- (iii) Larger pressure drop behind the cylinder
- (iv) Slower initial pressure recovery behind the cylinder
- (v) Lower plateau pressure
- (vi) Identical pressure recovery rate near the step
- (vii) Slightly higher maximum pressure ahead of the step
- (viii) Larger pressure drop at the top of the step
- (ix) Retarded pressure recovery at the top of the step, and a possible separated region on the top of the step

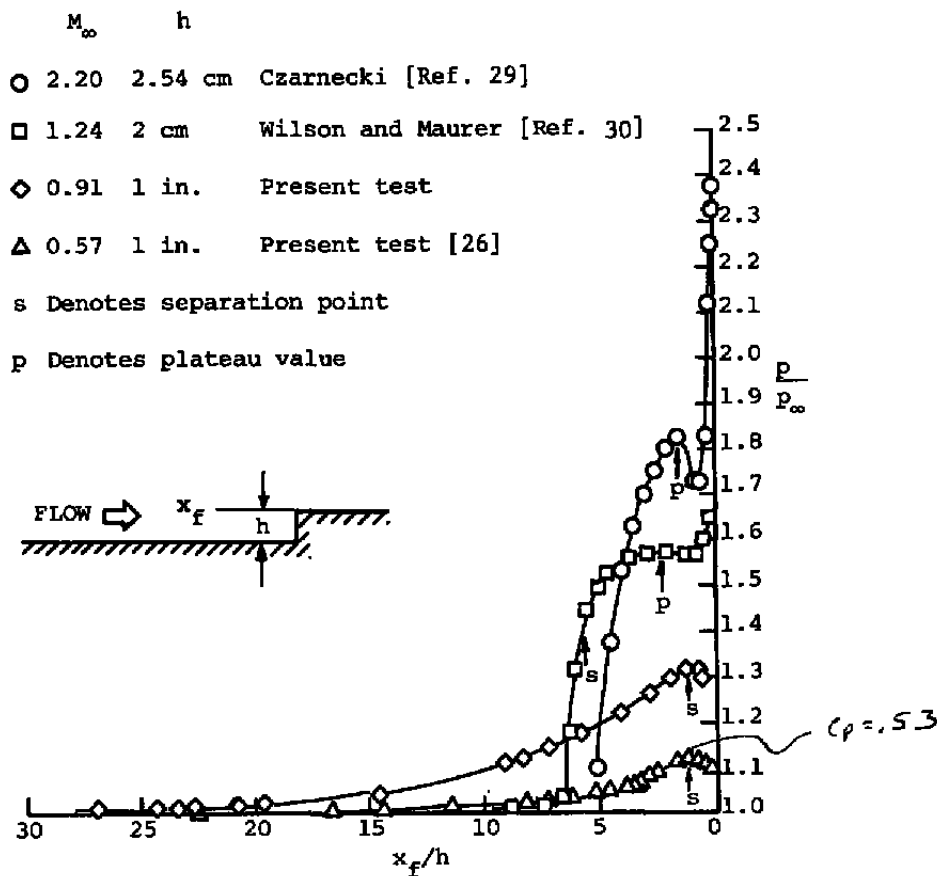


Figure 36. Comparison of Pressure Distributions for Sub-, Trans- and Supersonic Flow Ahead of a Forward-Facing Step.

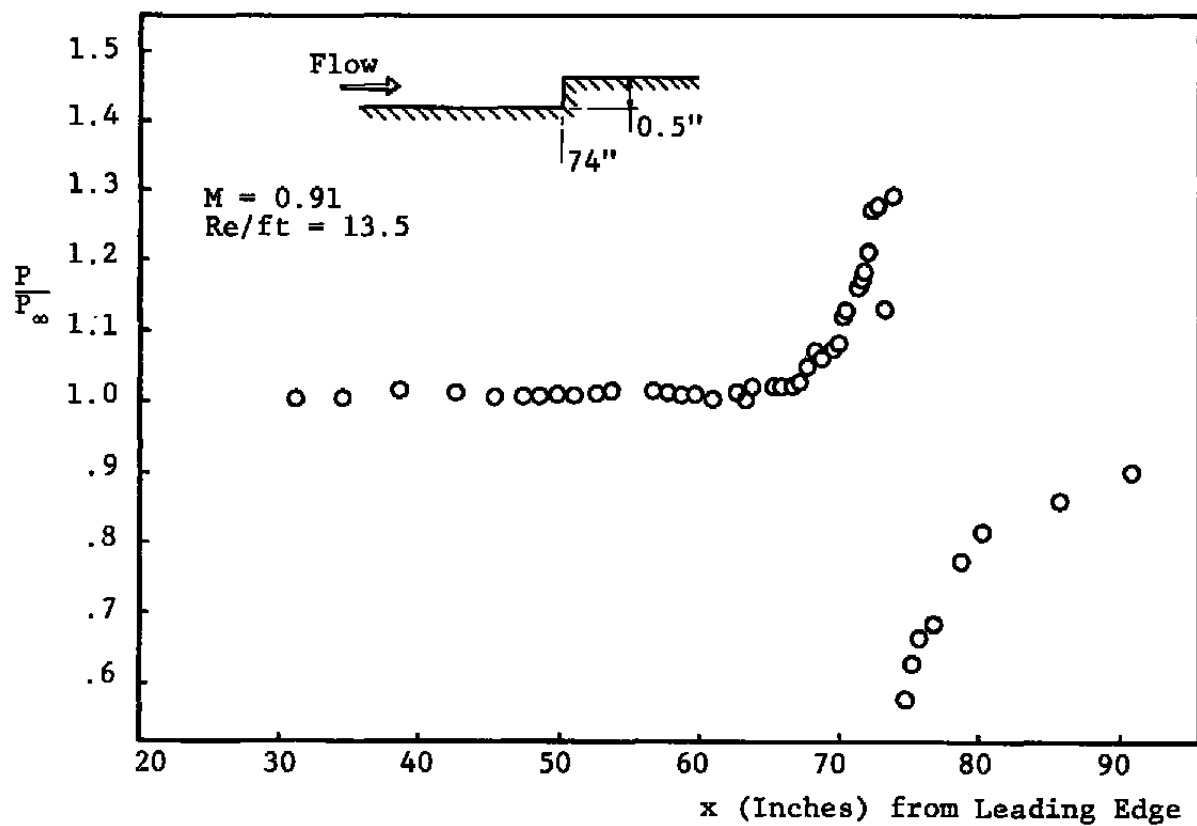


Figure 37. Static Pressure Distribution in Subsonic Flow Over Forward-Facing Step.

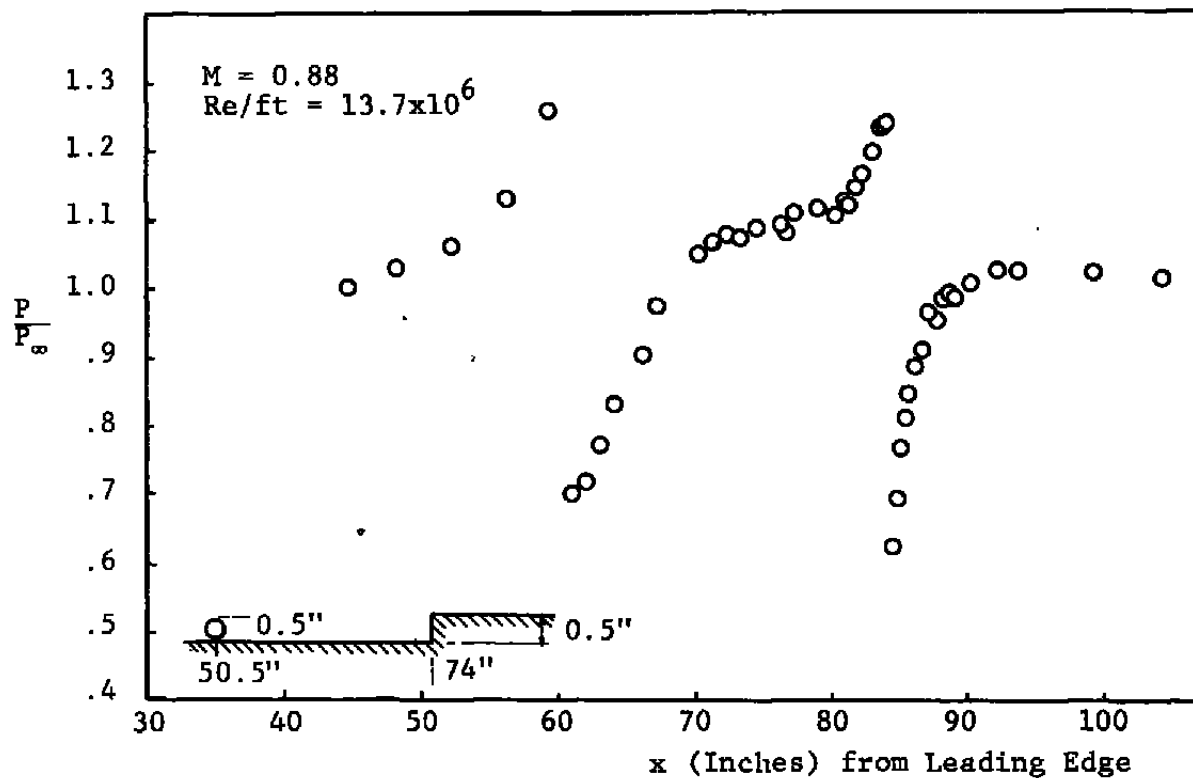


Figure 38. Static Pressure Distribution in Subsonic Flow Over Forward-Facing Step with 0.5-Inch Cylindrical Disturbances.

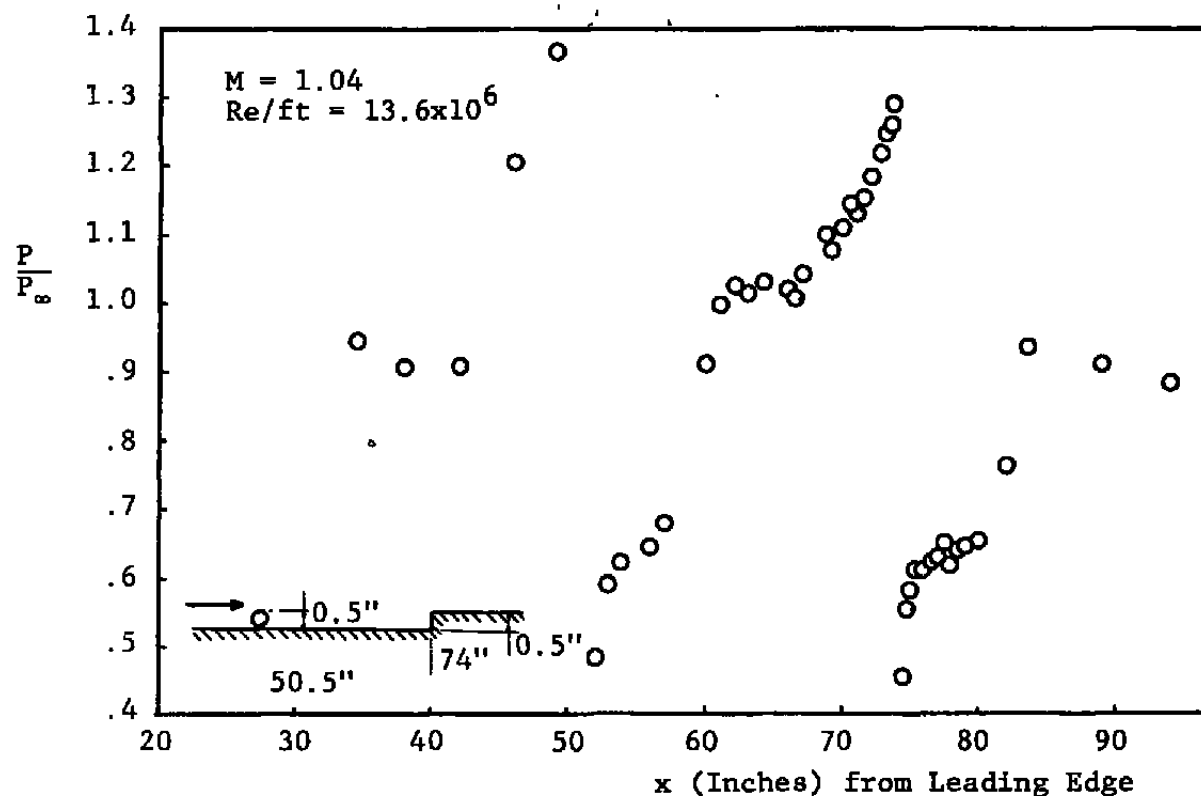


Figure 39. Static Pressure Distribution in
 Supersonic Flow Over a Forward-Facing
 Step with 0.5-Inch Cylindrical
 Upstream Disturbance.

Figures 40 and 41 show the Schlieren photographs with corresponding pressure distributions for the configurations in Figs. 38 and 39.

The flow over forward-facing steps has been discussed in detail by Chen (Ref. 26), and therefore it will not be discussed in more detail here. However, some new correlations obtained from this study are discussed in connection with the flow over forward-facing ramps and shallow cavity flows.

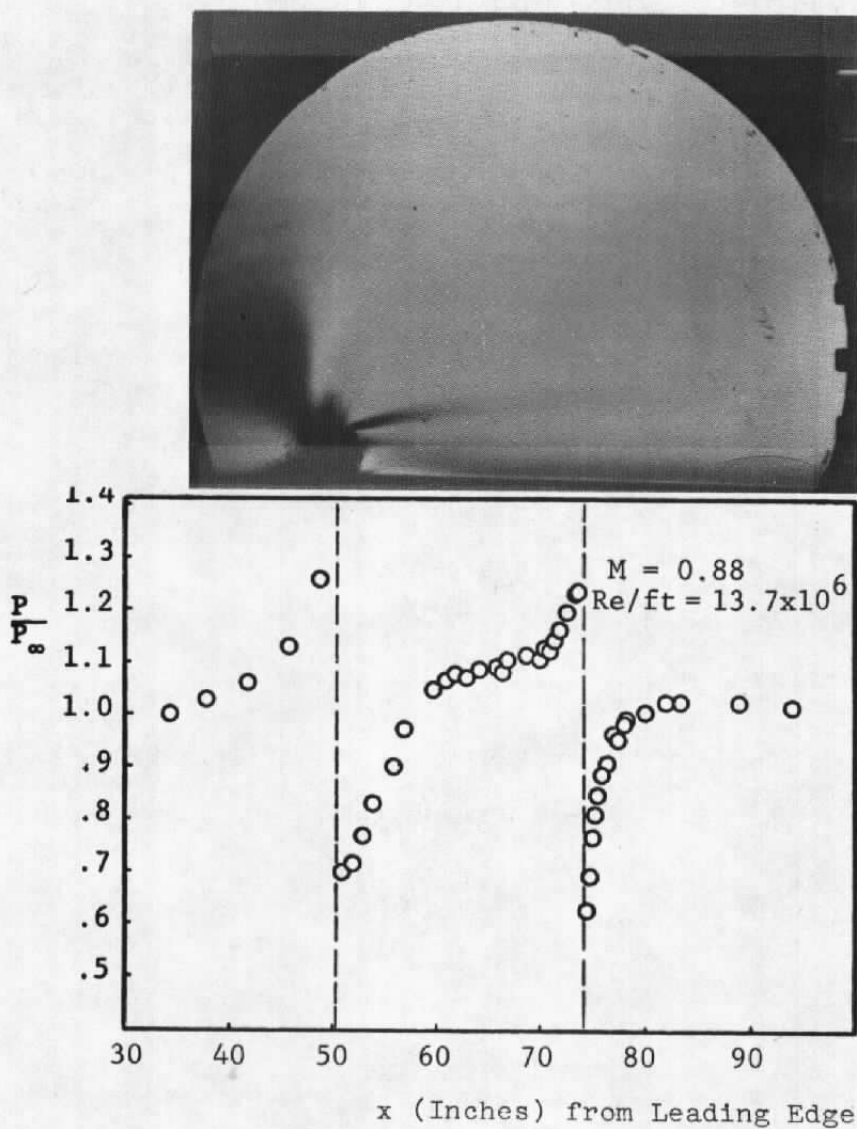


Figure 40. Schlieren Photograph and Static Pressure Distribution in Subsonic Flow Over Forward-Facing Step with 0.5-Inch Cylindrical Disturbance.

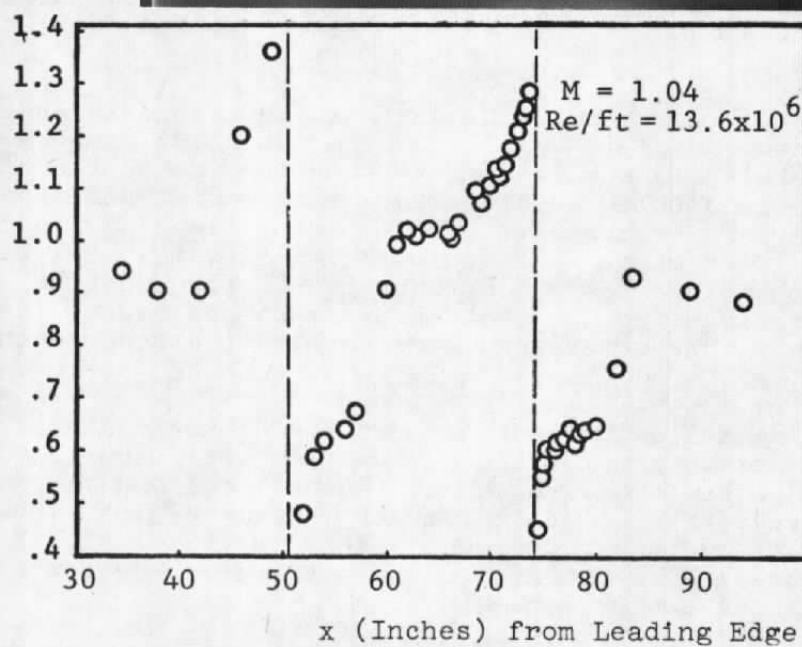
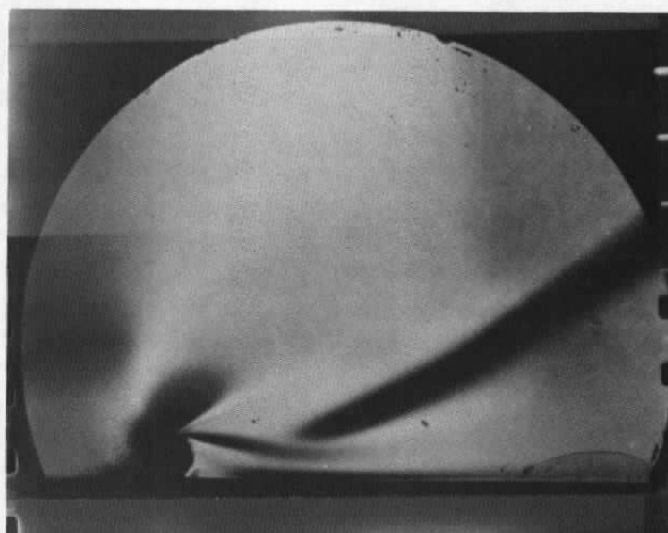


Figure 41. Schlieren Photograph and Static Pressure Distribution in Supersonic Flow Over Forward-Facing Step with 0.5-Inch Cylindrical Disturbance.

5.0 TURBULENT FLOW OVER CAVITIES

The turbulent transonic flow over cavities of different length-to-depth ratios (l/h) was studied and an attempt was made to relate the results of the cavity flow to the partially separated transonic flow over airfoils.

The turbulent boundary layer separates at the top of the rearward-facing step. Depending on the length to depth of the cavity, the flow reattaches on the cavity floor. After the reattachment point a new shear layer starts developing and the flow starts to relax from the disturbance introduced to it by passing over the step and the separated region. If l/h is small, the flow may not reattach on the cavity floor or it may become unstable, causing the flow to reattach periodically, producing a very complicated unsteady pattern. Figure 42 shows the regions for unattached, unstable and attached flow for cavities of different sizes. There has been no attempt in the present investigation to study the detail of the unsteady phenomenon if it occurs. Only flows with stable conditions will be discussed.

Typical features of the surface pressure distribution for flow over a cavity, with Mach and Reynolds numbers in the range of this study, are sketched in Fig. 43. Surface oil flow was used to identify the reattachment and separation locations accurately, on the cavity floor and on the surface of the steps. Figure 44 shows a typical oil flow photograph. The flow which separated in front of the forward-facing step does not reattach at the top of the step, but rather reattaches somewhere on the face of the step.

In the following sections details of the characteristic pressure parameters for the cavity flow are discussed and an attempt has been made to correlate the local and free stream parameters using the present experimental results. Cavity flow has been discussed by Chen (Ref. 26) in detail, so an attempt has been made here to concentrate on the correlating aspect of the cavity parameters.

5.1 BASE PRESSURE

As the flow passes over the rearward-facing step it expands, depending primarily on the cavity dimension, to a minimum or base pressure. The sudden discontinuity in the boundary causes the flow to separate at the top corner of the rearward-facing step. The flow will be stable and

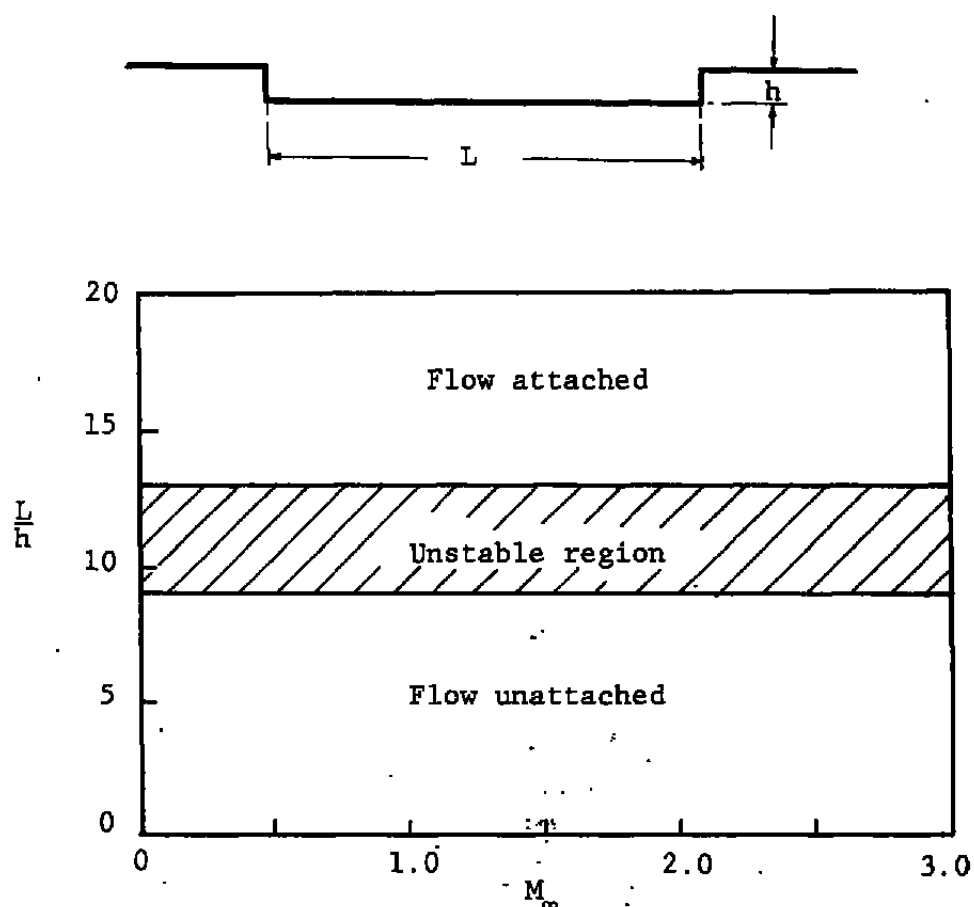


Figure 42. Nondimensional Critical Cavity Length. Reference [26].

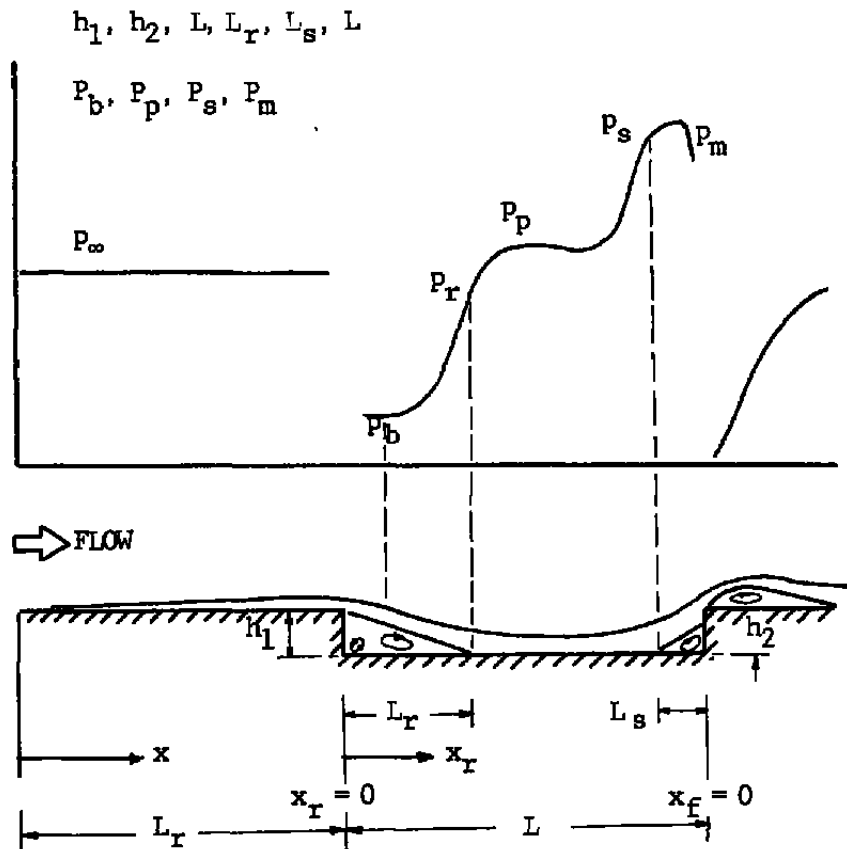


Figure 43. Nomenclature and Schematic Diagram of the Pressure Distribution and the Flow Over a Shallow-Cavity Model.

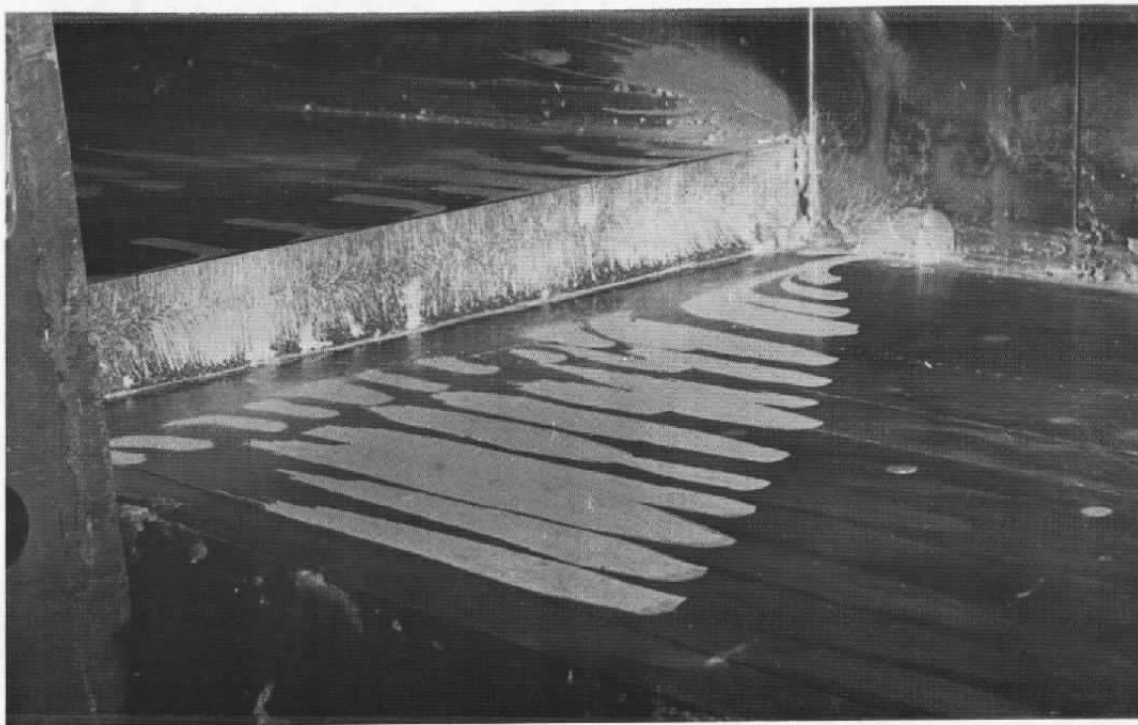


Figure 44. A Typical Oil Flow Pattern Upstream and on the Forward-Facing Step.

reattach on the cavity floor if the cavity length-to-depth ratio is greater than 13 (Fig. 42). Variation of the base pressure nondimensionalized with the total pressure, for various cavity geometries, is plotted in Fig. 45. The base pressure decreases as the Mach number increases. This decrease is linear up to $M_\infty \sim 1.0$, with greater decreases in this region. The interesting point from this plot is the fact that in this flow range the cavity geometry has little or no effect on this parameter P_b/P_t . To clarify this point, P_b/P_t versus L/h is plotted in Fig. 46, and it is obvious that there is no dependency on cavity geometry. However, P_b/P_∞ , plotted versus L/h in Fig. 47, shows a slight decrease as L/h increases. The Reynolds number influence on P_b/P_∞ in the range investigated ($4 \times 10^7 < Re < 19 \times 10^7$) could not be isolated from the data.

5.2 REATTACHMENT PRESSURE

The flow which separates from the top corner of the rearward-facing step reattaches at a downstream point on the cavity floor, enclosing a region of separated flow of low velocity and nearly constant pressure. The separated shear layer reattaches in a region of adverse pressure gradient. The rise in surface pressure reverses part of the fluid in the shear layer and feeds it back into the recirculating region, while part of the fluid with higher velocity escapes the dead zone in the base region. The reattachment pressure for subsonic flow is higher than the free stream static pressure.

The reattachment distance is a maximum in the transonic region and decreases as supersonic flow is obtained. Figure 48 shows the separation distance as a function of Mach number, and the increase in the separation distance in the neighborhood of $M_\infty \sim 1$ is obvious. Similar to the base pressure, the nondimensionalized reattachment pressure with respect to total pressure decreases linearly as the free stream Mach number increases (Fig. 49). For a fixed free stream Mach number, P_r/P_∞ versus L/h has a minimum corresponding to a cavity length-to-depth ratio of 30 - 40 (Fig. 50). However P_r/P_t remains independent of cavity geometry (Fig. 51), which shows that P_t is a more proper choice of reference pressure for the nondimensionalization of P_r .

5.3 PLATEAU PRESSURE

After the reattachment point the static pressure on the cavity floor overshoots and then levels out at the plateau pressure which is normally higher than the free-stream

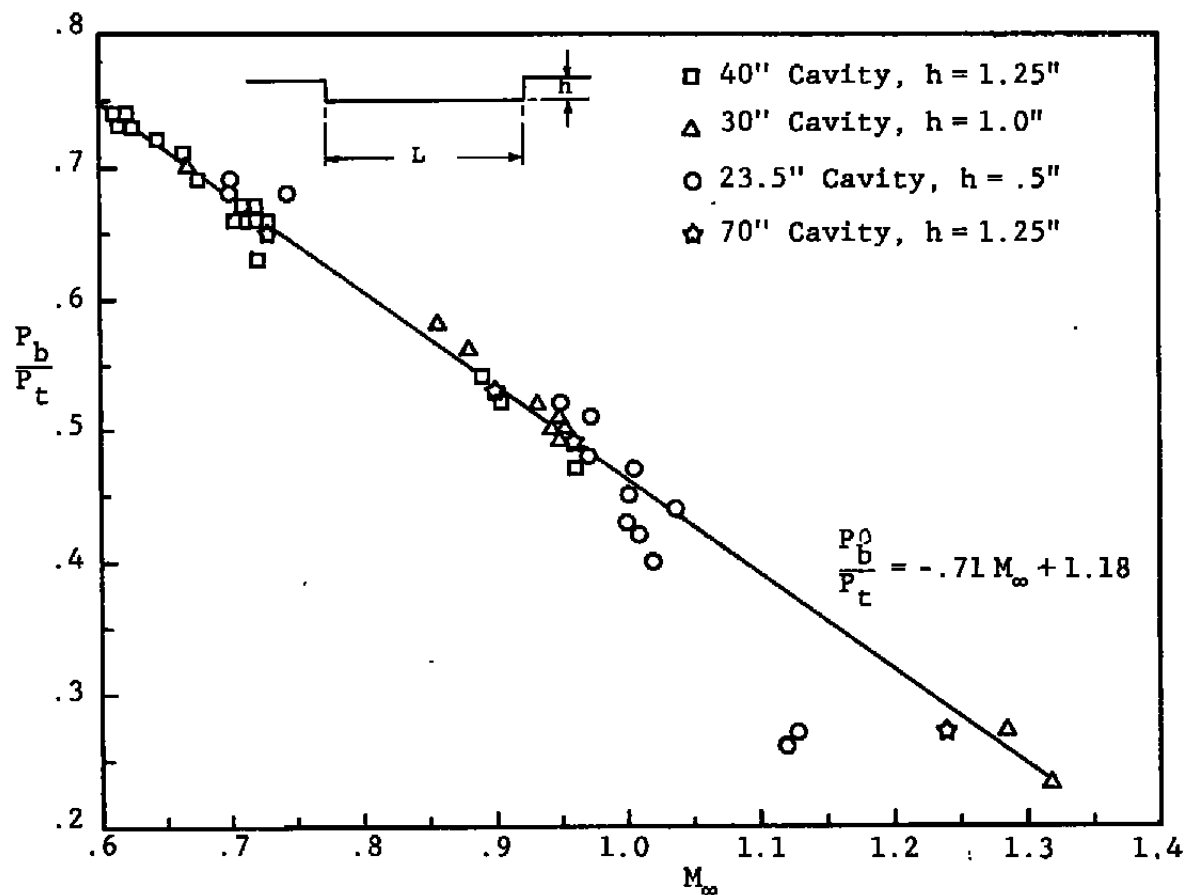


Figure 45. Variation of Base Pressure Against Free Stream Mach Number for Shallow Cavity.

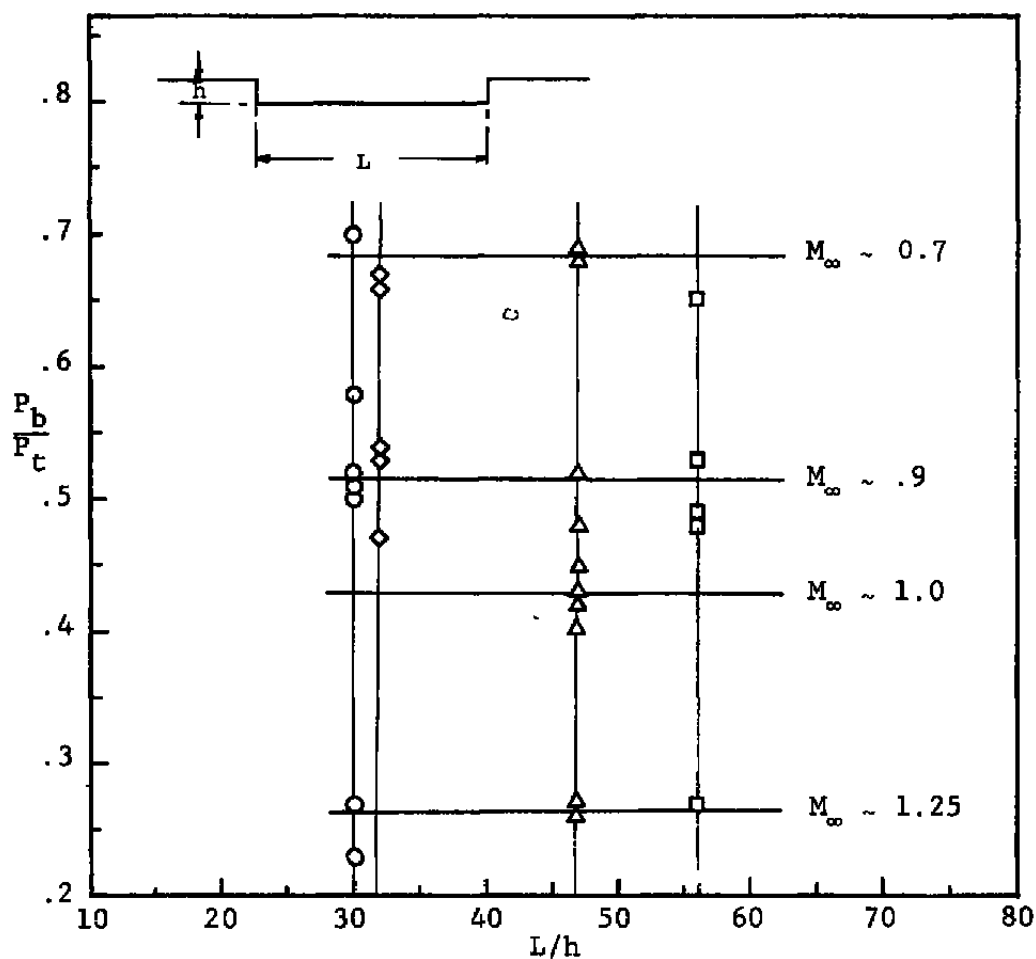


Figure 46. Variation of Base Pressure Normalized with P_t Against Cavity Geometry. Data are taken at various Mach numbers with lines indicating trends at each Mach number.

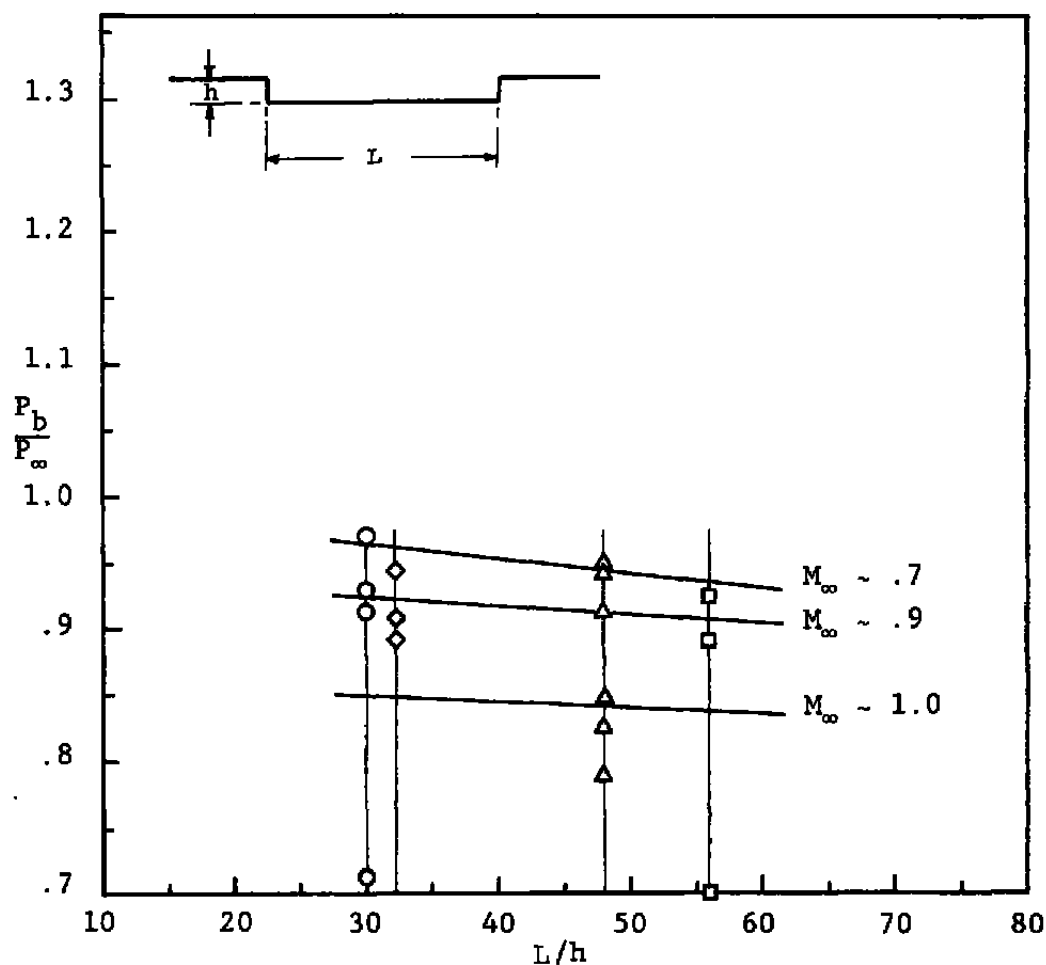


Figure 47. Variation of Base Pressure Normalized with P_∞ Against Cavity Geometry. Data are taken at various Mach numbers with lines indicating trends at each Mach number.

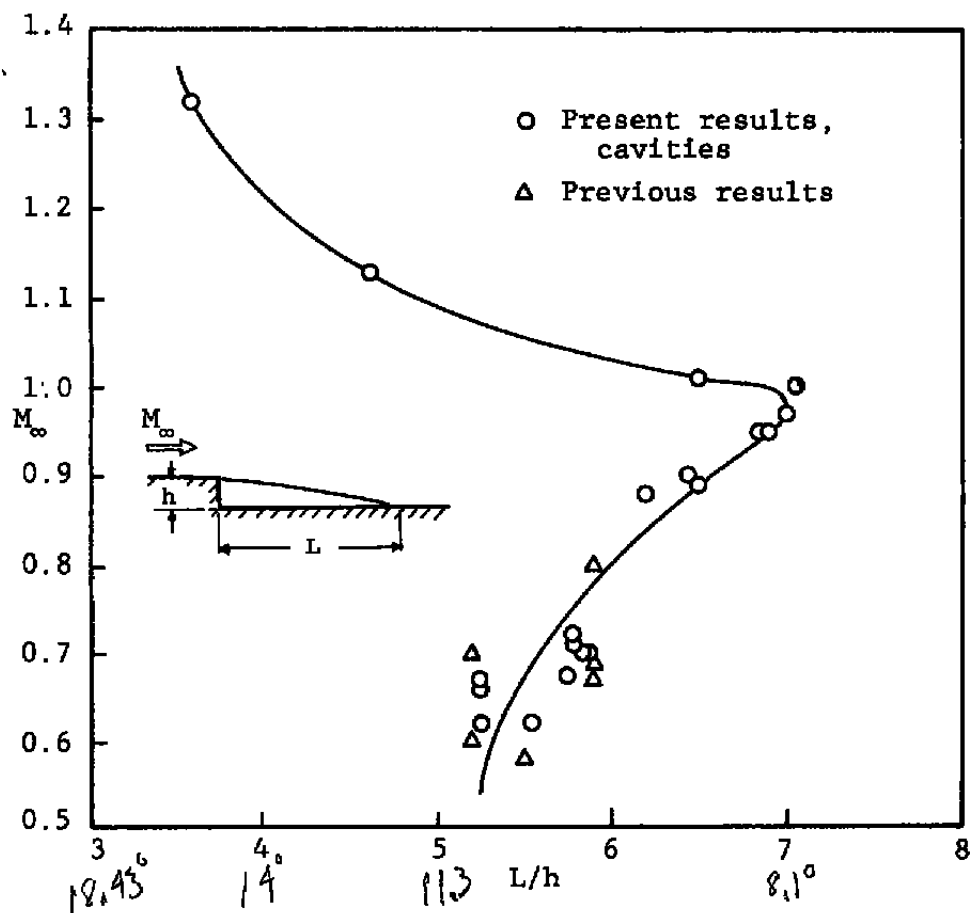


Figure 48. Variation of Reattachment Distance with Mach Number.

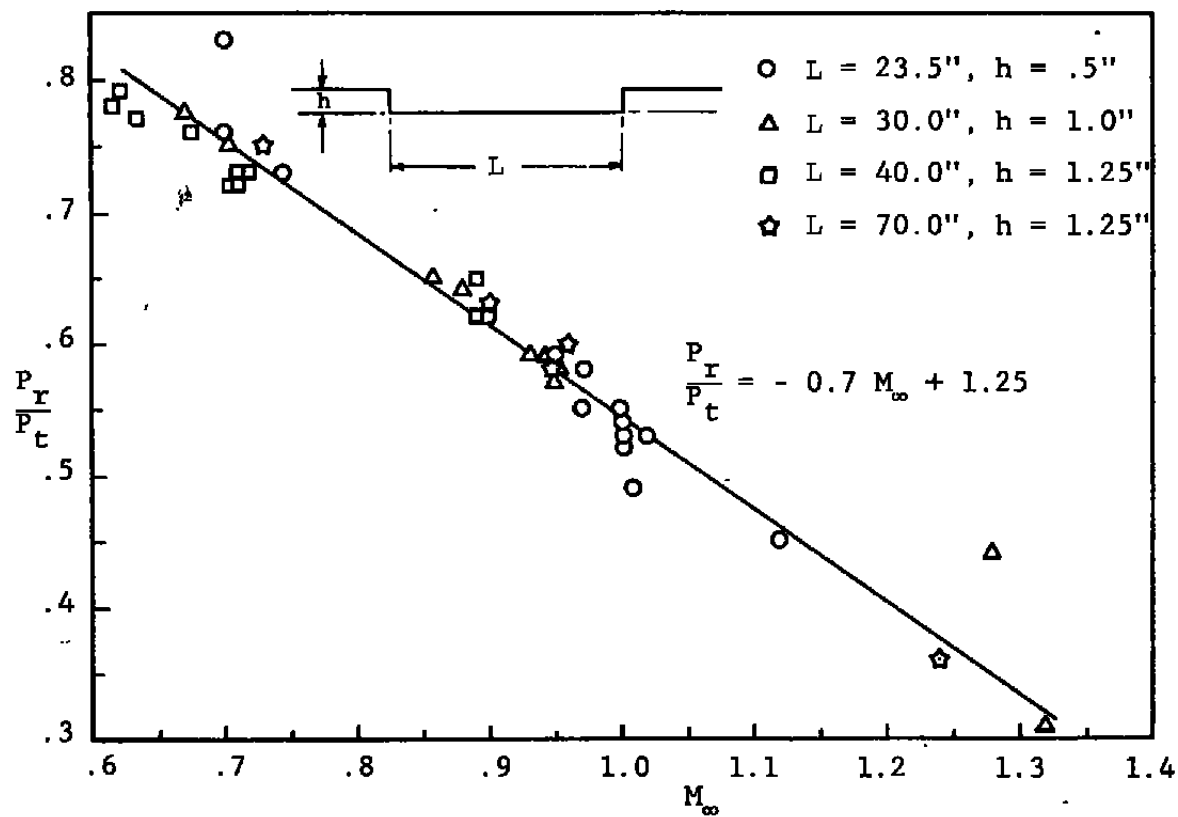


Figure 49. Variation of Reattachment Pressure with Free Stream Mach Number for a Shallow Cavity.

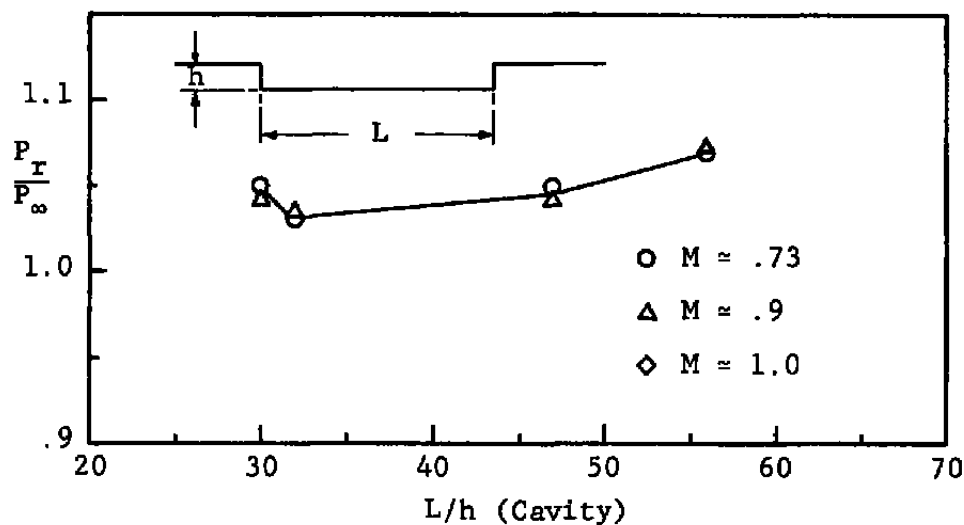


Figure 50. Variation of $\frac{P_r}{P_\infty}$ Against Cavity Geometry.

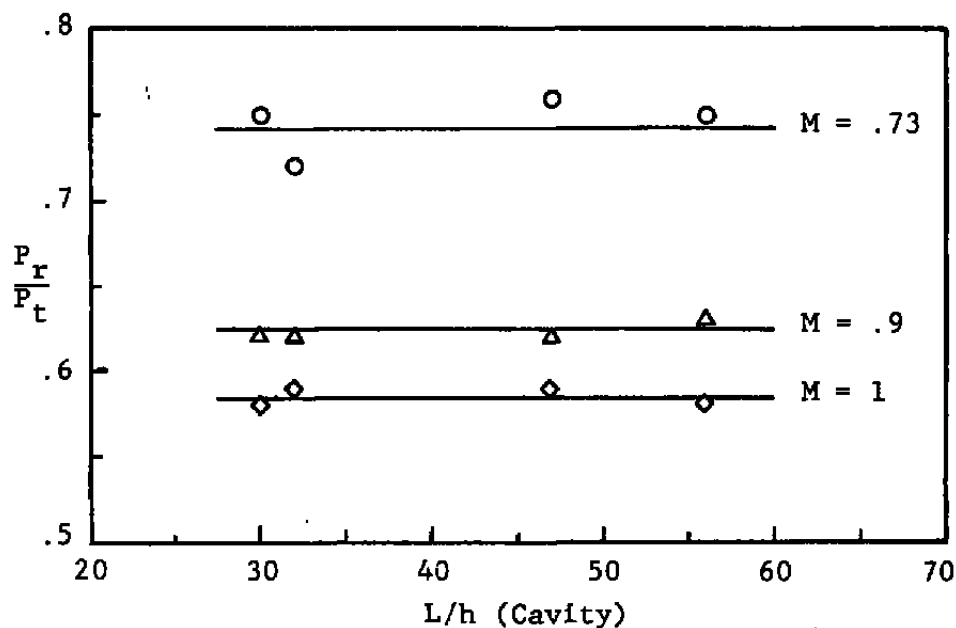


Figure 51. Variation of $\frac{P_r}{P_t}$ Against Cavity Geometry.

static pressure. Immediately after the reattachment point a new shear layer starts developing with the disturbed shear layer on top of it. Along the plateau pressure section the disturbed flow undergoes a relaxation process. If the cavity length/height is decreased the plateau pressure increases (Fig. 52), due to the upstream influence of the adverse pressure gradient ahead of the forward-facing step.

The plateau pressure variation as the free stream Mach number changes is small (Fig. 53). However, when the Mach number has reached the supersonic range it begins to increase rapidly with increasing Mach number.

The Reynolds number effect on P_p/P_∞ seems to be very negligible. In Fig. 53 the Reynolds number varied over the range $30 \times 10^6 < Re_x < 10 \times 10^7$ and no clear variations which could be caused by Reynolds number effect can be observed. The plateau pressure nondimensionalized with respect to total pressure shows a definite linear dependence on the free stream Mach number (Fig. 54). As the free stream Mach number increases the plateau pressure decreases linearly. These data exhibit much less scatter compared to the P_b/P_t or P_r/P_t data discussed earlier. This probably means that the plateau pressure is not very sensitive to parameters which were not controlled during the present tests and which has a secondary influence on the base and recovery pressures.

5.4 SEPARATION PRESSURE

As the flow proceeds downstream toward the forward-facing step from the plateau pressure region, it faces the steep adverse pressure gradient due to the presence of the step. Depending on the total kinetic energy available, the turbulent flow can proceed forward only a certain distance at which point it separates. The separation pressure was found by the use of surface oil flow as follows. First, the separation distance in front of the step was accurately measured from the oil flow traces. Then, using the surface pressure measurements and the separation distance, the separation pressure was identified. The surface oil flow technique is quite accurate and several investigators have used this technique for a similar purpose. It is assumed that the separation pressures found using the surface oil flow were quite accurate. However, the oil flow technique was not used for all of the tests. For the tests with no oil flow the separation pressure was found from the measured static pressure distribution only.

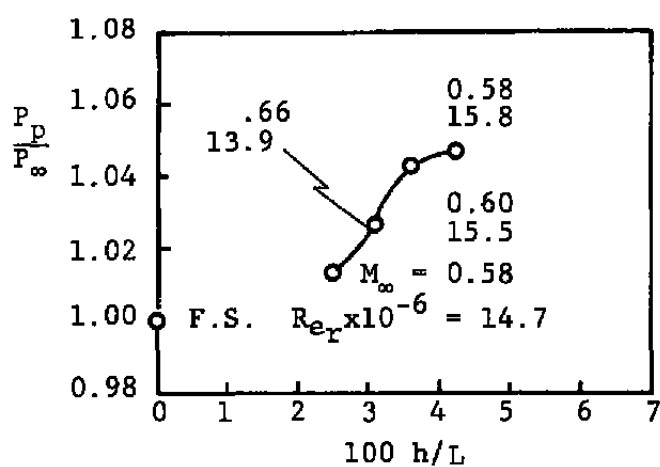


Figure 52. Effect of Depth to Length Ratio on the Plateau to Free Stream Pressure Ratio. Reference [26].

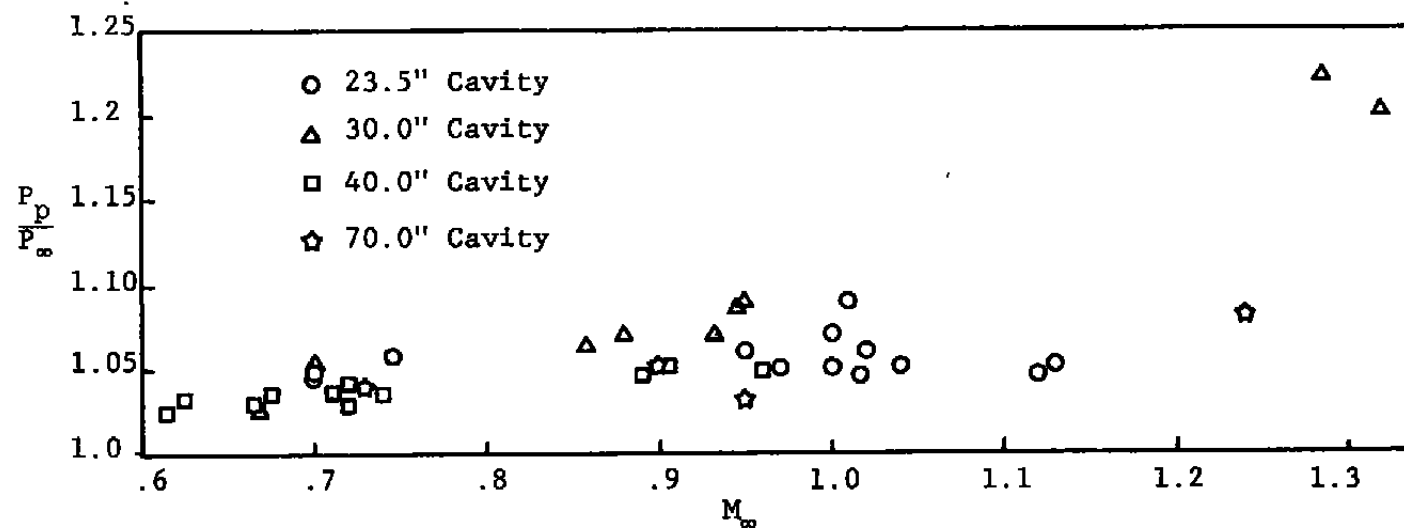


Figure 53. Variation of Plateau Pressure in Flow Over Cavities with Free Stream Mach Number.

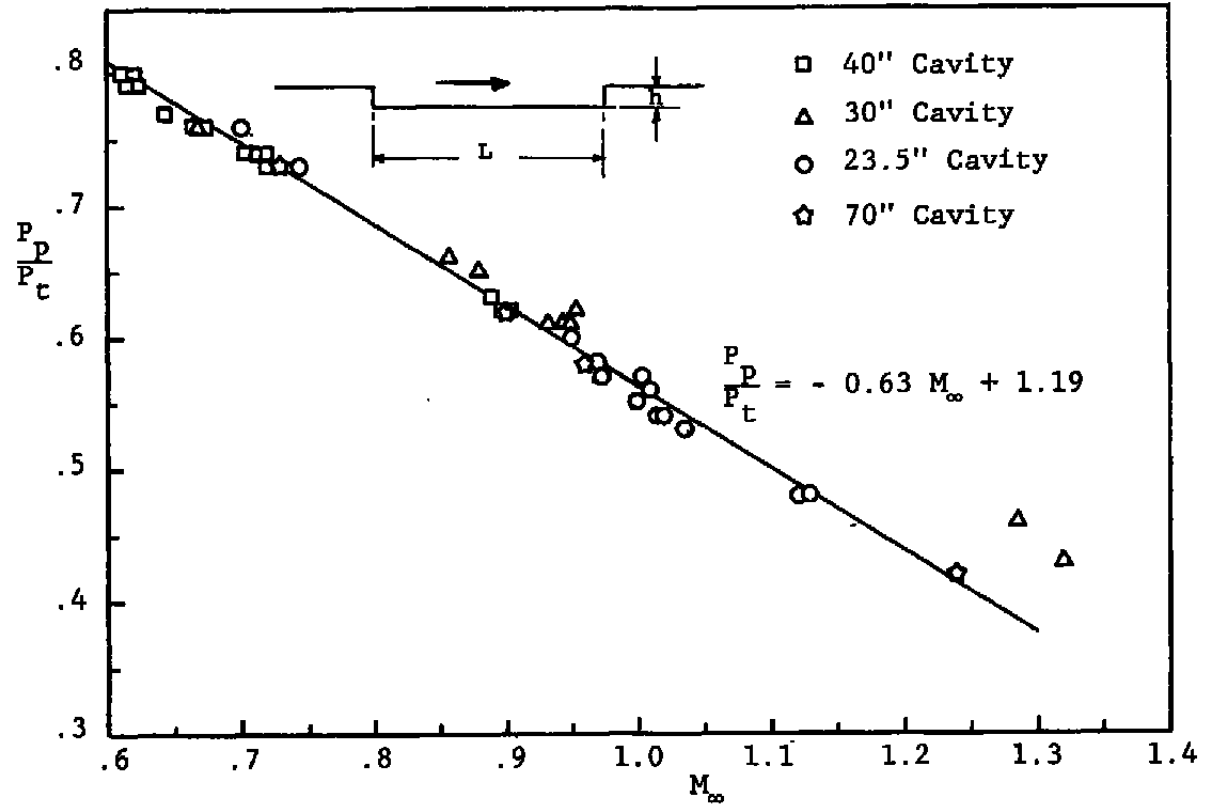


Figure 54. Variation of Plateau Pressure in Flow Over a Shallow Cavity Against Free Stream Mach Number.

The separation pressure increases linearly with Mach number (Fig. 55). Notice that the data for the flow over a forward-facing step which is equivalent to a cavity of infinite length follows the same trend. The Reynolds number has little or no explicit effect on the separation pressure in range of high Reynolds numbers examined (Fig. 56). In these cases the maximum pressure was used rather than the separation pressure because separation occurred just prior to the point of maximum pressure and the maximum pressure could be determined very accurately. The discussion will emphasize the maximum rather than the separation pressure.

5.5 MAXIMUM PRESSURE

After the flow separates in front of the step, the wall static pressure increases slightly to a maximum (peak) pressure at a position very close to the face of the forward-facing step. After this point the pressure drops and the flow expands to the free stream condition over the top corner. At the top of the step the flow generally separates again, but this will not be discussed here. The maximum pressure depends linearly on the Mach number with the same slope as the separation pressure, when both are normalized with the free streams static pressure (Figs. 56 and 57). This indicates that P_m/P_∞ is a parameter which behaves similarly to the separation pressure. However, the maximum pressure is very much easier to measure experimentally, while the determination of separation pressure is difficult both theoretically and experimentally. Experimentally there are generally errors associated with its measurement due to the flow sensitivity in the region of separation. Therefore, a close approximation to the separation pressure, i.e., the maximum pressure, will be of interest, especially since they vary similarly.

Comparison of an infinitely long cavity (forward-facing step) and a shallow cavity of finite length illuminates the relation between the maximum and plateau pressures. The two configurations are expected to be similar because the cavity pressure rises from the plateau to the maximum pressure while for a forward-facing step (cavity of infinite length) the maximum pressure is reached from the free stream pressure. Therefore, in a macroscopic scale some similarity of the above mentioned flow fields should exist. Figure 58 compares the parameters P_m/P_∞ and P_p/P_∞ , for the various geometries shown on the figure. In Fig. 59, P_m/P_p is plotted against the free stream Mach number. The data indicate quite some scatter in the region of $.85 < M_\infty < 1$. This scatter of data in the neighborhood of $M_\infty \sim 1.0$ which is seen in several figures may be due to interference

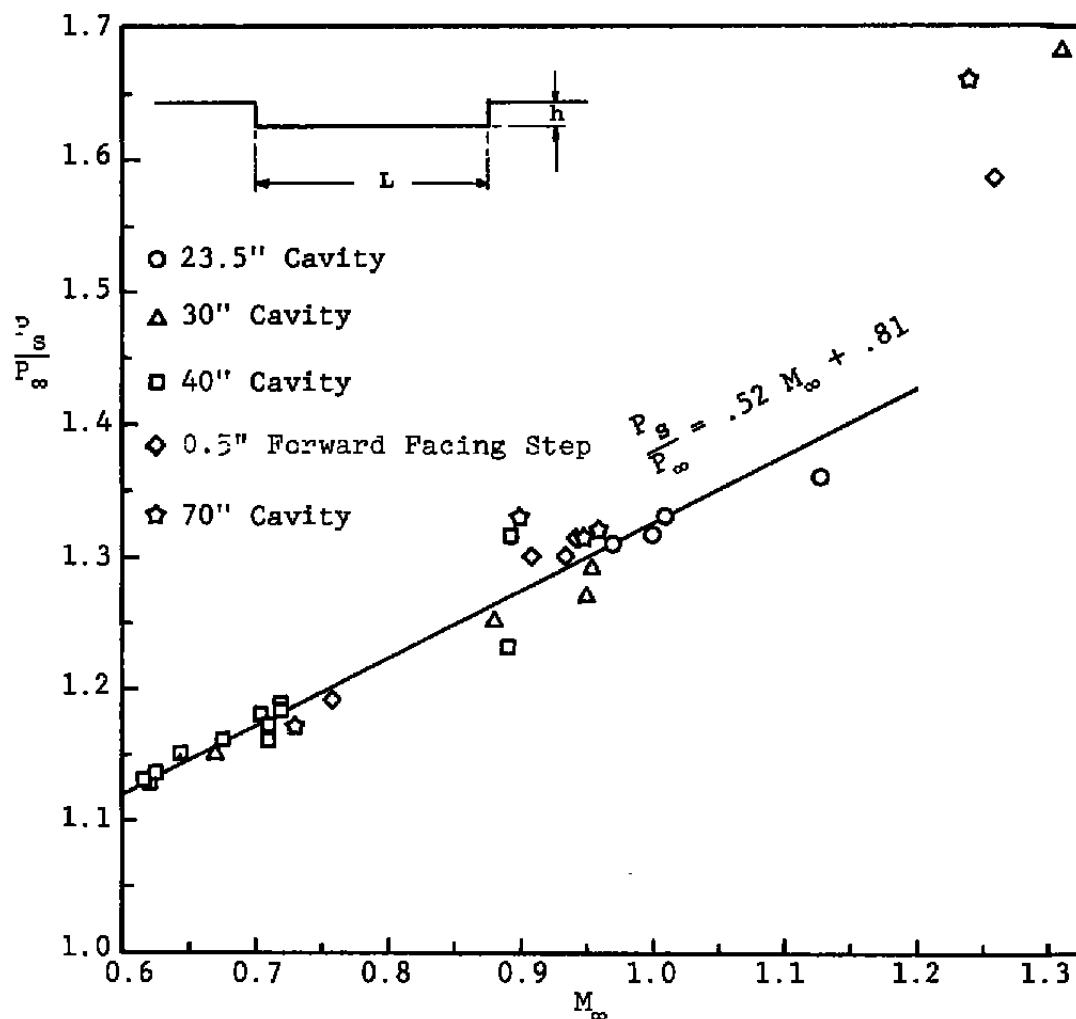


Figure 55. Variation of Separation Pressure in Flow Over Shallow Cavity Against Mach Number.

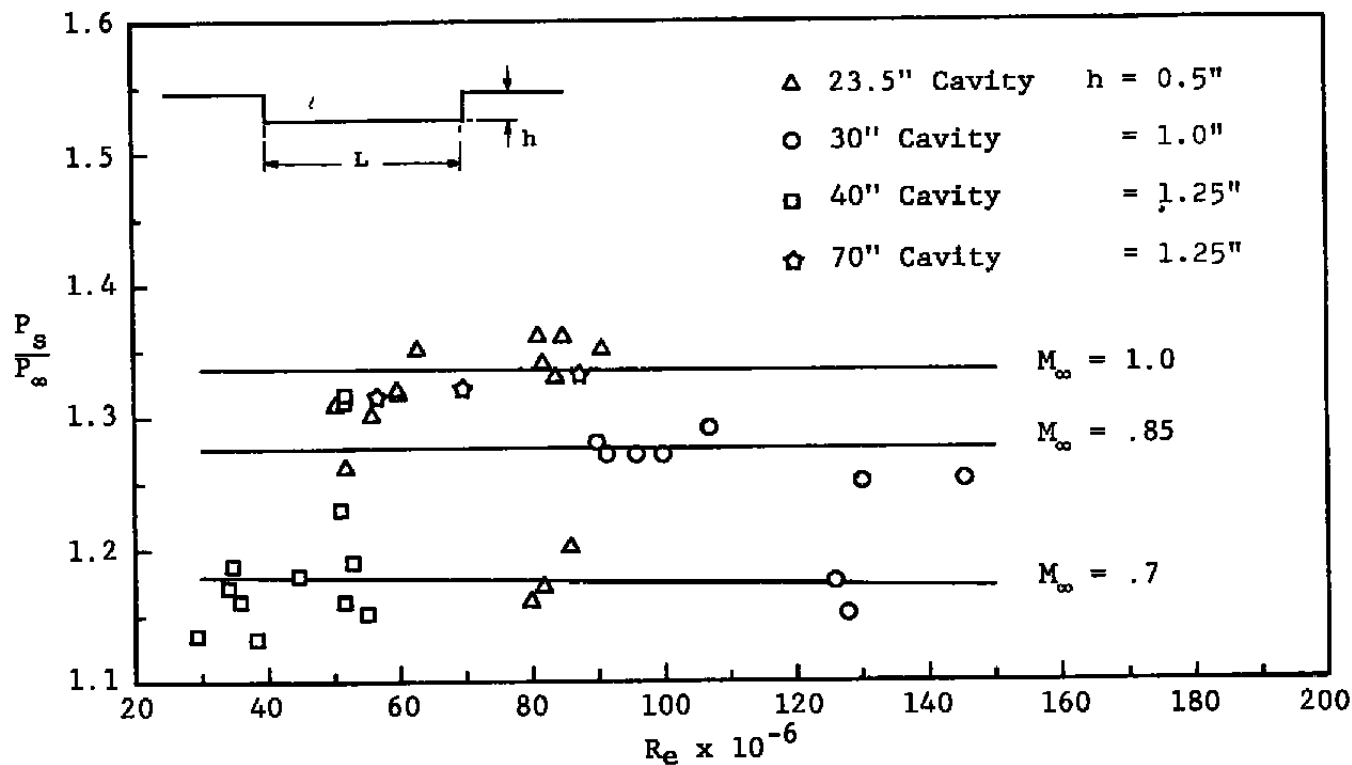


Figure 56. Reynolds Number Effect on the Separation Pressure in Flow Over a Shallow Cavity with the Mach Number Influence. Data not at a uniform M_∞ .

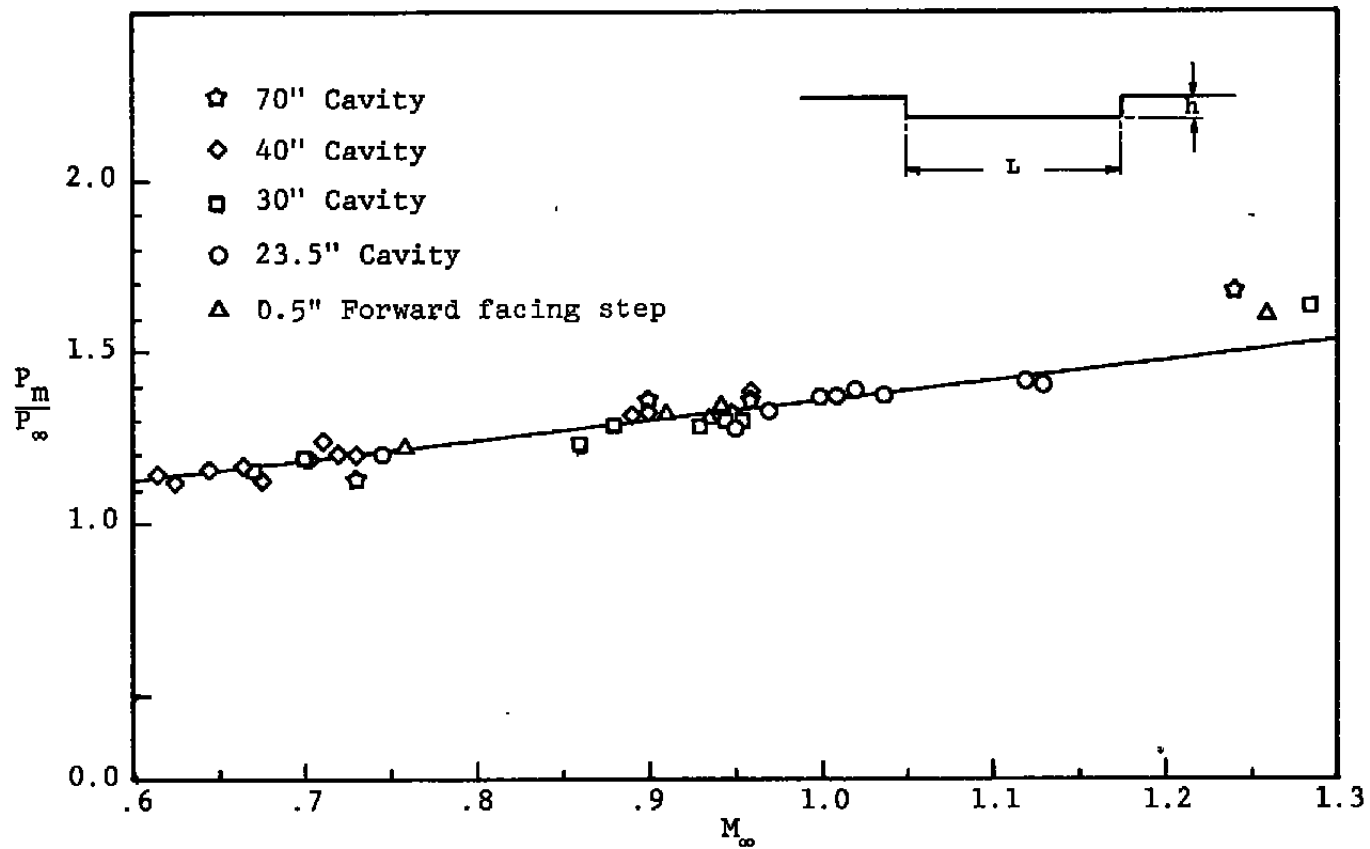


Figure 57. Variation Peak Pressure in Flow Over Shallow Cavity Against Mach Number.

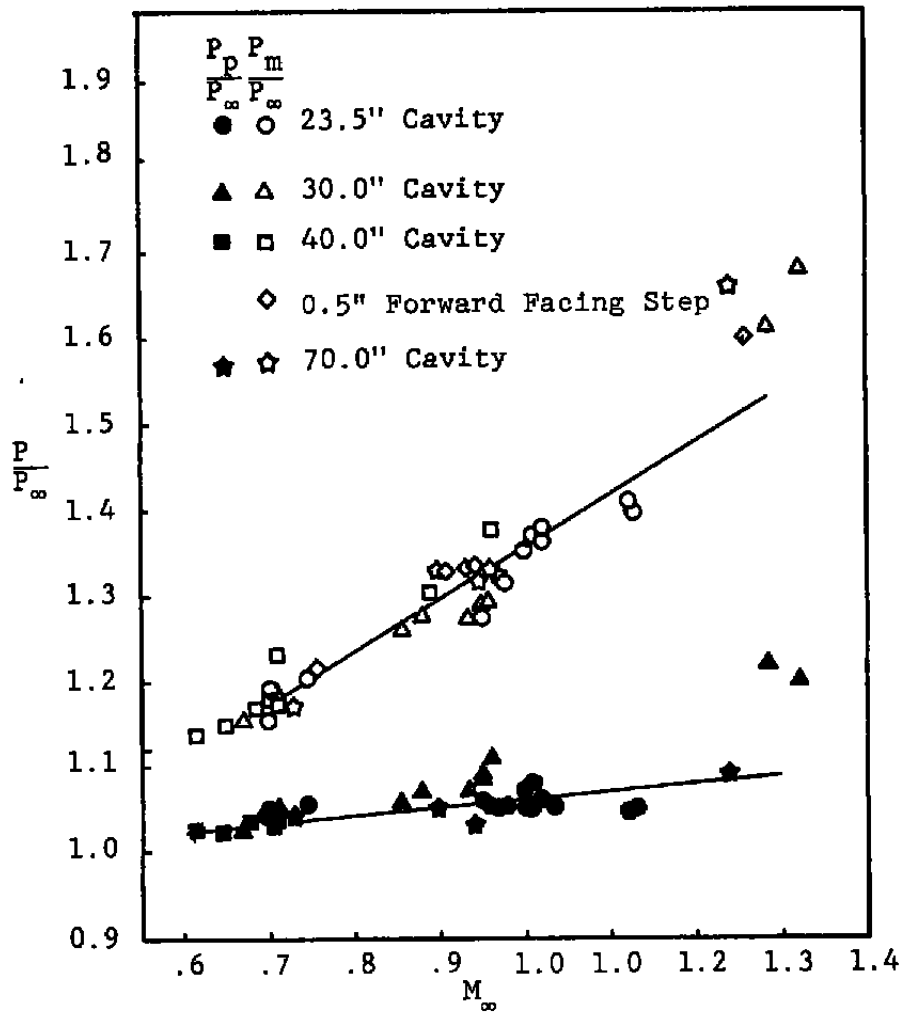


Figure 58. Comparison of Plateau and Peak Pressure Against Free Stream Mach Number.

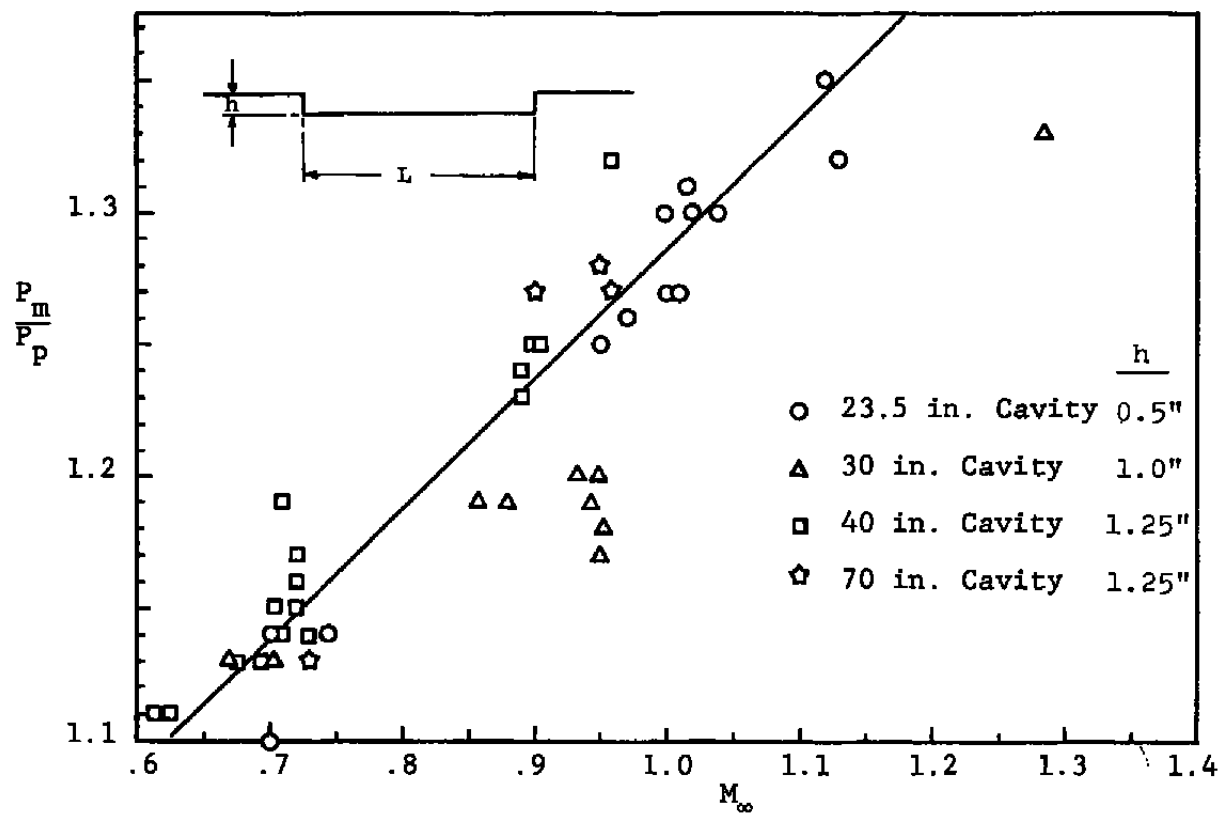


Figure 59. Variation of P_m/P_p in Flow Over Cavity Against Free Stream Mach Number.

effects in the transonic range. This point is clarified in Fig. 60, where the variation in P_m/P_∞ with the geometry of cavity is seen to intensify in the range of $M_\infty \sim 1$, where the scatter existed on Fig. 59. For subsonic flow P_m/P_∞ varies only slightly as the cavity length-to-depth ratio changes. It is also obvious from this figure that, to obtain the highest maximum pressure possible, the geometry of cavity is critical. In other words, there is an optimum cavity length ratio (L/h) for which the upstream disturbance is most effective in constructively influencing the downstream flow to produce the largest possible maximum pressure before the forward-facing step. The exact physical phenomena that causes this effect is not clear, except it is known that transonic flow is very sensitive to any disturbances. The correct cavity length is important in providing the optimum relaxation distance for the disturbed transonic flow. The optimum relaxation distance is that distance which yields the necessary energy distribution to result in the highest peak pressure before the forward-facing step. This means that this configuration resists separation most effectively. Therefore, if we call this phenomena energizing the boundary layer, it would be of practical interest to apply this result to an airfoil. Since the maximum pressure increase over the airfoil is limited, a proper design that would utilize this concept of energization of the boundary layer may eliminate separation of the flow over the airfoil.

The maximum pressure normalized with the total pressure decreases linearly as the free stream Mach number increases (Fig. 61). Since the total pressure is related to Reynolds number, we can implicitly correlate P_m and Re as has been discussed previously.

5.6 COMPARISON OF CAVITY FLOW AND TRANSONIC FLOW OVER AIRFOIL

Practically no analytical solutions for transonic flow over airfoils exist when part of the flow is separated. Alternative solutions are frequently sought using numerical methods. The numerical calculations for viscous flow often contain parameters, like the Reynolds stresses, which need to be mathematically modeled. This mathematical modeling is not exact and rather approximate. Therefore, different correlations (approximations) are adopted for these parameters which are assumed to be valid for each particular case and depend on the availability of experimental data. Experimental data are then used to compare the accuracy of the numerical solution.

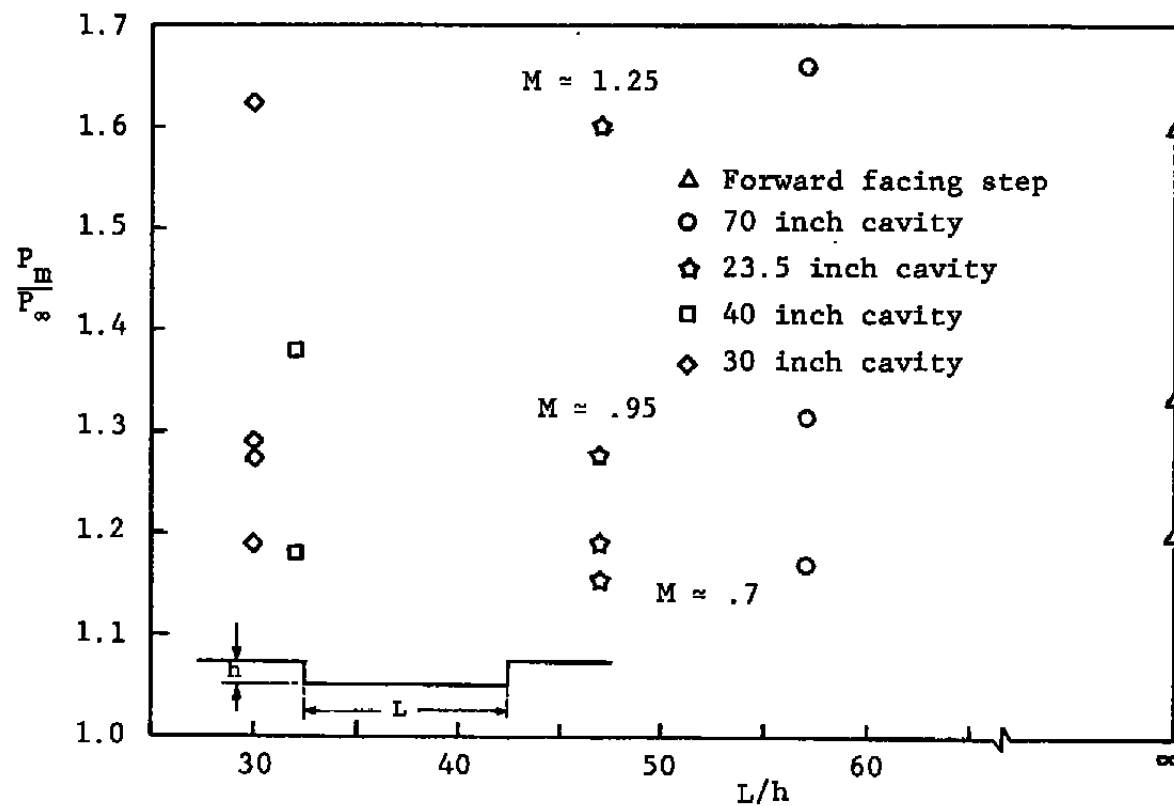


Figure 60. Variation of Peak Pressure in Flow Over Cavity Against Geometry of the Cavity.

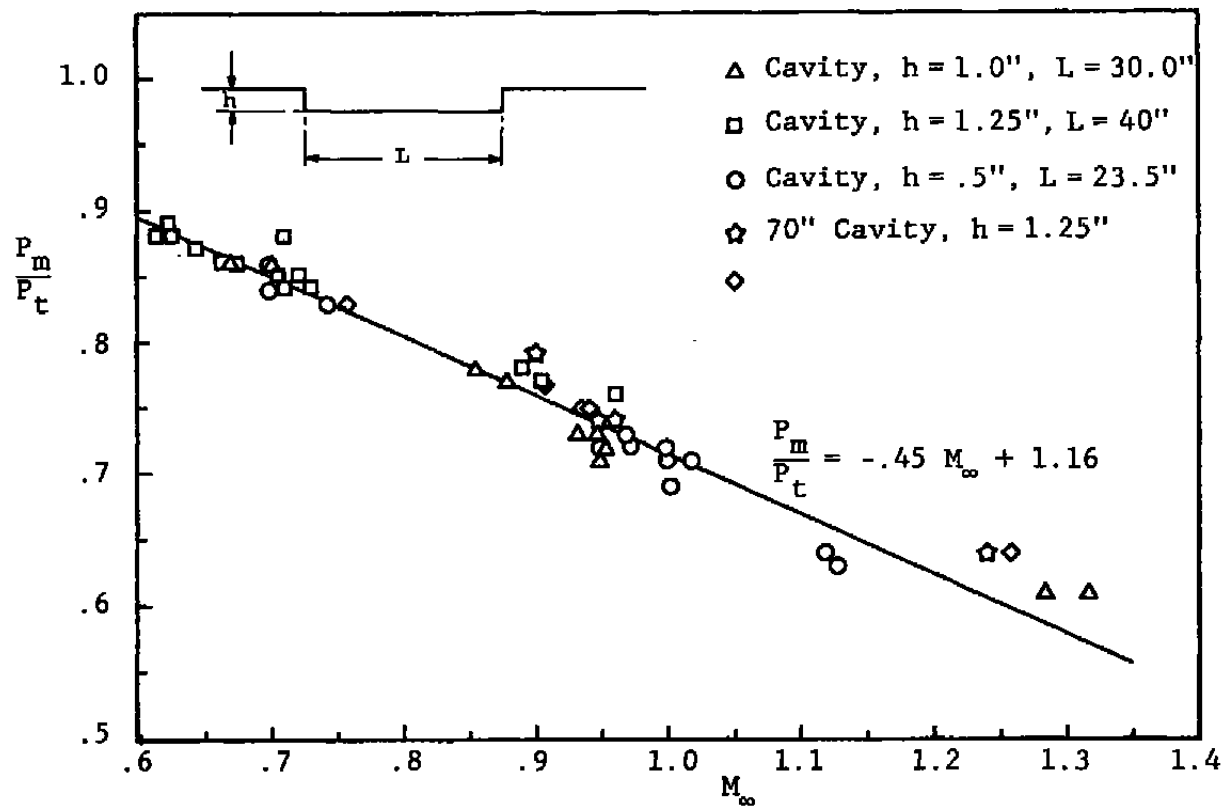


Figure 61. Variation of Maximum Pressure in Flow Over Cavity Against Free Stream Mach Number.

The only important parameter, which is drastically different between the wind tunnel test and the actual flight condition, is the Reynolds number. Generally most of the discrepancy between the wind tunnel test results and flight data are believed to be due to this Reynolds number difference. Similarity rules for extending the low Reynolds number experimental data to the desired range of flight Reynolds number are difficult to obtain.

It was discussed earlier that for the transonic flow over airfoils the viscous interaction is rather severe and very sensitive to the free stream flow changes. The separation occurring on the airfoils are of two types, Percy's types A and B, the Percy type B being the most frequent and natural process. The unsteadiness of the interaction intensifies and speeds up as soon as the separation bubble at the foot of the shock appears. Physically there is an unsteady coupling between the trailing edge separation and the recirculating region at the foot of the shock. This process is very unclear and needs to be studied in detail and fully understood before a proper Reynolds number influence can be discovered. Actual wind tunnel testing of small scale airfoil models has many limiting problems which provide extreme difficulties for any detailed study. For a small scale model the flight Reynolds number is hard to obtain, which is the original problem. For a large model, the size of the tunnel for transonic testing required to prevent wall interference increases drastically. For the type B separation the interaction between the two separation regions is sensitive to changes in free stream flow, and this wall interference could cause serious deviations in the data.

Accurate measurements are very hard to obtain in a non-uniform free stream condition. Introduction of measurement devices like a pitot probe will change the flow field as well. Lo, et al. (Ref. 31) have studied the flow over a circular bump using a laser velocimeter and pitot probe. They point out that external probes like pitot probes or rakes of different kinds may significantly disturb the flow and influence parameters like the shock location. Therefore, the data from the interaction regions needs to be obtained from non-interfering type measurements.

If one is able to simulate the above flow field (transonic flow over an airfoil) by utilizing a simple geometrical configuration, then certain testing would become much more convenient. Flow over such a model should generate the basic regions of flow present over an airfoil. Most of the emphasis must be on the boundary layer region, since this is the viscous region of interaction. A shallow

cavity appears to be qualified for such consideration. There are generally two separated regions in flow over a cavity. Depending on the length to the depth ratio of the cavity different types of interactions can be simulated. For this purpose we need to consider a cavity in the unstable region of Fig. 42, Section 5.1. In the present study this class of cavities was not studied in detail. However, from the study of stable cavity flows there is enough evidence to believe that the unstable cavity flow behaves very similarly to the flow over airfoils.

In transonic flow over an airfoil, before total separation occurs, there are three regions of interaction. First, the initial disturbance which is due to the shock wave-boundary layer interaction, accompanied by a local separation. Second, the region of attached flow between the reattachment point and the point of separation in the trailing edge region of the airfoil. Third, the separated flow in the region of the trailing edge. Similarly, in the flow over cavity, there is a recirculating region downstream of the backward-facing step, a reattached region, and a separated region in front of the forward-facing step. Changes in the free stream Mach number and Reynolds number produce the unsteady interaction which should behave in a similar manner to the unsteady process over an airfoil. Due to the shallowness of the cavity, the wind tunnel experimental setup is fairly simple and does not require complex facilities.

In Section 5, the results of the experimental study of the steady flow over different length-to-depth ratio cavities were investigated in detail. It can be easily shown that the surface pressure distribution over the attached portion of a cavity under certain conditions has a similar trend to the flow over an airfoil. The separation process depends generally on the pressure gradient and properties of the approaching boundary layer. Boundary layer properties under normal conditions depend on the Reynolds number. Therefore, if we show that the pressure distribution over a cavity and an airfoil have a similar trend, then correlation of flows at equal Reynolds numbers over cavities and airfoils will be possible.

To show the similarity of the pressure behavior, the static pressure distribution calculated by solving the viscous transonic equations numerically (Ref. 32) over a parabolic airfoil was selected.

It should be noted that this is a small disturbance approximation to the Navier-Stokes equations and includes the effect of compressive viscosity on the non-Rankine-Hugoniot regions, but does not include the boundary layer

effects. Including the boundary layer would require the solution of the full Navier-Stokes equations in the shock-boundary layer interaction region, which is very complicated.

The numerical solution of the viscous transonic equations for the unseparated flow at $M_\infty = 0.8$ over a parabolic airfoil of 15 percent thickness ratio generate a pressure distribution curve, shown in Fig. 62.

$$\tilde{C}_p = C_p \left[(\gamma + 1) M_\infty^2 \right]^{1/3} / \tau^{2/3}$$

is the transonic pressure coefficient where τ is the thickness ratio. For the same flow, if there is 15 percent trailing edge separation (Percy type B) the shock location moves upstream. This result is also shown on Fig. 62, with broken lines. The region of primary interest is between the shock and the trailing edge separation, outlined in Fig. 62. The surface pressure coefficient distribution over a 40-inch cavity of 1.25-inch depth in a flow of $M_\infty = 0.89$ and $Re_L = 24 \times 10^6$ is illustrated in Fig. 63. Depending on the location from which x is measured, we will get a very similar pattern for \tilde{C}_p for the cavity, compared to the region of interest over the airfoil, Fig. 64. Figures 65 and 66 show similar \tilde{C}_p plots for a few other cavities, for the purpose of presenting similar existing trends.

In the numerical calculations used above, the location of trailing edge separation has been initially fixed.

Also, while trying to compare the cavity and airfoil pressure fields, the effect of the curvature on the airfoil needs to be considered. However, here the idea is to show the general similarity which promises the possibility of a complete correlation between these two flow fields. An iterative scheme could be established between the experimental cavity results and the theoretical calculations to obtain realistic solutions to the transonic flow over airfoils, using the idea of this similar behavior. But, since the boundary layer has not been taken into account in the numerical calculations, the shock-boundary layer interaction region would not be correlated in this process and this region needs to be considered separately.

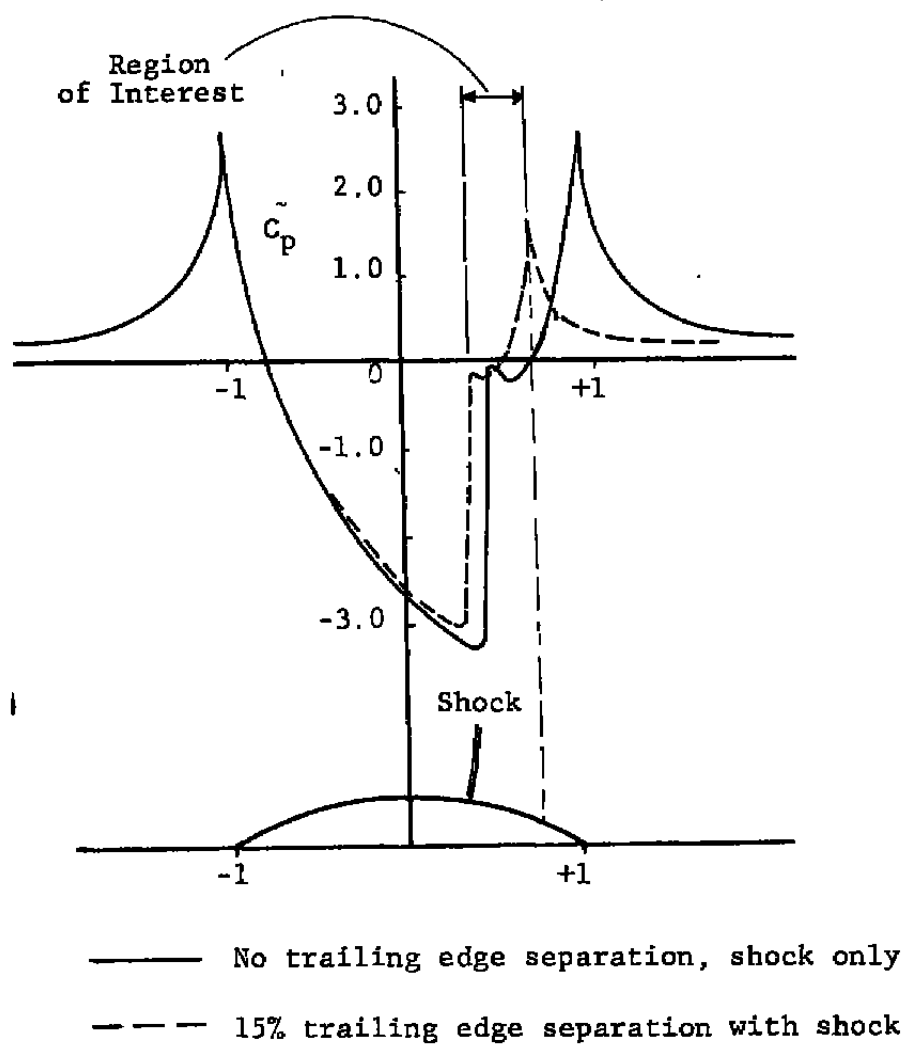


Figure 62. Numerical Result of $M_\infty = 0.8$ Flow Over a 15% Parabolic Airfoil.

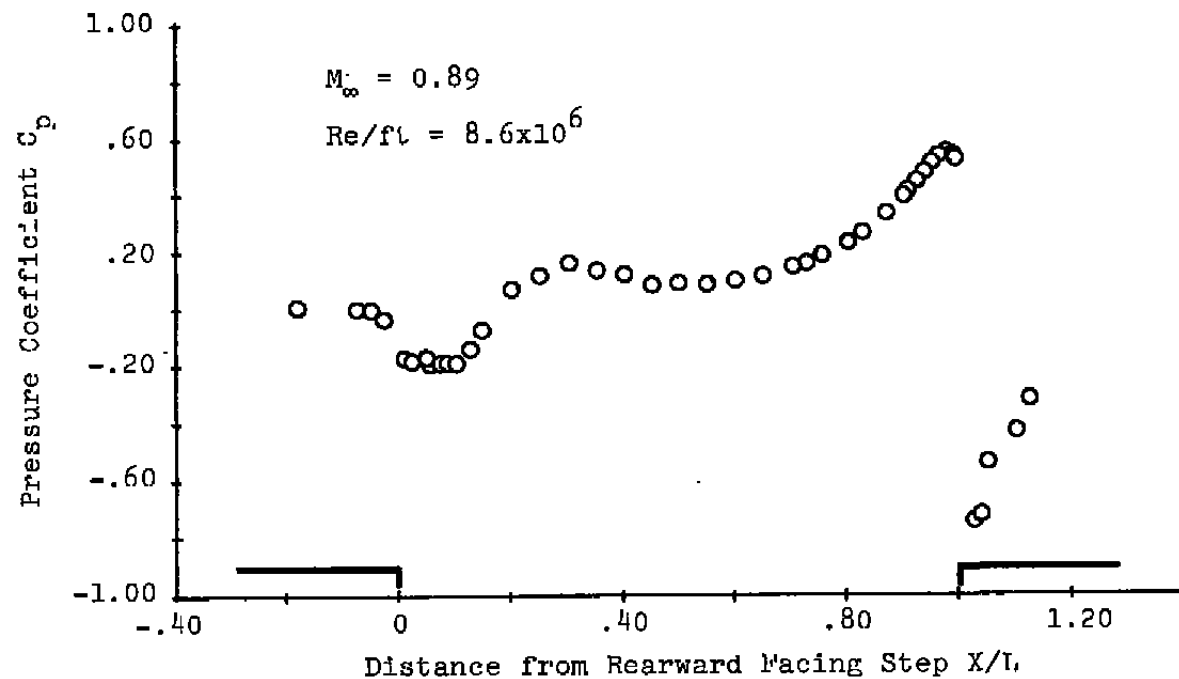


Figure 63. Surface Pressure Distribution Over a 40-Inch Cavity.

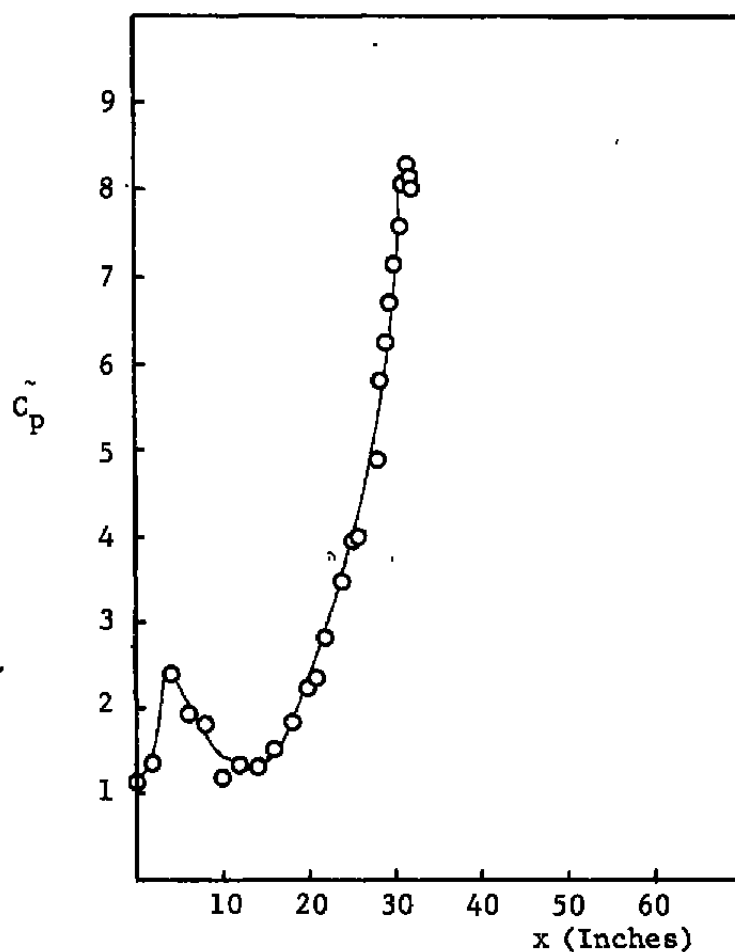


Figure 64. \tilde{C}_p Plot Obtained from Figure 63 Which Shows Similar Trend With the Region of Interest of Figure 62.

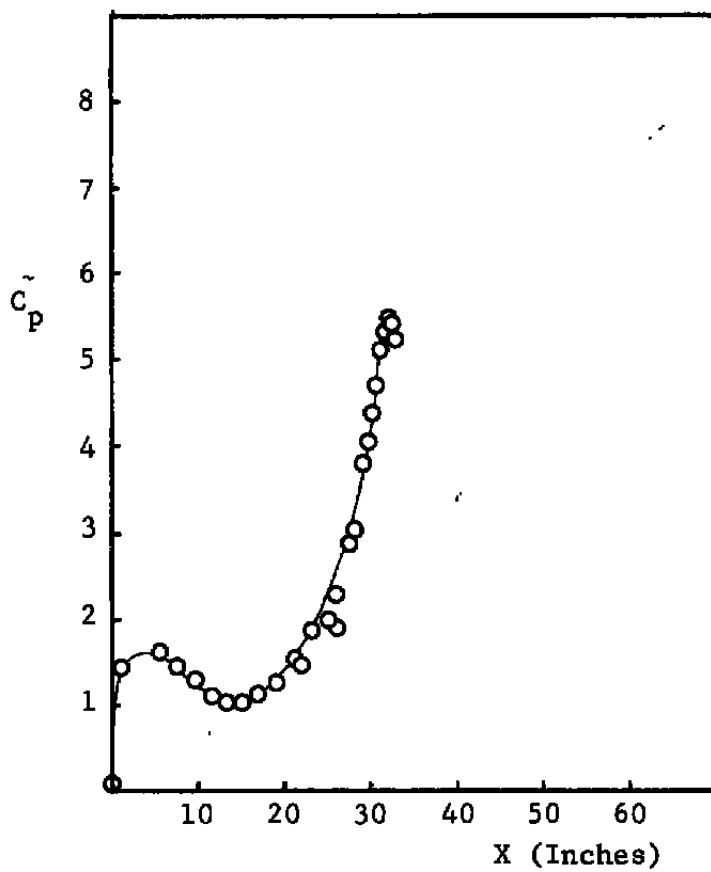


Figure 65. \tilde{C}_p Plot for a 40-Inch Cavity
in Free Stream $M_\infty = .718$.

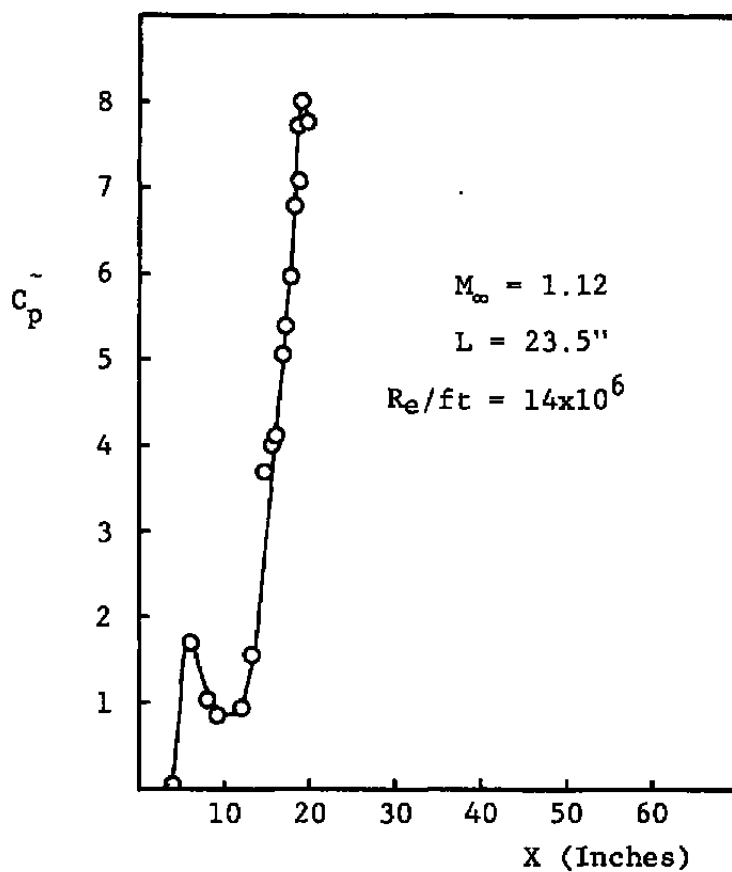


Figure 66. \tilde{C}_p Plot for a 23.5-Inch Cavity in Free Stream $M_\infty = 1.12$.

6.0 TURBULENT BOUNDARY LAYER

The main purpose of this study has been to investigate the transonic flow behavior in the presence of adverse pressure gradients with upstream disturbances of different nature. As noted earlier, the emphasis has been on the overall physical parameters and not on the microscopical structure of the fluid behavior. The boundary layer in all of the experiments of this investigation was completely turbulent. Boundary layer measurements were performed during the course of the main experiments to provide further detailed insight into the flow process along with the other parameters that were measured. Due to the impossibility of eliminating all probe interference, no velocity profile measurements were made for some of the experiments. The measurement technique and data reduction technique were explained in Section 2.

The original theory of the boundary layer, as developed by Prandtl (1904), is not capable of handling the calculations involved for a flow with adverse pressure gradients. The major conflicting assumptions are that the transverse pressure gradient can be neglected and that the longitudinal pressure distribution can be assumed to be given by the inviscid flow theory. Recent experimental and theoretical works (Refs. 33, 34, 35, 36) have shown that the transverse variation of pressure needs to be included in separated flow regions.

In the present study, transverse pressure variations in regions of adverse pressure gradients and in the separated region were experimentally measured. These measurements were done using the traversing cone probe described in Section 2. Transverse pressure measured 3 inches upstream of a 25 degree ramp-compression-corner with and without an upstream disturbance are compared in Fig. 67. The moderate transverse pressure decrease was expected and the upstream disturbance increases the deviation of boundary layer flow from an equilibrium one. Since a large curvature of the streamlines is required for a large transverse pressure gradient, and since the streamlines must approach straight lines in the immediate vicinity of the straight wall, it follows that only in the outer part of the boundary layer is the streamline curvature large, near flow separation, and the turbulent boundary layer equations are locally questionable since they neglect transverse pressure variations.

Some boundary layer measurements for the flow fields discussed in the section on the flow over ramps are shown in

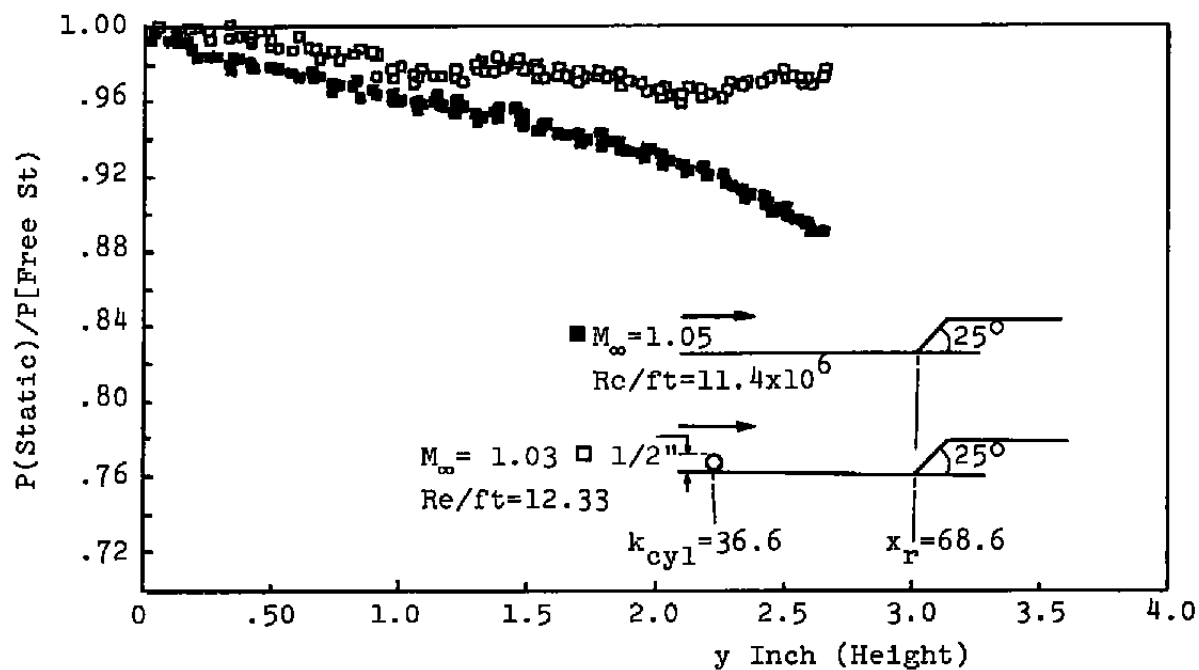


Figure 67. Comparison of Transverse Pressure Gradient for the Shown Flow Conditions.

Figs. 68, 69, 70 and 71. The results are very similar to those found for the flow over a shallow cavity (Ref. 26). All these velocity profiles have been measured in the adverse pressure gradient region 2.8 inches upstream of the ramps. The conclusions drawn from these velocity profiles are similar to those of the pressure studies in the flow over ramp section of this work. The boundary layer thickness δ and profile wake amplitude π were increased and the skin friction coefficient C_f decreased, compared to a flat plate profile, for the ramp without an upstream disturbance. In comparing the profile for the flow over a ramp with no upstream disturbance to that with disturbance, the disturbed profiles show an increase in δ and π and a further decrease in C_f . The effect of disturbance size on the boundary layer profile is shown in Figs. 68, 69 and 71.

6.1 LAW OF THE WALL AND LAW OF THE WAKE

An analytical representation of the turbulent boundary layer is very desirable. There have been many attempts, by several investigators, to come up with a similar representation for the turbulent boundary layer profile. The development of law of the wall was originally based on the Prandtl mixing length theory (1925). Prandtl assumed a correlation of the turbulent shear stresses to the local mean velocity fluctuations in the form

$$\tau_t = -\rho \overline{u'v'} \approx \rho \ell^2 \left\{ \frac{\partial \bar{u}}{\partial y} \right\}^2$$

Further developments in this direction were achieved by von Karman (1930), Nikuradse (1930), Betz (1931), Taylor (1932), Millikan (1938), Schultz-Grunow (1940), Hamel (1943), Ludweig and Tillman (1949), Reichardt (1951), Laufer (1951), Clauser (1954, 1956), Gales (1955), Van-Driest (1956), Spalding (1961), Keinstein (1967), and others.

The formulation of law of the wall was based on pipe flow observations and its form was suggested by Ludweig and Tillman (1949) in the form

$$\frac{u}{u_\tau} = f\left(\frac{yu_\tau}{\nu}\right)$$

and was believed to be a universal similarity law for turbulent flow over a smooth surface. Later, in 1956, Coles suggested the formulation in the form

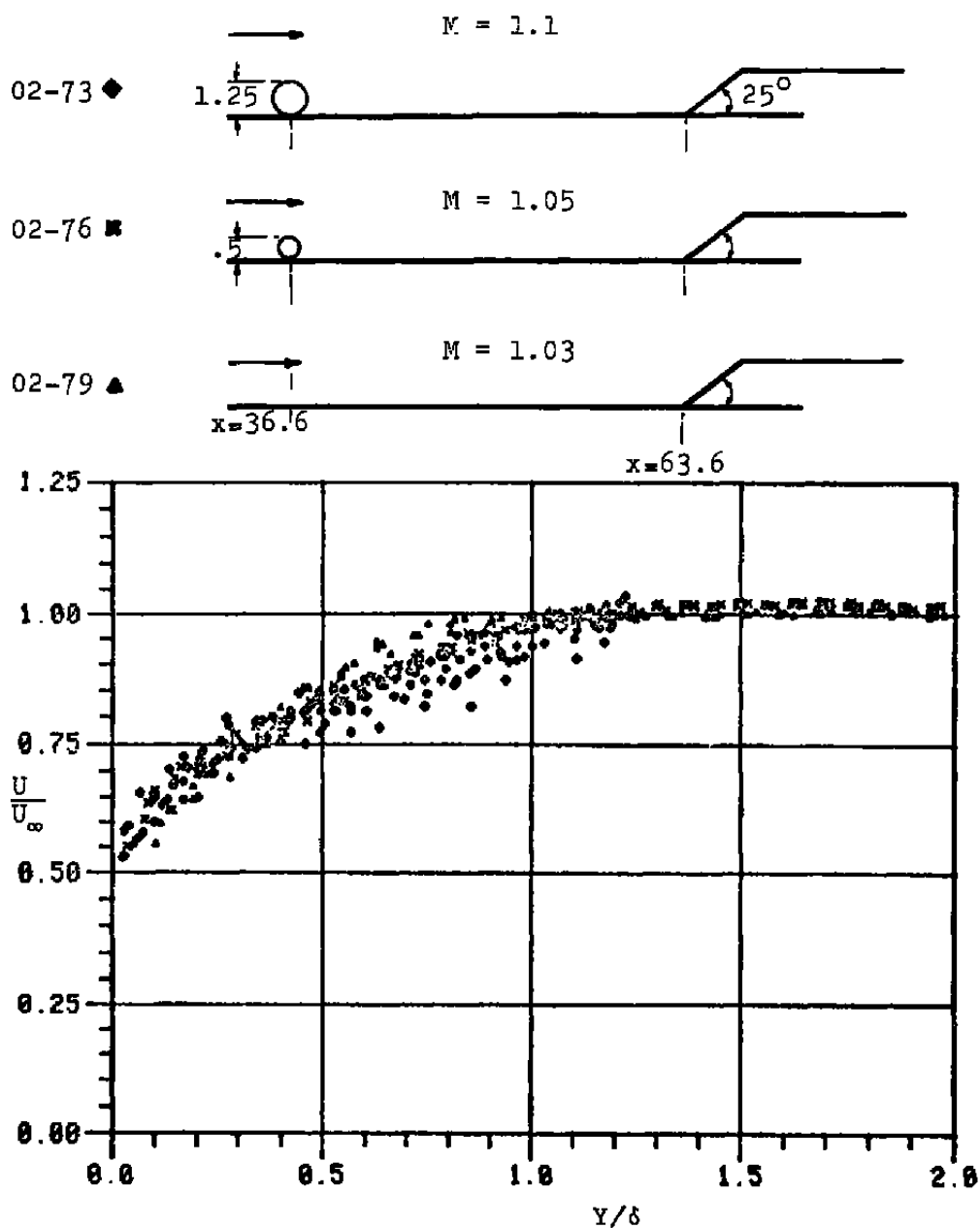


Figure 68. Comparison of Velocity Profiles for the Above Flow Conditions.

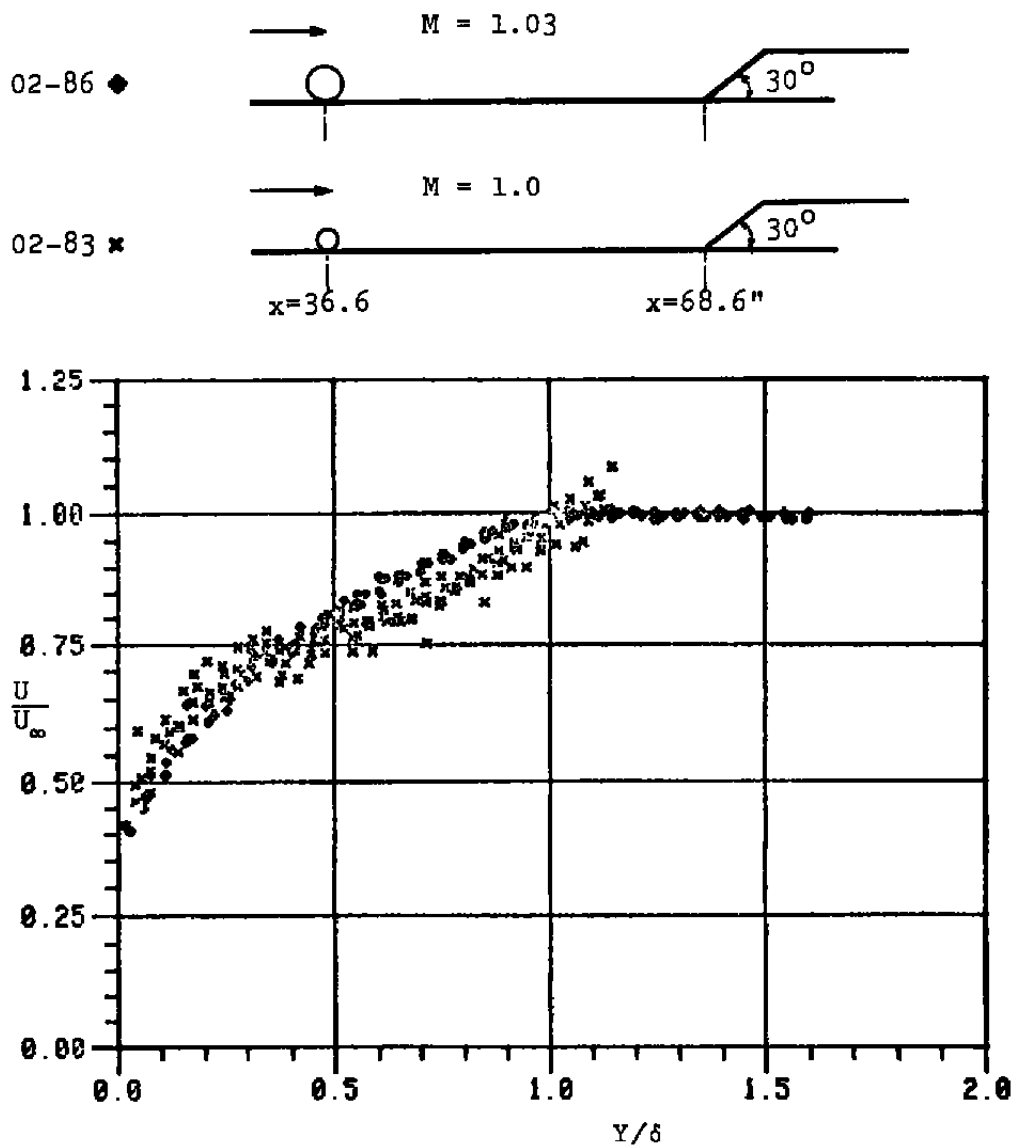


Figure 69. Comparison of Upstream Disturbance Effects on the Velocity Profile 3 Inches in Front of the 25 Degree Ramp.

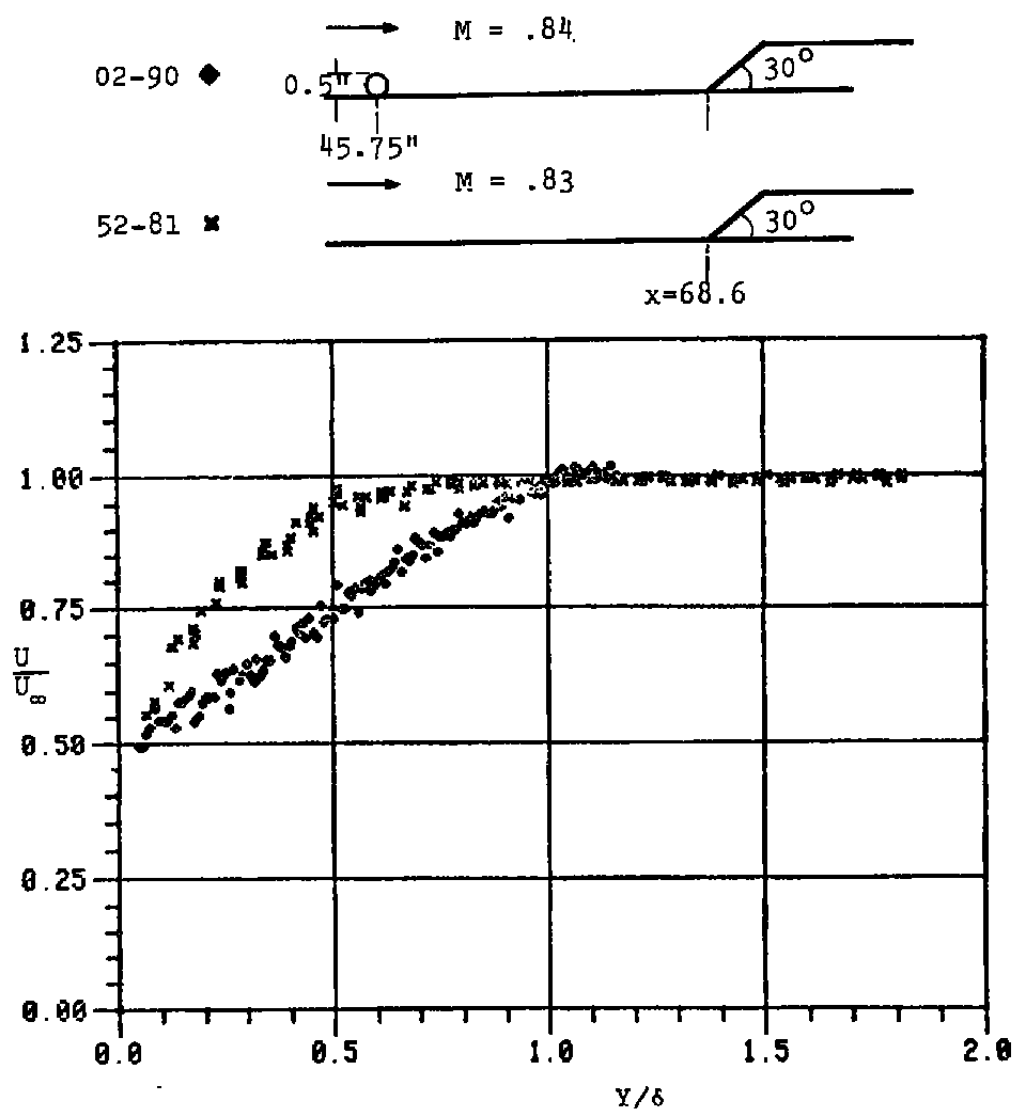


Figure 70. The Effect of Upstream Disturbance on the Velocity Profile 3 Inches in Front of the 30 Degree Ramp.

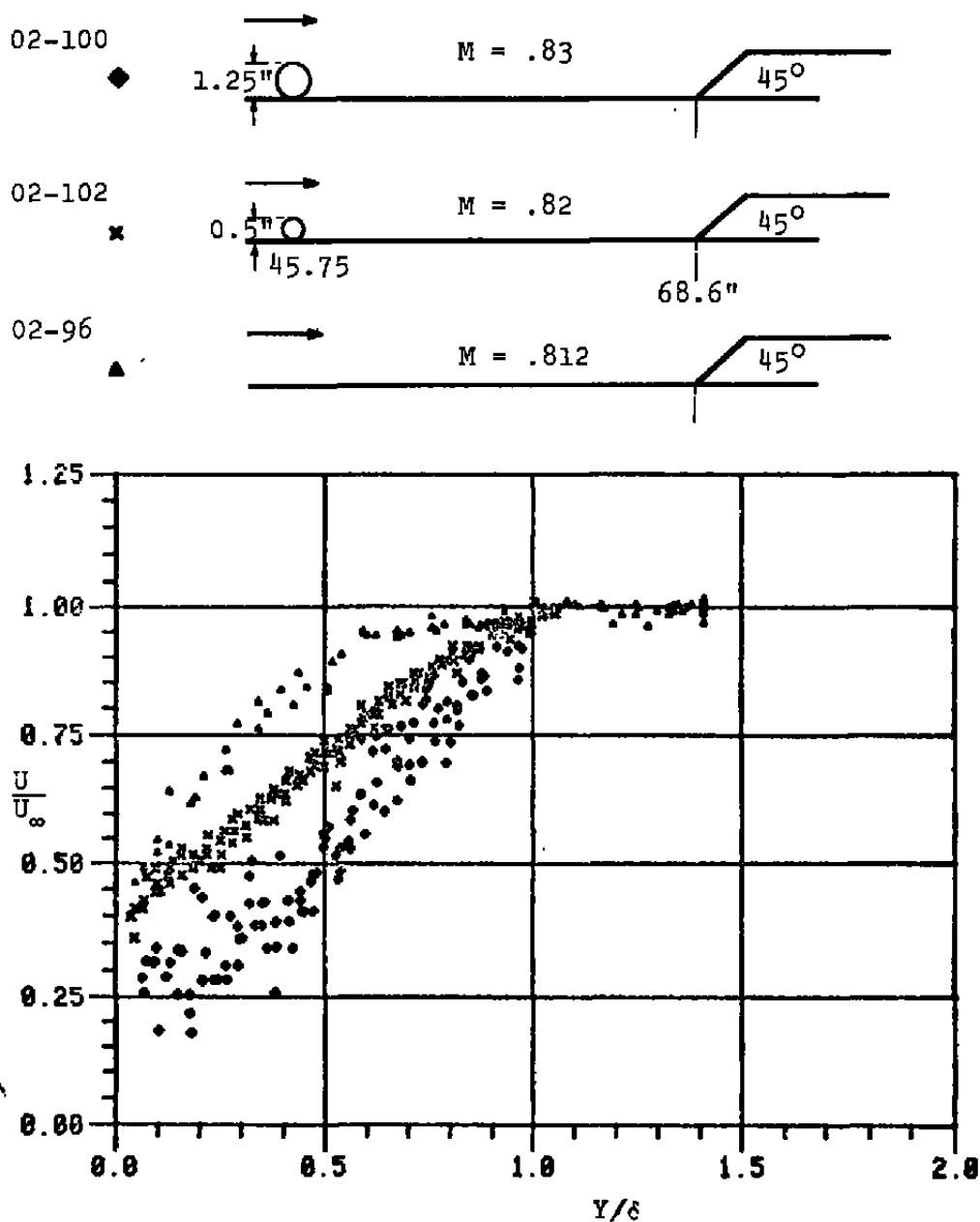


Figure 71. Comparison of Upstream Disturbance Effects on the Velocity Profile 3 Inches in Front of the 45 Degree Ramp.

$$\frac{u}{u_\tau} = f\left(\frac{yu_\tau}{\nu}\right) + \frac{\pi}{k} w\left(\frac{y}{\delta}\right)$$

as the similar representation of turbulent velocity profiles, where π is a profile parameter independent of the spatial coordinates x and y . Finally the form

$$\frac{u}{u_\tau} = \frac{1}{k} \ln \frac{yu_\tau}{\nu} + B + \frac{\pi}{k} \left[1 - \cos \frac{\pi y}{\delta} \right]$$

was established by Coles for a flat plate incompressible turbulent boundary layer with the universal constants $k = 0.41$ and $B = 5.0$.

Van-Driest in 1951 introduced the "effective-velocity" approach to extend this incompressible relation to compressible boundary layers. He achieved this by a modification of the Prandtl mixing length theory to account for variable density.

Since the introduction of the law of the wall and law of the wake several authors have attempted to develop more complete forms of similarity expressions for the turbulent boundary layer. These attempts have been made due to the fact that the law of the wall and wake is not exact and rather approximate. Depending on the conditions, the deviation between this expression and experimental results can be very large. The conditions where the law of the wall and the law of the wake faces problems are: (1) in regions of strong pressure gradients, (2) very close to the wall where $y^+ < 50$, (3) at the edge of the boundary layer $y \approx \delta$. Against all the difficulties related to the law of the wall and law of the wake it is probably the most frequently used form of representation of an equilibrium boundary layer. A criteria for equilibrium was given by Clauser (1954). According to his criteria equilibrium turbulent flow occurs when the boundary layer has similar trends when plotted in the $(u-u_\infty/u^* \text{ vs. } y/\delta)$ coordinates. Here u^* is the same as u_τ , the friction velocity used in the law of the wall and law of the wake.

In the present experiments, although most of the boundary layer profiles were measured in the presence of large pressure gradients, they have been plotted in the u^+ and y^+ coordinates for general comparison with the flat plate boundary layer. To obtain u^+ and y^+ from u and y obtained from the measured data, the following method was

used. Known were: u , y , δ , δ^* , and H . These values were calculated during the data reduction process for each profile. The unknowns were u_τ , the friction velocity, and the $\bar{\pi}$ profile parameter. The law of the wall and law of the wake was used in the form

$$\frac{u}{u_\tau} = \frac{1}{k} \ln \left(\frac{yu_\tau}{\nu} \right) + B + \frac{\bar{\pi}}{k} \left(1 - \cos \frac{\bar{\pi}y}{\delta} \right) \quad (10)$$

with $k = 0.41$ and $B = 5.0$ (Coles constants).

The displacement thickness can be expressed as

$$\frac{\delta^*}{\delta} \frac{u_\infty}{u_\tau} = \int_0^\infty \left(\frac{u_\infty - u}{u_\tau} \right) d \left(\frac{y}{\delta} \right) \quad (11)$$

Substitution of Equation (10) into (11) and integration results in

$$k \frac{\delta^*}{\delta} \frac{u_\infty}{u_\tau} = 1 + \bar{\pi} \quad (12)$$

From Equation (10) at $y = \delta$ we have

$$\frac{u_\infty}{u_\tau} = \frac{1}{k} \ln \frac{u_\tau \delta}{\nu} + B + \frac{2\bar{\pi}}{k} \quad (13)$$

From Equations (12) and (13) the values of u_τ and $\bar{\pi}$ can be calculated for a given velocity profile. Since the present work was for compressible flow the Van-Driest "equilibrium velocity" concept was used to transform the incompressible form of Equation (10) into the compressible form. The equation was transformed using the following equations:

$$u_{eq} = \frac{u_\infty}{a} \sin^{-1} \left[a \frac{u}{u_\infty} \right]$$

where

$$a = \left[\frac{(\gamma-1)M_\infty^2}{2 + (\gamma-1)M_\infty^2} \right]^{1/2}$$

for an adiabatic wall.

Figures 72 and 73 show a typical comparison of the velocity profiles and their law of the wall and wake presentation, respectively. The disturbed flow has a fuller profile close to the wall.

6.2 NORMAL SHOCK-BOUNDARY LAYER INTERACTION

Very frequently a nearly normal shock is formed in the transonic flow over a body, as in Fig. 74. In an inviscid flow of upstream Mach number M_∞ , the pressure behind the shock will increase according to the normal shock relationship. The interaction process between the shock wave and the turbulent boundary layer is more involved. In inviscid flow the pressure will increase discontinuously across the shock, Fig. 75. But, real flow cannot permit a discontinuous pressure rise, and therefore near the wall the shock is replaced by a band of compression waves, Fig. 75. The pressure rise in this case occurs typically in a distance of three to five boundary layer thicknesses. Therefore, the pressure gradient appearing at the wall is determined by the strength of the shock and the properties of the boundary layer.

The pressure rise across the shock thickens the boundary layer downstream of the shock. Under certain conditions this pressure rise leads to the creation of a separated region at the foot of the shock, Fig. 76. However, since the separation is often caused by the pressure increase, it is possible that there exists a critical pressure rise which is just strong enough to cause separation.

There have been many studies on the shock-boundary layer interaction, most of which have investigated the interaction between an oblique shock and the turbulent boundary layer. There have also been investigations centered on the transonic flow and near normal shock interactions. The fact that the present study was performed at very high Reynolds numbers which are close to the flight Reynolds numbers makes this work of interest for practical applications.

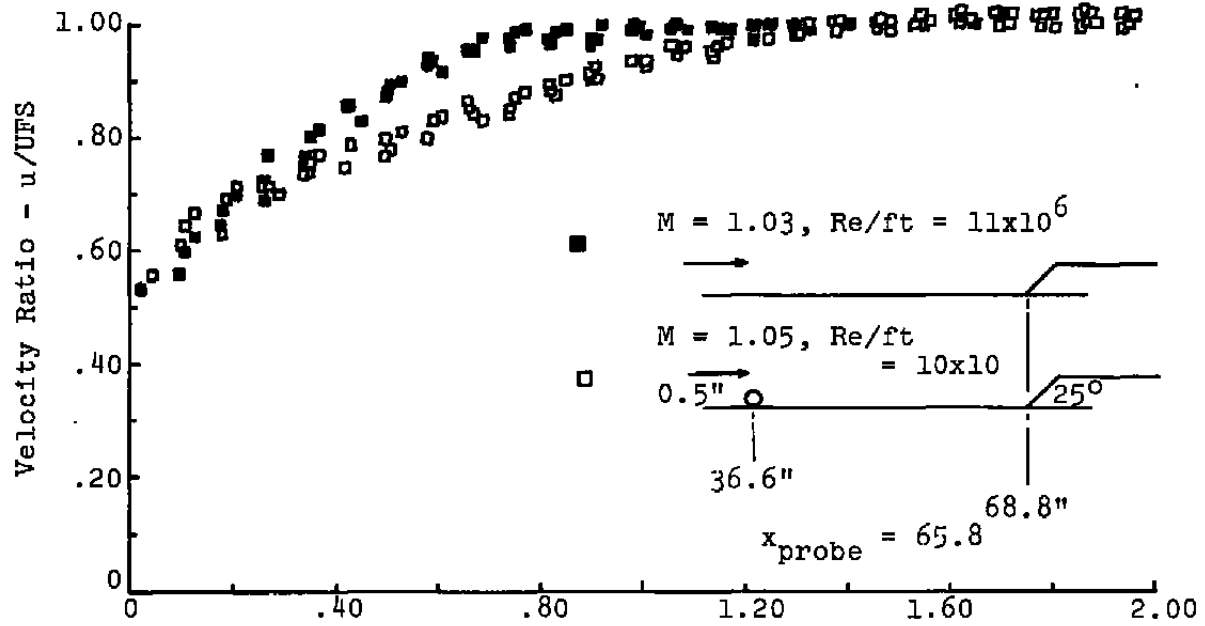


Figure 72. Comparison of Velocity Profiles for the Flow Field Shown.

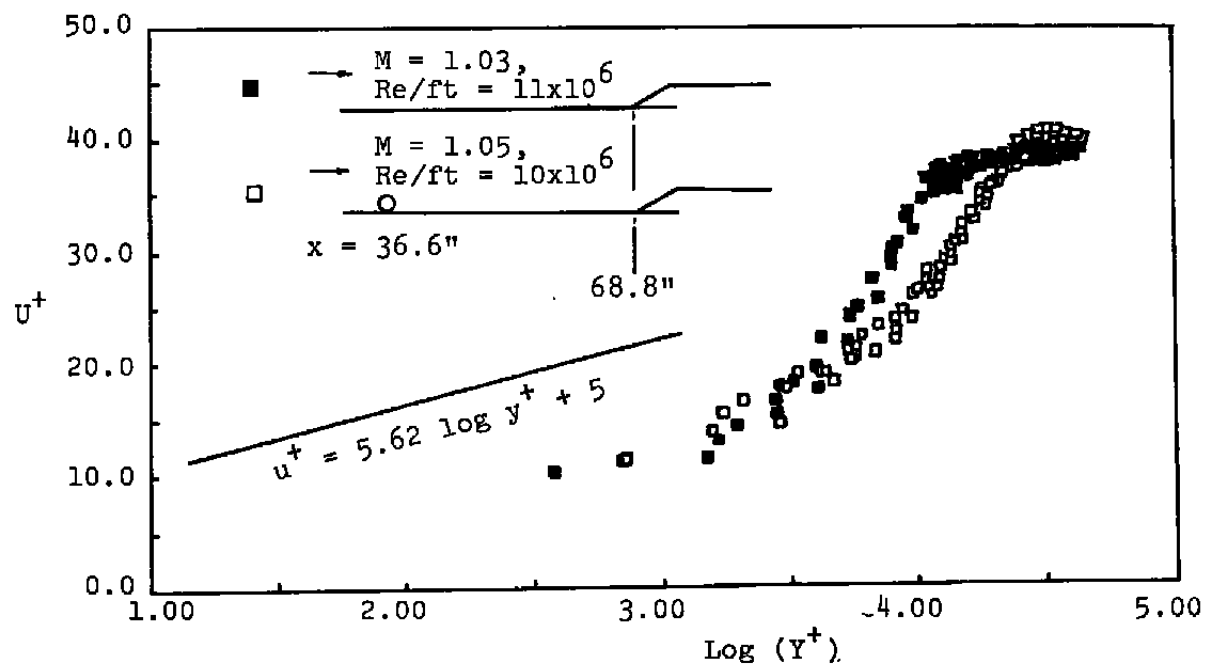
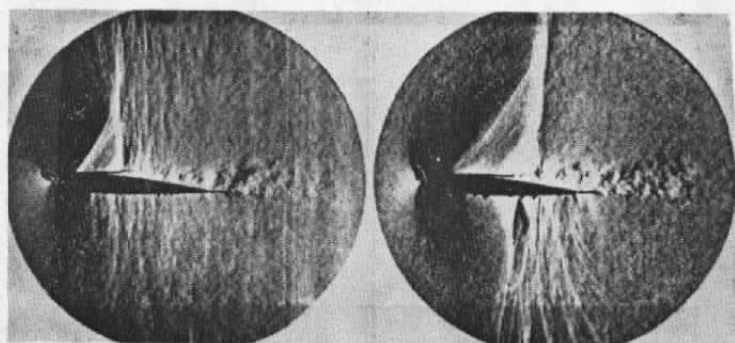


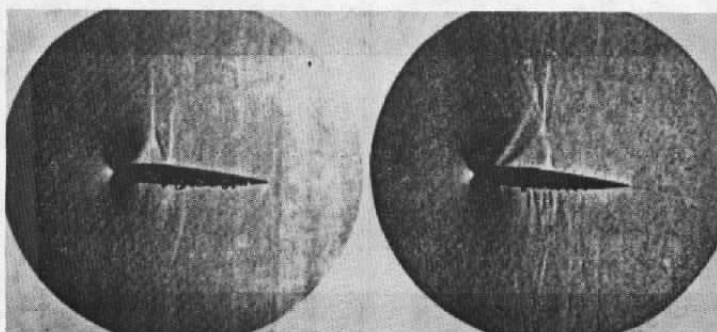
Figure 73. Comparison of the Law of the Wall and Law of the Wake for Profiles Shown on Figure 71.



$M_{\infty} = .78$

$M_{\infty} = .87$

$(\alpha = 2^{\circ})$



$M_{\infty} = .78$

$M_{\infty} = .86$

$(\alpha = 4^{\circ})$

Figure 74. Appearance of Normal Shock Over NACA 0012 Airfoils in Transonic Flow.

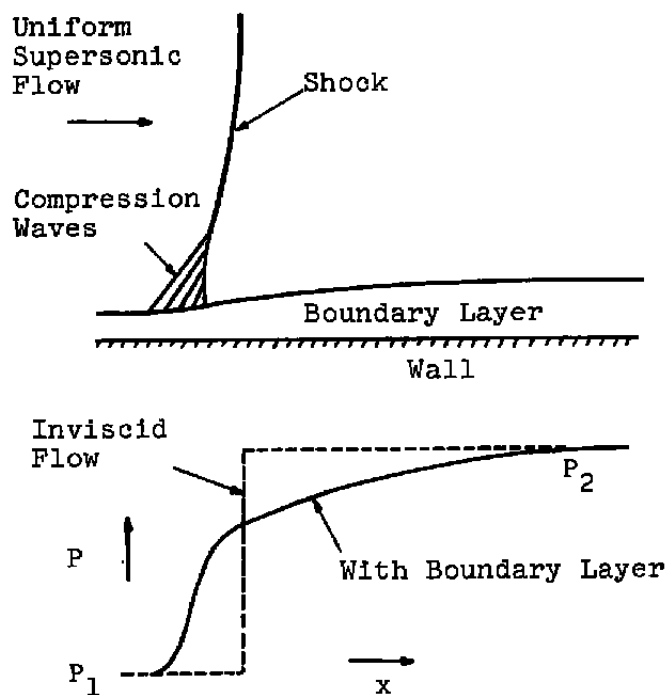


Figure 75. Flow Pattern and Pressure Distribution When the Shock is Not Strong Enough to Cause Much Separation.

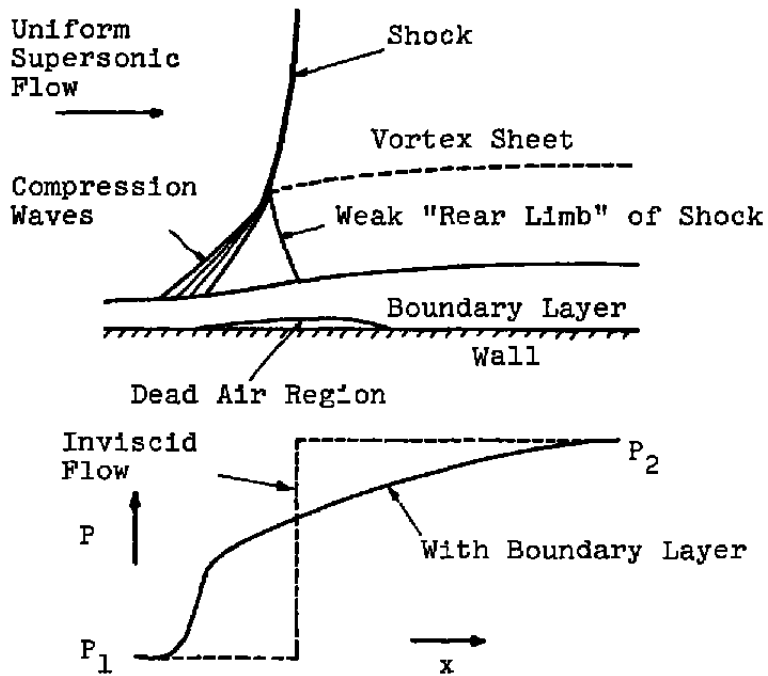


Figure 76. Flow Pattern and Pressure Distribution With a Strong Shock.

This study was performed in the UTSI transonic wind tunnel, with the normal shock produced by a shock generator placed inside the tunnel. One important part of this experiment was to design the shock holder. This part was done by Dowgwillo and more information about the shock holder is given in Chapter 2.0 .

6.2.1 Experimental Setup and Results

The shock holder was installed inside the tunnel at the station $x = 50.5$ inches from leading edge, 8.19 inches above the flat floor plate, producing a detached nearly normal shock wave. For this particular geometry of the shock holder, this location was experimentally shown to produce the least interference with the rest of the interacting zone. However, some unsteadiness was introduced into the flow field due to the circular trailing edge of the shock holder.

Flow visualization techniques including surface oil flow, kerosene and graphite, and static and motion Schlieren pictures, were used to record the flow interaction details. When separation was incipient it was difficult to detect. Incipient separation does not have any important practical effect. However, it is usually of considerable interest to determine the incipient separation conditions because it represents the lower limit of the process of separation. There are several methods for separation detection. A very exact but difficult method is to find the location of zero skin friction, since skin friction vanishes at the onset of separation. However, this method is very difficult experimentally to be performed, because it requires skin friction gages which are very sensitive and can accurately measure vanishingly small forces. Surface oil flow, which is used to detect separation, is not generally very accurate because the very small momentum contained in the tiny bubble at the start of separation could not move the viscous oil. Therefore, a mixture of kerosene and graphite will possibly be more accurate in the detection of incipient separation since it has very little viscosity. The use of a certain value of the shape factor H as a separation prediction criterion for the normal shock case is not very accurate. Gadd (Ref. 37) used the $C_f = 0$ location, and his formulation for calculating C_f is fairly accurate.

The existence of separation was supposed to be detected by one of the above techniques. However, regular surface oil flow did not give any indication of separation. The kerosene and graphite technique showed many spanwise accumulation lines which originally were hard to interpret, since

there was no separation detected from the static Schlieren pictures. Gadd (Refs. 37 and 38) predicted separation at $M \approx 1.2$. Alber, et al. (Ref. 39) through experimental measurements observed that separation appeared at the foot of the shock when the local Mach number reached 1.34. This figure was observed for the flow over a circular arc profile. Alber, et al., observed that trailing edge separation appeared at much lower Mach numbers and actually at $M \approx 1.34$ a separation region appeared at the foot of the shock. Fast motion Schlieren pictures taken at a rate of 2000 to 5000 frames per second showed an unsteady pattern in the shock interaction region. The normal shock was observed to be oscillating at a nearly constant frequency of 250 Hz with an amplitude of 1.03 inches in the inviscid region and 1.27 inches at the edge of the boundary layer. Figure 77 shows the shock oscillations. These Schlieren pictures were taken at a rate of nearly 3000 frames/sec. The presence of separation was not clear in these Schlieren pictures. However, due to the high Reynolds number and high turbulence level in the tunnel it was suspected that the separation region, if any, would have been too small to be detected by the oil flow techniques. Vidal, et al. (Ref. 40) also noticed the unsteadiness of the geometry of the bifurcated shock wave at the surface. He noticed as the Reynolds number increases the region of separation shrinks for a fixed free stream Mach number. Altstatt (AEDC TR-77-47) found that the shock wave was oscillating in the free stream only but not close to the wall. His shock was generated over a curved surface in a transonic wind tunnel. The oscillation of a normal detached shock due to free stream flow fluctuations is caused by the variations in the shock stand-off distance with changes in the free stream Mach number. At the same time the change in the free stream Mach number changes the strength of the shock. Therefore, the pressure rise across the shock will vary and hence the amount of boundary layer thickening will vary. Because of this the region of shock-boundary layer interaction will oscillate as well with the shock in the free stream portion of the flow.

If the free stream flow variations are such that there is a separated region at one instant and it vanishes later when flow conditions have changed, then there will also be quite extensive oscillations of the near normal shock wave. Since these oscillations are at a high frequency compared to the sampling time of the static and total pressure measurements, it would not appear in these pressure measurements and generally the mean values were measured.

The static pressure distribution on the flat plate shows (Fig. 78) that the flow accelerates downstream of the

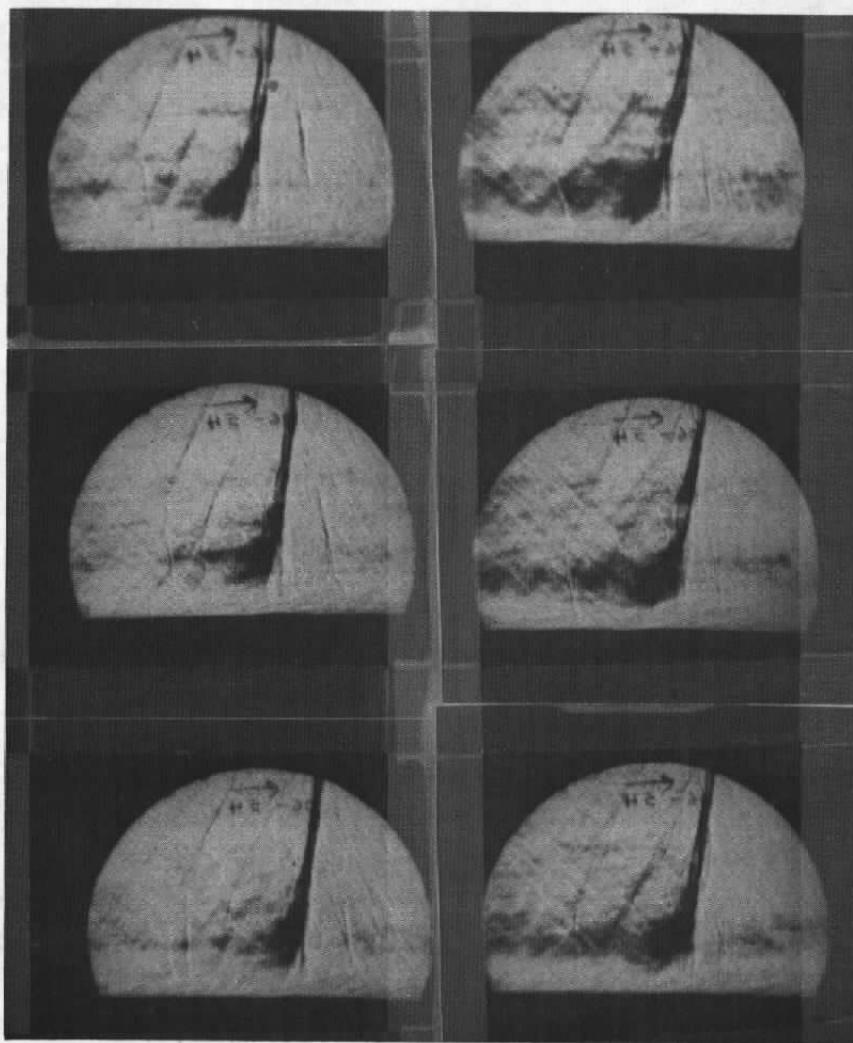


Figure 77. Shock Wave Oscillations.

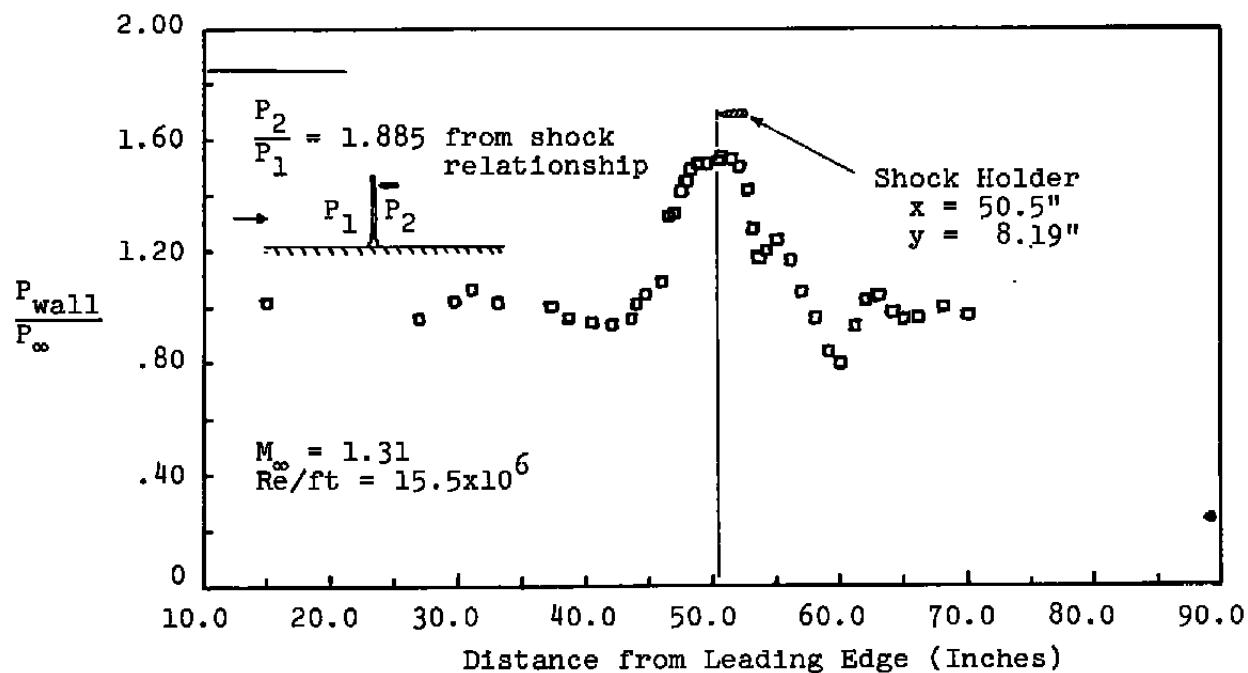


Figure 78. Static Pressure Along the Flat Plate With the Impinging Normal Shock.

shock incidence. The acceleration is possible due to the fact that the tunnel ceiling is perforated and the shock holder is very short in the flow direction. The flow does not remain choked for a long enough distance downstream. There is also the possibility of interaction between the expansion fan over the shoulder and the circular end of the shock holder and the boundary layer. There is an indication that the length of the shock holder in the direction of flow is very critical to insure a disturbance-free and choked flow. Another difficulty encountered, due to the geometry of the shock holder, was that of the generation of an unsteady flow field from the interaction between the oscillating base flow of the shock holder and the main flow stream. In this range of Mach numbers, the flow field is very sensitive to perturbations introduced into the main flow. However, the high frequency and large amplitude of the shock wave oscillations is suspected to be the combined result of the interaction between the unsteady vortices behind the shock holder and the nonuniform free stream flow. Vidal, et al. (Ref. 31) used a long plate with two area changes, one of them by the use of a flap which weakened the shock and positioned the propagating shock at a fixed position. They did not observe any interaction from the trailing portion of this plate in the shock region.

The boundary layer velocity profile measured 3 inches downstream of the shock indicated a disturbed profile, but there is no indication that the flow is separated. In Fig. 79 this velocity profile is shown in comparison with a flat plate velocity profile of similar Reynolds number. These velocity profiles are also compared in the law of the wall and law of the wake coordinates in Fig. 80. The shift of the data to smaller values compared to the flat plate data on y^+ , u^+ plot is due to the favorable pressure gradient present at the location where this velocity profile was measured. As discussed earlier, this is because of the interference caused by the expansion over the shock holder. Therefore, the profile is a disturbed profile in a favorable pressure gradient.

The transverse pressure gradient was measured at the same location with the cone probe and a significant variation of pressure in the y -direction was observed (Fig. 81). At the edge of the boundary layer $dp/dy \neq 0$ because of the streamline curvature, which is due to thickening of boundary layer downstream of shock wave boundary layer interaction.

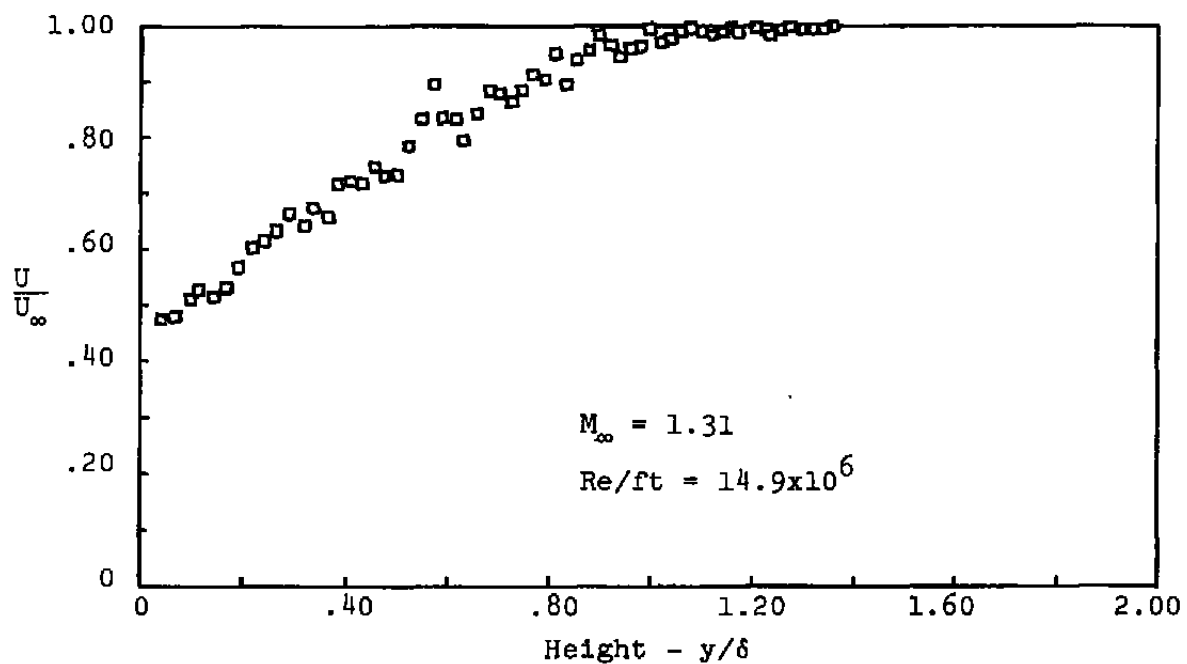


Figure 79. Velocity Profile Downstream of the Normal Shock.

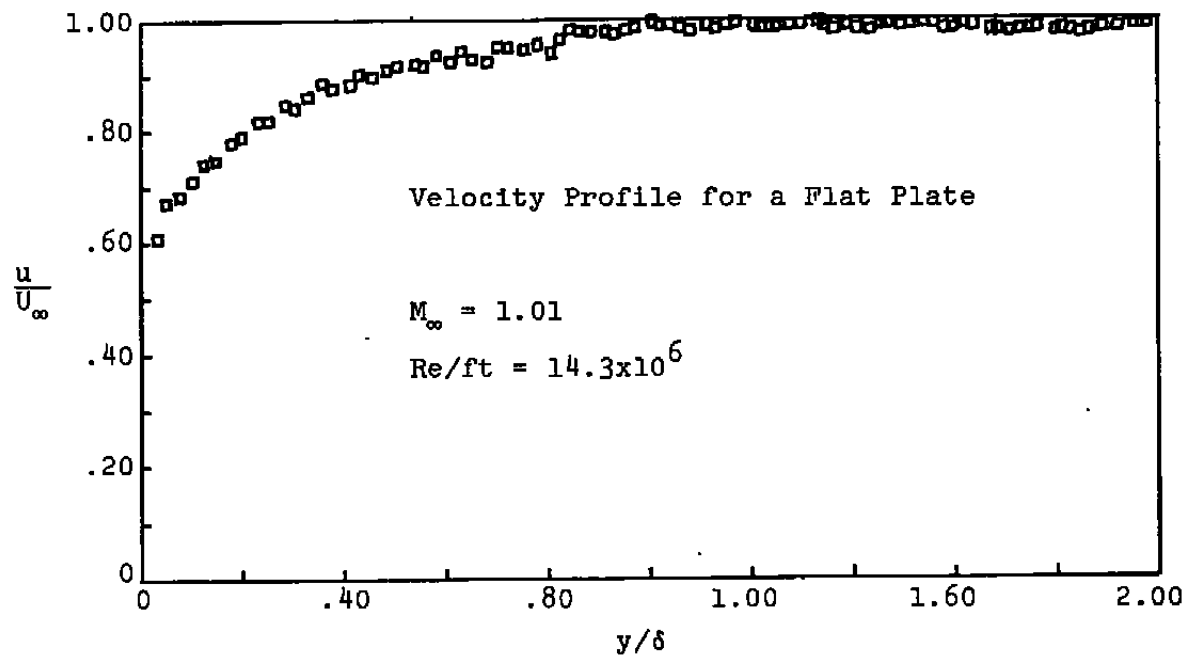


Figure 79. (Continued)

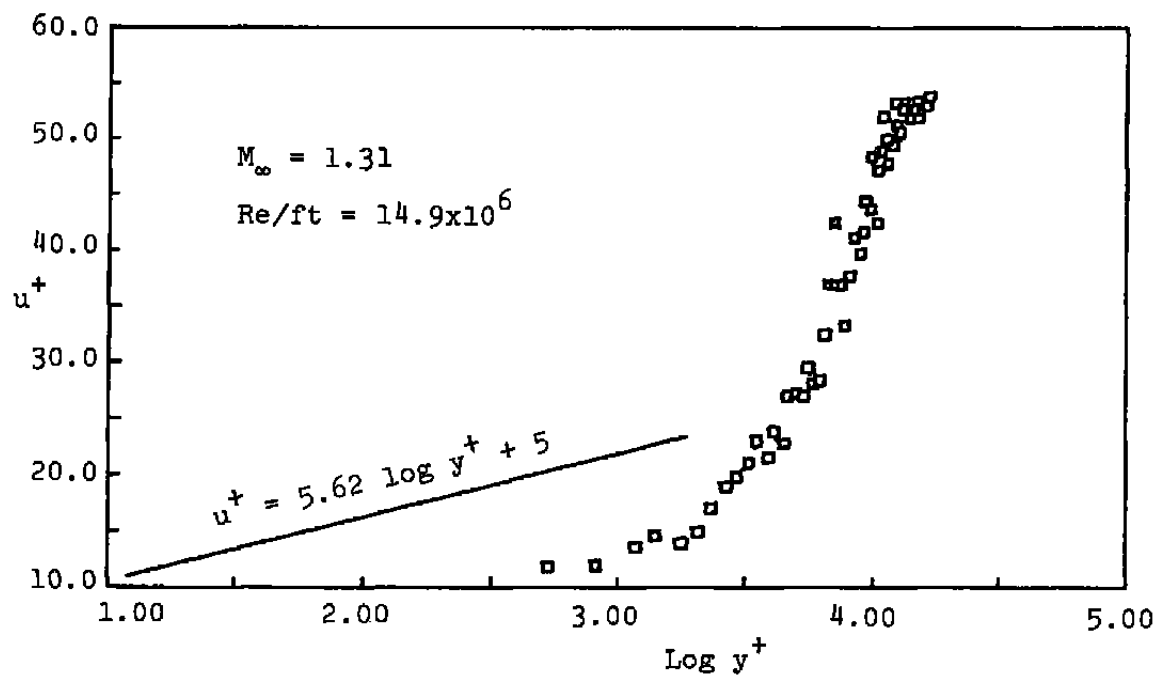


Figure 80. Plot of the Velocity Profile Downstream of the Shock in the Law of the Wall Law of the Wake Coordinate.

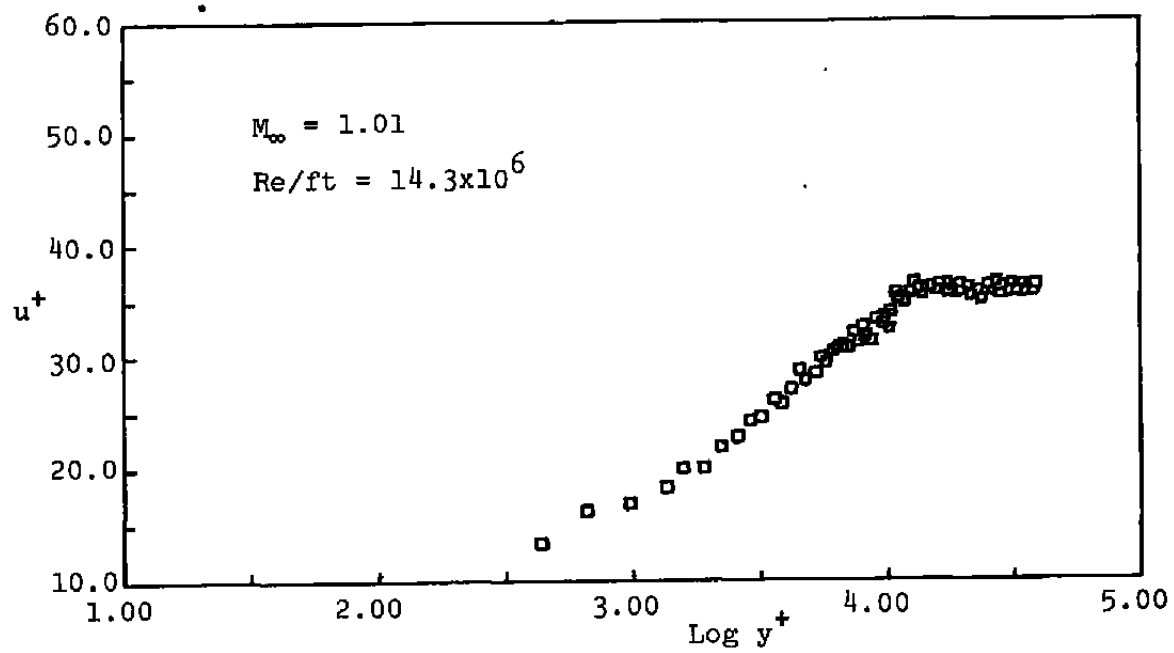


Figure 80. (Continued)

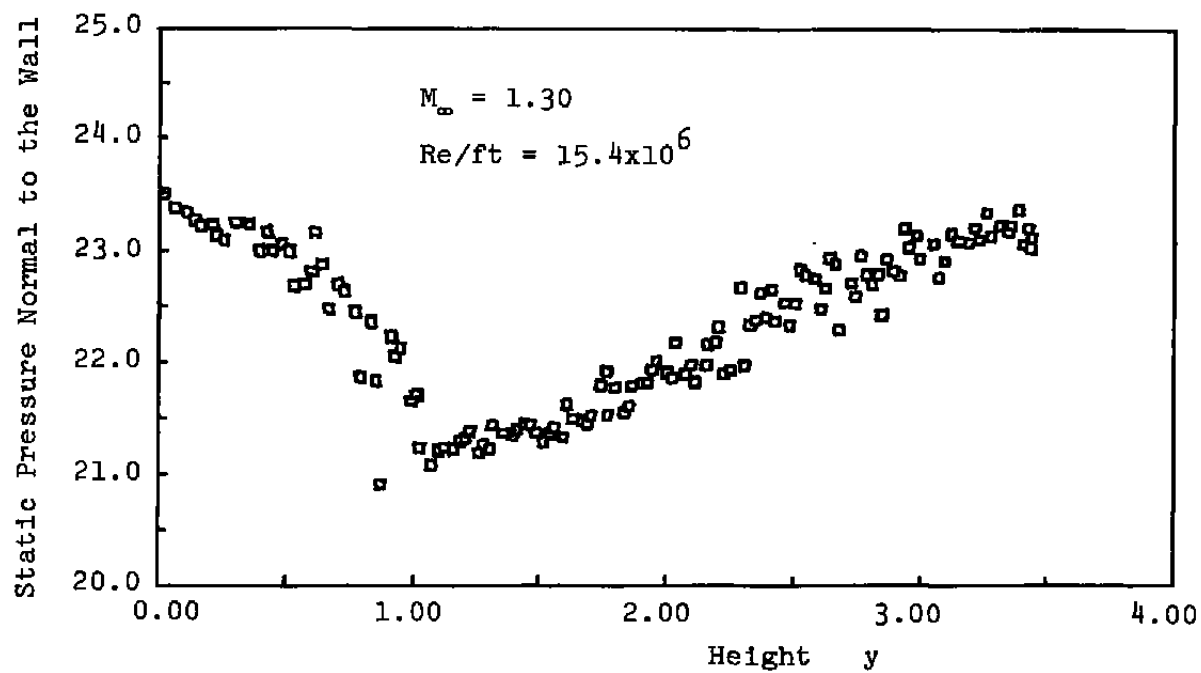


Figure 81. Transverse Pressure Immediately Downstream of the Shock.

7.0 NAVIER-STOKES SOLUTIONS FOR LONG CAVITIES

One of the major concerns in dealing with high Reynolds number transonic flows is the viscous-inviscid interaction near separated regions. If the separation is induced by a shock it adds an additional complication.

In the last few years computational fluid dynamics has advanced to a point where we can compute the solutions of full Navier-Stokes equations for two-dimensional geometries at high Reynolds numbers. Turbulence is introduced in the calculations through eddy viscosity terms (algebraic models). Solutions for transonic flows over arbitrary airfoil geometries are very good when the separated regions over the airfoils are relatively small. Shock-wave boundary layer interaction can be computed reasonably well under those conditions. We give a brief review of a solution technique -- an explicit-implicit time dependent algorithm due to McCormack (Ref. 41) and his associates (Refs. 42, 43, 44).

7.1 A FINITE DIFFERENCE ALGORITHM FOR NAVIER-STOKES EQUATIONS

The compressible Navier-Stokes equations for a two-dimensional problem can be written in conservation form as

$$\frac{\partial U}{\partial t} + \frac{\partial F}{\partial x} + \frac{\partial G}{\partial y} = 0 \quad (14)$$

where

$$U = \begin{bmatrix} \rho \\ \rho u \\ \rho v \\ e \end{bmatrix}, \quad F = \begin{bmatrix} \rho u \\ \rho u^2 + p + \sigma_x \\ \rho uv + \tau_{xy} \\ (e + p + \sigma_x)u + \tau_{yx}v + k\frac{\partial T}{\partial x} \end{bmatrix}$$

$$G = \begin{bmatrix} \rho v \\ \rho vu + \tau_{yx} \\ \rho v^2 + p + \sigma_y \\ (e + p + \sigma)v + \tau_{yy}u + k\frac{\partial T}{\partial y} \end{bmatrix} \quad (15)$$

$$\begin{aligned}
\sigma_x &= -\lambda \left(\frac{\partial u}{\partial x} + \frac{\partial v}{\partial y} \right) - 2\mu \frac{\partial u}{\partial x} \\
\sigma_y &= -\lambda \left(\frac{\partial u}{\partial x} + \frac{\partial v}{\partial y} \right) - 2\mu \frac{\partial v}{\partial y} \\
\tau_{yx} = \tau_{xy} &= -\mu \left(\frac{\partial u}{\partial y} + \frac{\partial v}{\partial x} \right)
\end{aligned} \tag{16}$$

7.2 MACCORMACK'S IMPLICIT-EXPLICIT ALGORITHM

A reasonable mesh is chosen in the computational region such that (i) it provides a good resolution of the flow features, i.e., a fine mesh close to solid boundaries to account for viscous effects with a cell Reynolds number of order 1 or 2 and which stretches out exponentially to merge into a coarse mesh in the outer region where the flow is essentially inviscid, (ii) total number of mesh points is not unreasonably large which would limit how small the mesh length in the direction along the body can be, (iii) mesh fits the body geometry, i.e., mesh can be made up of non-rectangular quadrilaterals. For simplicity, the description of the algorithm is sketched below for a rectangular mesh where x and y are coordinate directions and are along and normal to a solid body respectively.

The algorithm is a time dependent algorithm in which, starting with an assumed initial flow field, solution is advanced in discrete time steps till an asymptotic steady-state solution is reached. In the coarse mesh region, the solution is advanced from one time step to another by a sequence of explicit difference operators represented as

$$U_{i,j}^{n+1} = L_y \left(\frac{\Delta t}{2} \right) L_x(\Delta t) L_y \left(\frac{\Delta t}{2} \right) U_{i,j}^n \tag{17}$$

The difference operator L_y accounts for the effects of the terms $\partial G / \partial y$ and the operator L_x accounts for the terms $\partial F / \partial x$. For example $L_y(\Delta t)$ solves the differential equation

$$\frac{\partial U}{\partial t} + \frac{\partial G}{\partial y} = 0 \tag{18}$$

over a time step Δt by a predictor-corrector algorithm defined by

$$\begin{aligned} \overline{U}_{i,j}^{n+\frac{1}{2}} &= U_{i,j}^n - \frac{\Delta t}{\Delta y} \left(G_{i,j}^n - G_{i,j-1}^n \right) \\ U_{i,j}^{n+\frac{1}{2}} &= \frac{1}{2} \left[U_{i,j}^n + \overline{U}_{i,j}^{n+\frac{1}{2}} - \frac{\Delta t}{\Delta y} \left(\overline{G}_{i,j+1}^{n+\frac{1}{2}} - \overline{G}_{i,j}^{n+\frac{1}{2}} \right) \right] \end{aligned} \quad (19)$$

and

$$U_{i,j}^{n+\frac{1}{2}} = L_y(\Delta t) U_{i,j}^n \quad (20)$$

The difference operator $L_x(\Delta t)$ is similarly defined to solve $\partial U / \partial t + \partial F / \partial x = 0$ over a time step Δt . The symmetric ordering of the sequence of operations in Equation (17) assures us the second-order accuracy of the scheme. The time step Δt is limited by the numerical stability requirement similar to the CFL criterion. Max Δt is in general proportional to Δx and/or Δy . Thus this algorithm, which is quite rapid in the coarse mesh region, becomes slow in the fine mesh region due to small Δy which results in small Δt close to the wall. To overcome this stability restriction in the fine mesh region, $L_y(\Delta t)$ can be further split into two operators -- one an operator L_{yH} which accounts for the hyperbolic terms (convective terms) in Equations (14) and (15) by the use of the method of characteristics and an explicit predictor-corrector method, and the other an operator L_{yp} which accounts for the parabolic terms (viscous terms) in Equations (14) and (15) by an implicit algorithm similar to the Crank-Nicholsen scheme. Thus in the fine mesh region the solution can be advanced over a time step Δt by a sequence of explicit and implicit operators, given by

$$U_{i,j}^{n+1} = \left[L_{yH} \left(\frac{\Delta t}{2M} \right) L_{yp} \left(\frac{\Delta t}{2M} \right) L_x \left(\frac{\Delta t}{2M} \right) L_{yH} \left(\frac{\Delta t}{2M} \right) \right]^M U_{i,j}^n \quad (21)$$

where $M \approx 2$. After each operator in the solution algorithm, proper boundary conditions are enforced.

MacCormack, Deiwert and their associates have reported (Refs. 41 to 44) excellent results for various two-dimensional, axisymmetric and three-dimensional flow problems at transonic and supersonic Mach numbers and at very high Reynolds numbers. The algorithm sketched above

can be generalized for a general quadrilateral (not necessarily rectangular) mesh and Deiwert used this approach to compute transonic separated flows over lifting airfoils (Ref. 42).

7.3 CAVITY FLOW COMPUTATIONS

We have computed the flow past a long cavity on a wind tunnel wall by solving full Navier-Stokes equations by the explicit algorithm due to MacCormack (slow version). For this purpose we have modified a computer program written by Deiwert, which is developed for computing flows past lifting airfoils using arbitrary quadrilateral grids. For the cavity flow a suitable quadrilateral (non-rectangular) grid is generated using conformal mapping techniques. The method of generating the grid is described in Appendix I. Figure 82 shows the mesh generated for a 40-inch long cavity of 1-1/4" depth with 79x31 cells. It may be noted that the mesh cells in the forward and rearward-facing step regions are mirror reflections of one another. Figure 83 is a sketch of the dimensions of a computational region. Figures show the details of the grid near the forward-facing step. Flow is at transonic Mach numbers and at high Reynolds numbers. Entry boundary condition is uniform flow. Leading edge is located sufficiently far ahead of the cavity region so that a turbulent boundary layer is fully developed before encountering the cavity region. Upper wall boundary condition is imposed as a solid inviscid wall.

Results after 460 time steps are shown in Fig. 84. The pressure distribution agrees with experimental results for the most part of the cavity except in the base region behind the rearward-facing step, and downstream of the forward-facing step where numerical resolution is not adequate. The algebraic turbulence model which is used in the calculation is rather empirical and is based primarily on incompressible turbulent boundary layer models. This model is not quite suitable for recirculating flows. Another source of error may be due to a lack of sufficient numerical resolution of the mesh chosen in the base region. Figure 85 shows the velocity vectors in front of the forward-facing step. It has been demonstrated that it is feasible to compute separated transonic flows with full Navier-Stokes equations but much work needs to be done to improve turbulence models in separated regions.

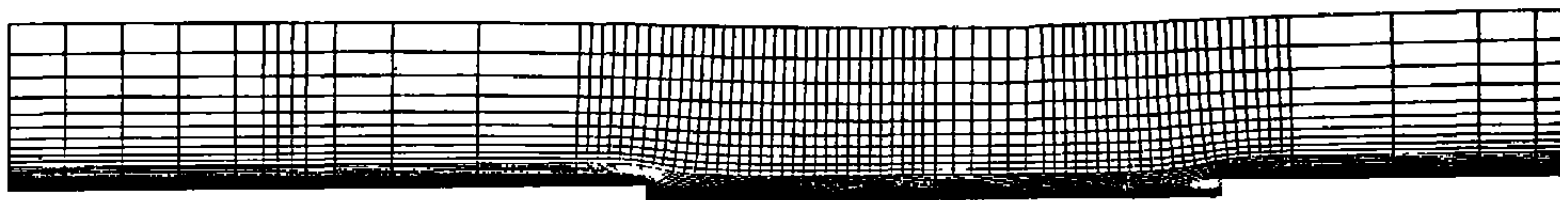


Figure 82. Grid Used for 40-Inch Long Cavity.

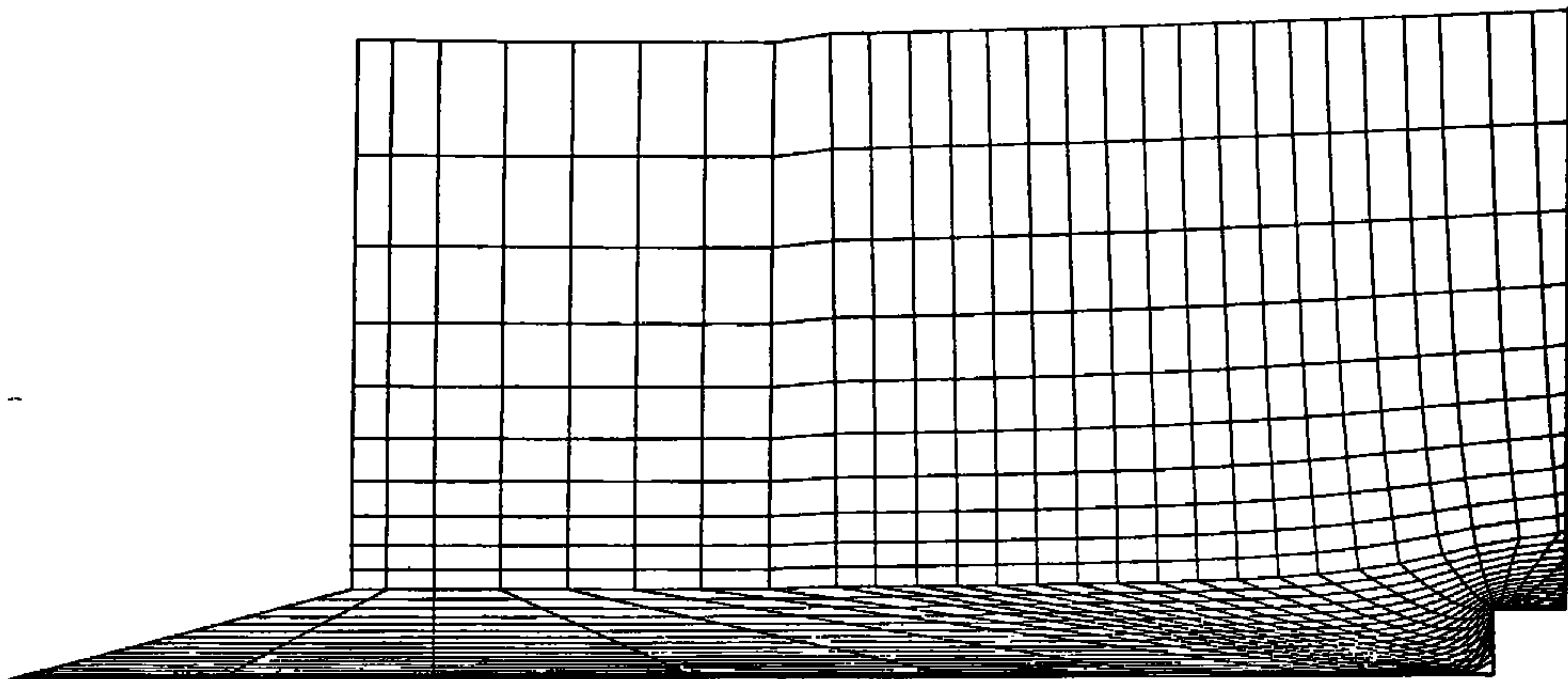


Figure 82. Details of the Grid Near the Forward Facing Step.

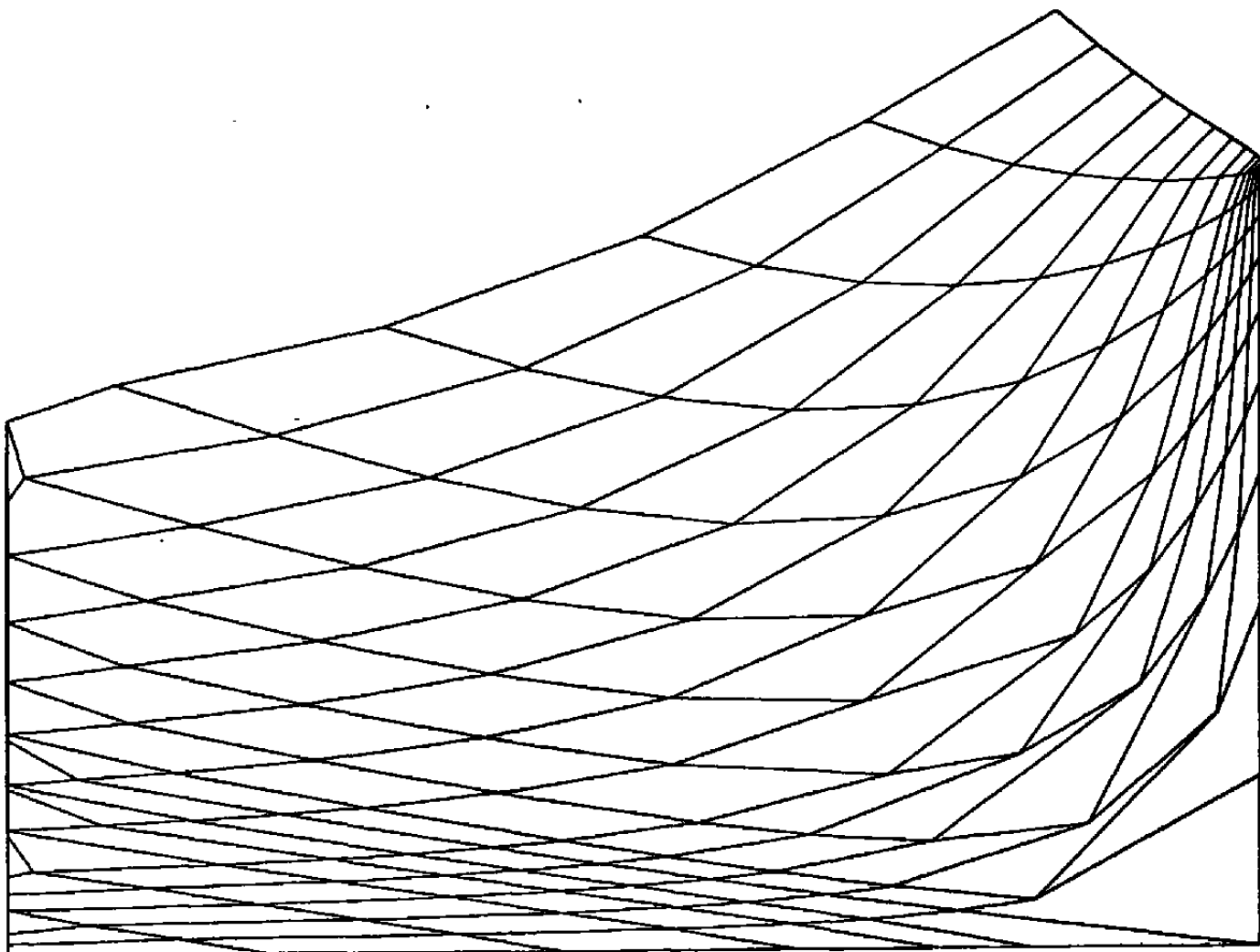
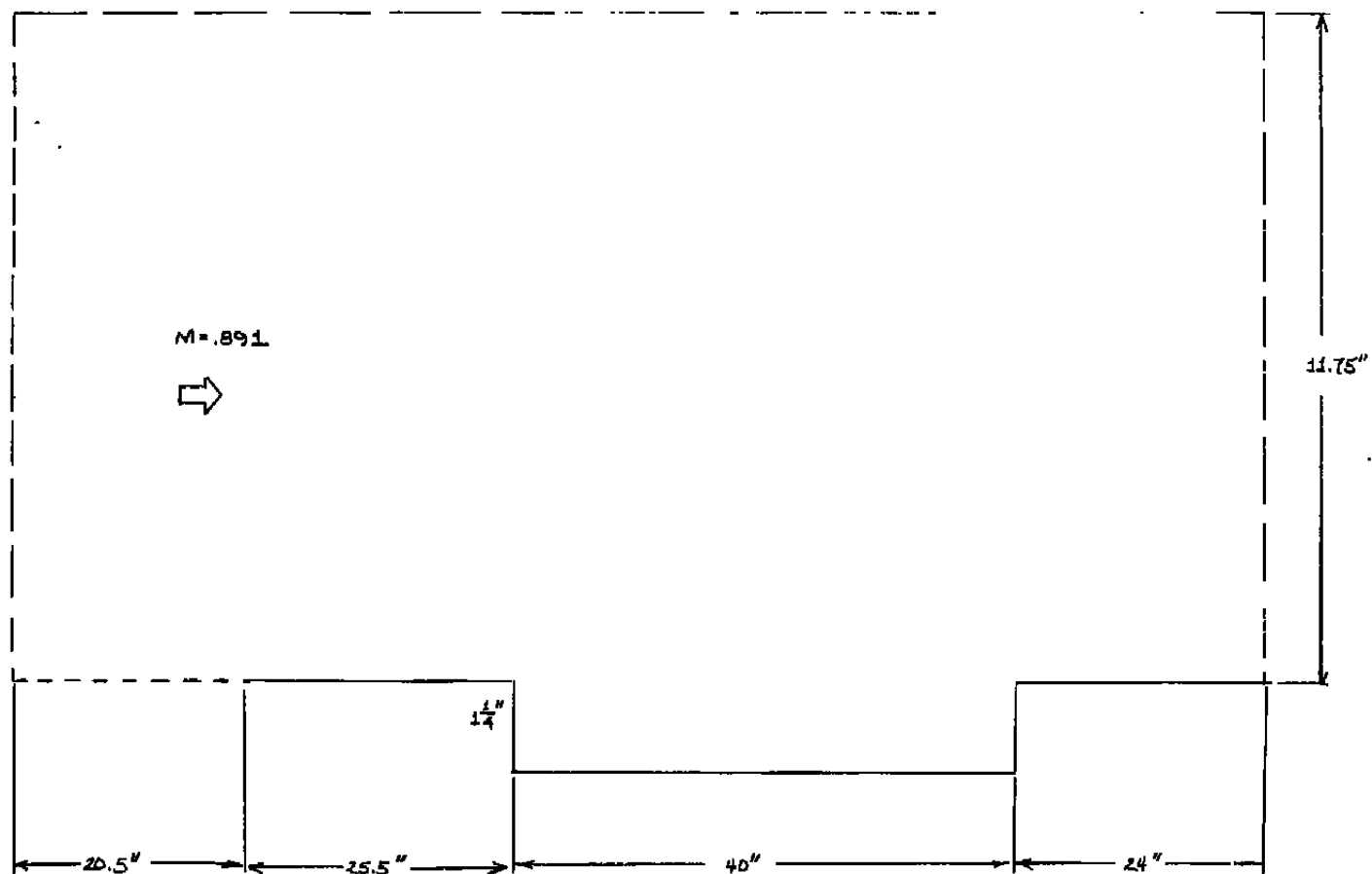


Figure 82. Details of the Grid Near the Forward Facing Step.



$$Re/ft = 8.5 \times 10^6$$

Figure 83. Sketch of the Computational Region for Flow Past a Long Cavity.

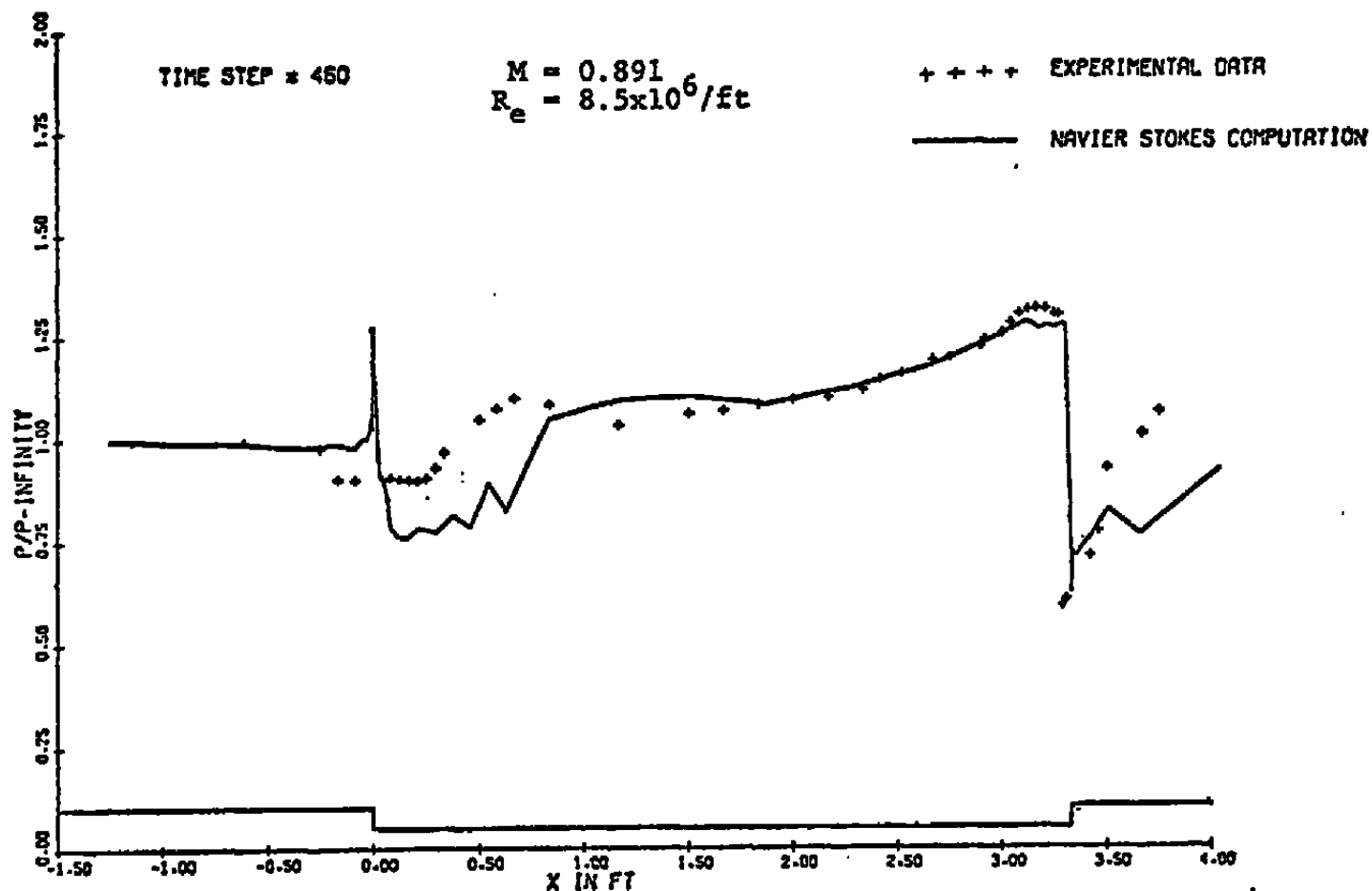


Figure 84. Pressure distribution for flow past a cavity
 (cavity length - 40", cavity height - 1.25").

FORWARD FACING STEP

TIME STEP = 460

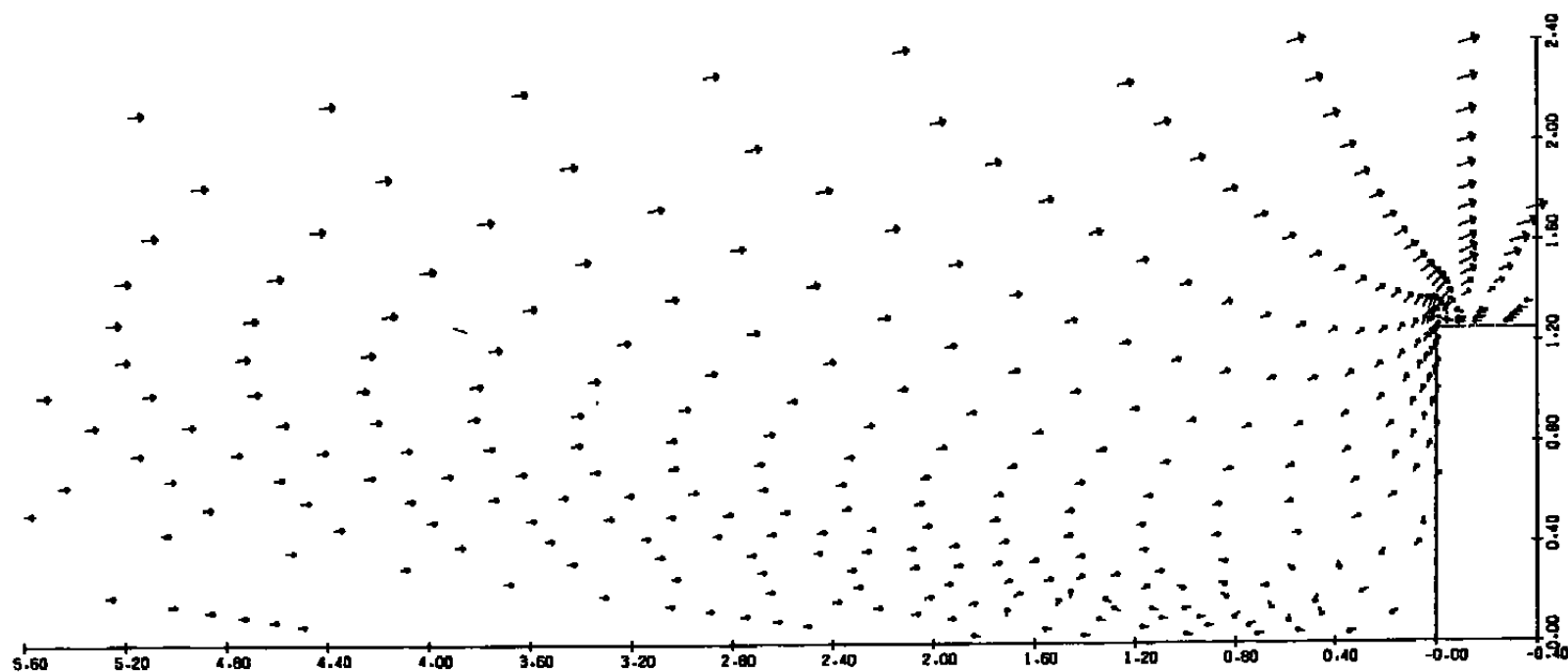


Figure 85. Velocity Vectors Near the Forward Facing Step.

8.0 SUMMARY AND CONCLUSIONS

This investigation was originated to study transonic turbulent flow interactions at high Reynolds numbers. There had not been systematic studies in this specific region of aerodynamics before the initiation of the present work. Therefore, it is hoped that the results of this study will be useful for approaching some of the problems encountered in transonic flow separation. In the first phase of this work (Refs. 1, 2, the wake-separation mechanism was studied for shallow cavity geometries and many conclusions of special interest were drawn. In the present study, the previous work has been generalized and the range of parameters has been extended. In particular the Mach number range was increased to include low supersonic speeds, being from 0.65 to 1.32. The Reynolds number range was 4×10^6 to 200×10^6 .

The experiments were performed in a two-dimensional turbulent boundary layer over the 144-inch-long floor plate of the UTSI transonic wind tunnel. The models for the experiments were produced by modifying the floor of the test section and therefore obtaining large Reynolds numbers comparable to actual flight Reynolds numbers.

Flows with various pressure gradients were produced by the introduction of ramps of different angles, forward-facing steps of different sizes and impinging normal shock waves. The influence of the size and geometry of disturbance generators placed at various distances upstream of the adverse pressure gradient zones were also investigated. For the flow over ramp compression corners with and without the upstream disturbances, the Reynolds number and Mach number effects on such characteristics as the separation distance in front of the ramp, reattachment distance on the ramp and peak pressure on the ramp were studied and correlations obtained. These correlations are shown to be very consistent and, for each category of flow, will provide general, vital information. Through comparison and cross-plotting of the experimental data, it was demonstrated that the effects of a backward-facing step disturbance could be related to the effects produced by cylindrical disturbances. The main concern of the studies without upstream disturbances was to determine the incipient separation angle and the Mach number and Reynolds number dependence of that angle. The incipient separation angle for high subsonic and low supersonic speeds was found to be about 22.5 degrees. In the presence of upstream disturbances this angle was found to increase in some situations. The following

conclusions were drawn for the flow over ramp compression corners:

1. The peak pressure increases with increasing Mach numbers and slightly with increasing ramp angles.
2. The peak pressure location moves up the ramp as the ramp angle increases.
3. Upstream disturbances in the flow produce distortions in the boundary layer, which in turn results in a lower peak pressure over the ramp.
4. Under some conditions the presence of an upstream disturbance results in the transfer of kinetic energy into the disturbed shear layer and a consequent increase in the incipient separation angle.
5. The flow relaxation downstream of a disturbance takes place over a long distance.
6. Pressure recovers faster than the velocity downstream of a disturbance.
7. The size and geometry of a disturbance, normalized with the undisturbed boundary layer thickness, determines the extent of the flow modification introduced.
8. The extent of the disturbance generated by a backward-facing step is small compared to that due to cylindrical disturbances.

Reynolds number and Mach number effects on the characteristic local pressure parameters like base-, plateau-, separation- and peak-pressure were studied in detail for the flow over shallow cavities. Correlations between each of the above parameters and the Mach number, Reynolds number and free stream conditions were obtained. It was observed that an upstream disturbance may, depending upon the disturbance strength and the flow parameters, either suppress or enhance a downstream separation. It was also observed that by proper scaling there exists a similarity in surface pressure distribution of the transonic flow over airfoils in the attached region between the shock wave and trailing edge separation and the attached flow on a rectangular cavity floor.

Boundary layer velocity profile measurements were made for most of the tests. It was found that the surface pressure recovers faster than the velocity profile downstream of a disturbance. That is, the disturbed pressure field reaches equilibrium in a shorter distance downstream of a disturbance than does the velocity profile. The velocity recovery starts from the wall and spreads outwards; therefore the outer portion of the boundary layer (the wake part) carries the disturbance effect for a longer distance downstream of the interaction region. Velocity profiles were plotted in terms of the Coles Law of the Wall, Law of the Wake parameters and it was observed that a disturbed boundary layer, as well as the boundary layer in regions of large pressure gradients, showed quite extensive deviations from the flat plate flow.

No separation bubble in the region of the interaction of a normal shock and the boundary layer was discovered at Mach numbers up to $M_\infty \sim 1.32$. Static as well as high-speed Schlieren pictures were taken and it was observed that the detached shock was oscillating with a frequency of nearly 250 Hz. This was due to the shock-generating device (shock holder) interfering with the flow field being investigated.

Since the boundary layer is one of the most important flow features in studies such as the present, it would have been very desirable to have more velocity profile measurements for each test: both in the undisturbed and the disturbed regions of the flow. During the analysis of the experimental results, information about the oncoming undisturbed flow would possibly have explained a group of abnormalities observed on different plots.

It has been demonstrated that separated transonic flows, such as flows past rearward and forward-facing steps of a long cavity, can be computed using the full Navier-Stokes equations. However, the accuracy is rather limited in the separated region behind the rearward-facing step due to the inadequacy of algebraic turbulence model and a lack of sufficient numerical resolution.

9.0 LIST OF REFERENCES

1. Wu, J. M., et al. "Fundamental Studies of Subsonic and Transonic Flow Separation, Part I — First Phase Summary Report," AEDC-TR-75-95, September 1975.
2. Wu, J. M., et al. "Fundamental Studies of Subsonic and Transonic Flow Separation, Part II — Second Phase Summary Report," AEDC-TR-77-103, December 1977.
3. Chang, P. K. Separation of Flow, Pergamon Press, 1966.
4. Wu, J. M., and T. H. Moulden. "A Survey of Transonic Aerodynamics," AIAA Paper No. 76-326, AIAA 9th Fluid and Plasma Dynamics Conference, July 14-16, 1976, San Diego, California.
5. Chapman, D. R., D. M. Kuehn and H. K. Larson. "Investigation of Separated Flows in Supersonic and Subsonic Streams with Emphasis on the Effect of Transition," National Advisory Committee for Aeronautics Report 1356, 1958.
6. AGARD Conference Proceedings CP4: "Separated Flows" Parts 1 and 2, 1966.
7. Wauschkuhn, P., and V. Vasanta Ram. "The Turbulent Boundary Layer Behind a Separated Region," Report No. 32/1974, Bochum, 1974. Translation by A. Vakili-Dastjerd, H. J. Ramm, J. M. Wu.
8. Pearcey, H. H., J. Osborne and A. B. Haines. "The Interaction Between Local Effects at the Shock and Rear Separation — A Source of Significant Scale Effects in Wind-Tunnel Tests on Airfoils and Wings," Paper No. 11, Transonic Aerodynamics, AGARD Conference CP-35, September 1968.
9. Shen, L. "On Transonic Wind Tunnel Design Consideration," Master's Thesis, The University of Tennessee, Knoxville, Tennessee, 1974.
10. Vakili-Dastjerd, A. "Study of Direct Skin Friction Measurements and Design of Nozzle for Upper Transonic Wind Tunnel," M.S. Thesis, The University of Tennessee, Knoxville, Tennessee, August 1976.
11. Dowgwillo, R. M. "An Analysis of Data Quality in Transonic Wind Tunnel Testing," M.S. Thesis, The University of Tennessee, Knoxville, Tennessee, December 1977.

12. Charboneau, G. W. "Design of Data Acquisition Systems for the UTSI Transonic Wind Tunnel," M.S. Thesis, The University of Tennessee, Knoxville, Tennessee, 1977.
13. Wu, Jain-Ming, and Robert C. Lock. "A Theory for Subsonic and Transonic Flow Over a Cone -- With and Without Small Yaw Angle," TR-RD-74-2, U. S. Army Missile Command, Redstone Arsenal, Alabama.
14. Ames Research Staff, "Equations, Tables, and Charts for Compressible Flow", NACA 1135, 1953.
15. Kuwano, Hideki. "Study on High Subsonic Turbulent Flow Incipient Separation and Hole/Boundary Layer Interaction," M.S. Thesis, The University of Tennessee, Knoxville, Tennessee, June 1976.
16. Schubauer, B. B., and P. S. Klebanoff. "Investigation of Separation of the Turbulent Boundary Layer," NASA R-1030.
17. Chu, J., and A. D. Young. "Measurements in Separating Two-Dimensional Turbulent Boundary Layers," AGARD CP-168, May 1975.
18. Settles, G. S., S. M. Bogdonoff, and I. E. Vas. "Incipient Separation of a Supersonic Turbulent Boundary Layer at High Reynolds Numbers," AIAA J., Vol. 14, pp. 50-56, 1976.
19. Inger, G. R. "Similitude Properties of High-Speed Laminar and Turbulent Boundary-Layer Incipient Separation," AIAA J., Vol. 15, No. 5, May 1977.
20. Appels, C. "Incipient Separation of a Compressible Turbulent Boundary Layer," Von Karman Institute for Fluid Dynamics, TN 99, Rhode-St.-Genese, Belgium, April 1974.
21. Kuehn, D. M. "Experimental Investigation of the Pressure Rise Required for the Incipient Separation of Turbulent Boundary Layers in Two-Dimensional Supersonic Flow," National Aeronautics and Space Administration Memo 1-21-59A, Washington, D. C., February 1959.
22. Roshko, A., and G. J. Tomke. "Supersonic, Turbulent Boundary Layer Interaction with a Compression Corner at Very High Reynolds Number," Proceedings of the 1969 Symposium on Viscous Interaction Phenomena in Supersonic and Hypersonic Flow, Dayton, Ohio,

23. Sterrett, J. R., and J. C. Emery. "Experimental Separation Studied for Two-Dimensional Wedges and Curved Surfaces at Mach Numbers of 4.8 to 6.2," National Aeronautics and Space Administration TND-1014, Washington, D. C., February 1962.
24. Batham, J. P. "An Experimental Study of Turbulent and Re-Attaching Flows at a High Mach Number," J. Fluid Mech. 52, 425-435, 1972.
25. Elfstrom, G. M. "Turbulent Hypersonic Flow at a Wedge-Compression Corner," J. Fluid Mech. 53, 113-127, 1972.
26. Chen, C. H. "Study of Subsonic and Transonic Flow Separation -- With and Without Upstream Disturbance," Ph.D. Dissertation, The University of Tennessee, Knoxville, Tennessee, 1975.
27. Kuwano, Hideki. "Study on High Subsonic Turbulent Flow Incipient Separation and Hole/Boundary Layer Interaction," M.S. Thesis, The University of Tennessee, Knoxville, Tennessee, June 1976.
28. Tennekes, H., and J. L. Lumley. A First Course in Turbulence, M.I.T. Press.
29. Czarnecki, K. R., and M. W. Jackson. "Turbulent Boundary-Layer Separation Due to a Forward-Facing Step," AIAA Paper No. 74-581.
30. Wilson, R. E., and F. Maurer. "Turbulent Boundary Layer Separation at Low Supersonic Mach Numbers," AIAA Journal, 9: 189-190, January 1971.
31. Lo, C. F., F. L. Heltsley and M. C. Altstatt. "A Study of Laser Velocimeter Measurements in a Viscous Transonic Flow," AIAA Paper No. 76-333, AIAA 9th Fluid and Plasma Dynamics Conference, July 14-16, 1976, San Diego, California.
32. Wu, J. M., et al. "Fundamental Studies of Subsonic and Transonic Flow Separation, Part II -- Second Phase Summary Report," AEDC-TR-77-103, December 1977.
33. Neiland, V. Ia., "Supersonic Flow of a Viscous Fluid Around A Separation Point," 3rd Pan-Soviet Meeting on Theoretical and Applied Mechanics, 25 Jan.-1 Feb., 1968 -- Conference Proceedings, Nanka, Moscow (1968) (in Russian).

34. Neiland, V. Ia., "Asymptotic Problems of the Viscous Supersonic Flows," ZAGI Report No. 1529 (1971) (in Russian).
35. Stewartson, K., and P. G. Williams. "Self-Induced Separation," Proc. Roy. Soc., London, A 312, pp. 181-206 (1969).
36. Stewartson, K. "Multistructured Boundary Layers on Flat Plates and Related Bodies," Advances in Applied Mech., 13, pp. 145-239 (1974).
37. Gadd, G. E. "Interaction Between Normal Shockwaves and Turbulent Boundary Layers," NPL, R. & M. No: 3262, February 1961.
38. Gadd, G. E. "An Experimental Investigation of Interaction Between Shock Waves and Boundary Layers," J. of Aero. Sci., Vol. 20, No. 11, November 1953, pp. 729-739.
39. Alber, I. E., J. W. Bacon, B. S. Masson and D. J. Collins. "An Experimental Investigation of Turbulent Transonic Viscous-Inviscid Interactions," AIAA Jour., Vol. 11, No. 5, May 1973, pp. 620-627.
40. Vidal, R. J., Witliff, P. A. Catlin and B. H. Sheen. "Reynolds Number Effects on the Shock-Wave Turbulent Boundary Layer Interaction at Transonic Speeds," AIAA Paper No. 73-661.
41. MacCormack, R. W. "An Efficient Numerical Method for Solving the Time Dependent Compressible Navier-Stokes Equations at High Reynolds Number," NASA TM X-73, 129, July 1976.
42. Deiwert, G. S. "Computation of Separated Transonic Turbulent Flows," AIAA Journal, Vol. 14, June 1976, pp. 735-740.
43. Viegas, J. R., and T. J. Coakley. "Numerical Investigation of Turbulence Models for Shock Separated Boundary-Layer Flows," AIAA Paper 77-44, January 1977.
44. Hung, C. M., and R. W. MacCormack. "Numerical Solution of Three-Dimensional Shock Wave and Turbulent Boundary Layer Interaction," AIAA Paper 78-161, January 1978.

APPENDIX I

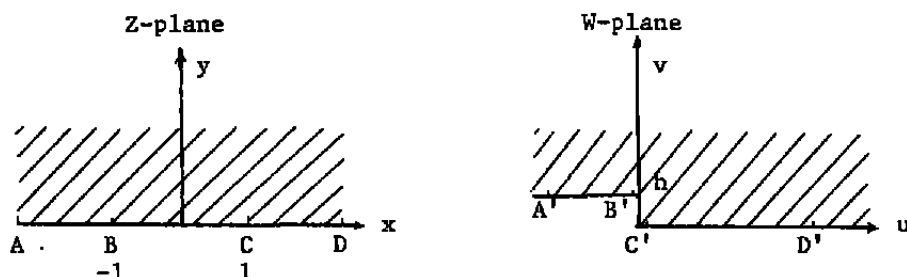
I.1 GRID GENERATION FOR FLOW OVER A LONG CAVITY

The objective is to generate a quadrilateral grid over a region bounded in the bottom by a long shallow cavity with a leading edge ahead of the cavity and bounded on the top by a wind tunnel wall as shown in Fig. 83 with typical dimensions. The grid should be fine enough to provide sufficient resolution in the viscous separated flow near the cavity wall, but be coarse in the region away from the cavity (inviscid flow boundary conditions are assumed at the top wall). Number of cells are of the order 79x31.

A conformal mapping of the form:

$$W = \frac{h}{\pi} \{ (Z+1)^{1/2} (Z-1)^{1/2} + \log[Z + (Z+1)^{1/2} (Z-1)^{1/2}] \}$$

maps points in the Z-plane into the W-plane as shown below.



where $Z = x + iy$, $W = u + iv$, h is the step height. We generate a grid based on this transformation for one half of the cavity and essentially reflect it to obtain the grid for the other half.

If a rectangular mesh in the x - y plane is mapped into the u - v plane the following results (Fig. 86). The line $x = \text{constant}$ and $y = \text{constant}$ map into equipotential and streamlines in the W -plane. This type of mapping while it places mesh lines close to the wall in the viscous region close to the cavity wall with desirable Δv -spacing, makes Δu -spacing in the outer inviscid region too small. Too small Δu in the inviscid region results in too small time steps for the flow field calculation in that region. To avoid this difficulty sloping lines are chosen in the Z -plane in the region corresponding to the sublayer and boundary layer, as shown in Fig. 86.

Since the inverse mapping is not available analytically, we first map x-y plane into the u-v plane for $y = 0$ with sufficiently small Δx . We choose proper spacing for u-points in the W-plane and locate the corresponding points in the x-y plane. In the viscous region Δv_{\min} is chosen to be

$$v_{\min} \approx \frac{2}{3} \frac{c}{\sqrt{Re_c}},$$

where c is the length of the cavity. u-spacing in the sub-layer, boundary layer and the outer inviscid layer are obtained by suitable exponential sketching. With the chosen v-spacing, the corresponding points in the Z-plane are determined. For y -height of the boundary layer, we map points in the Z-plane into W-plane with sufficient resolution. Then the range of grid points in the W-plane which correspond to the slanted lines in the Y-plane is decided upon. Taking equal divisions of this distance corresponding points are located in Z-plane. After this the points in Z-plane which map into the desirable grid in W-plane are all determined.

After generating the grid for one half of the cavity the other half-grid is obtained by reflecting this. Care is also taken to provide some resolution near the leading edge in front of the cavity. Figure 82 shows the complete cavity and the grid details near the forward-facing step.

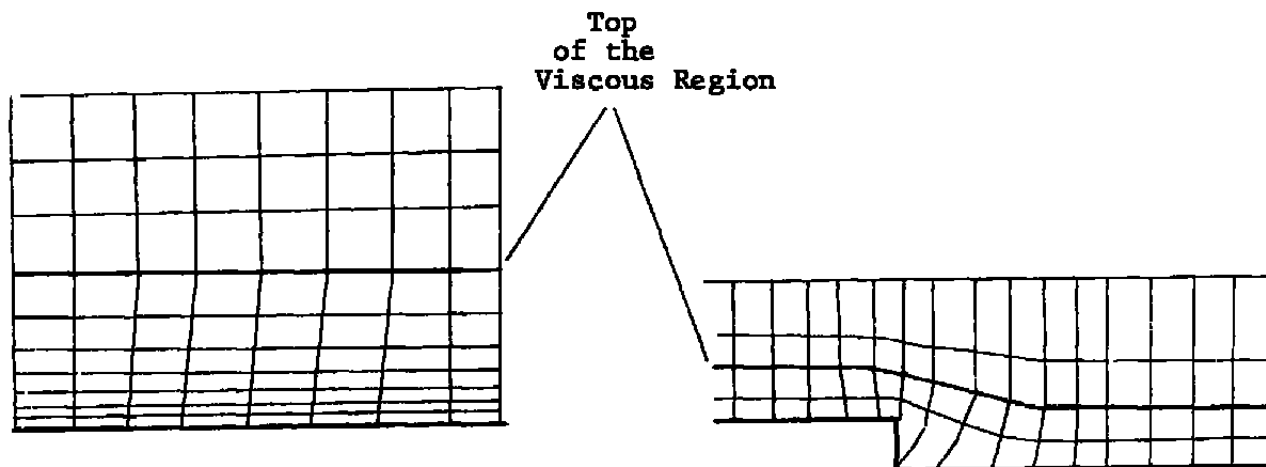


Figure 86. Mapping of the Rectangular Mesh in the x - y Plane into the uv Plane.